UCID-20156

Evaluation of Subsurface Fracture Geometry Using Fluid Pressure Response to Solid Earth Tidal Strain

Jonathan M. Hanson,

Manager of Applied Geophysics

Terra Tek Research

Salt Lake City, Utah 84108

September 1984

DISCLAIMER

DISCLAIMER

Printed in the United States of America
Available from
National Technical Information Service
U.S. Department of Commerce
5285 Port Royal Road
Springfield, VA 22161
Price: Printed Copy $; Microfiche $4.50

Page Range	Domestic Price	Page Range	Domestic Price
001-025	$ 7.00	326-350	$ 26.50
026-050	8.50	351-375	28.00
051-075	10.00	376-400	29.50
076-100	11.50	401-426	31.00
101-125	13.00	427-450	32.50
126-150	14.50	451-475	34.00
151-175	16.00	476-500	35.50
176-200	17.50	501-525	37.00
201-225	19.00	526-550	38.50
226-250	20.50	551-575	40.00
251-275	22.00	576-600	41.50
276-300	23.50	601-up[1]	
301-325	25.00		

[1]Add 1.50 for each additional 25 page increment, or portion thereof from 601 pages up.

UCID--20156

DE85 003294

ACKNOWLEDGEMENTS

This report is a summary of work initiated by the author while at the Earth Science Division of the University of California, Lawrence Livermore National Laboratory (LLNL) and the subsequent extension of this work while at Terra Tek Research, Salt Lake City. Funding for the work at LLNL was by the Department of Geothermal Energy, U.S. Department of Energy. The author would like to thank Drs. Leland Younker and Paul Kasameyer, LLNL, and Drs. John Schatz and Lawrence Owen, Terra Tek Research, for their many helpful comments during the course of this work. I would also like to thank Anne MacLeod of Terra Tek Research for her patience in typing this manuscript.

TABLE OF CONTENTS

LIST OF FIGURES

List of Figures (continued)

List of Figures (continued)

List of Figures (continued)

LIST OF TABLES

CHAPTER I

INTRODUCTION

The development of high-temperature, liquid-dominated geothermal resources will require the production and ultimate disposal of large volumes of fluids. Subsurface injection of the wastewater is the only environmentally acceptable scheme for disposal of most geothermal waters primarily because of moderate to high concentrations of dissolved salts. Relatively high waste water rejection temperatures and large discharge volumes also require subsurface disposal. The feasibility for long-term, large volume reinjection of spent geothermal fluid in the United States has yet to be established.

One critical area of concern is the movement and effects of the fluids as they enter the subsurface formation. In order to insure that the objectives of an injection program are realized without undue risk of environmental deterioration, a method to predict and monitor the movement of the injected fluid is necessary. Numerous case studies have demonstrated that the major uncertainty associated with attempts to predict the movement of injected fluid is the presence and orientation of fractures. High permeability fracture zones can serve as conduits for injected fluid and can channelize fluid movement in a localized and unpredictable fashion. Development of monitoring approaches which allow major fluid carrying fractures to be mapped and characterized would help to guarantee successful long-term reinjection programs.

Careful measurement and interpretation of pore pressure response to solid earth tides has the possibility of identifying the nature and orientation of the primary fluid conduits away from the injection well. This information would be useful in developing flow models that accurately predict behavior of spent fluids in the injection zone. The appeal of this approach is that no

other remote sensing technique is capable of mapping fracture orientation at depths below a few thousand feet. The target parameters for tidal reservoir testing are the same as conventional testing. However, because the driving forces are directional (tidal strains are tensors), the spatial orientation of the preferred flow conduits will be manifested in the well pressure record.

Preliminary work done by The University of California Lawrence Livermore National Laboratory (LLNL) on data taken at the Raft River Geothermal Area indicates that the nature of connected (i.e., pore or fracture) porosity and fracture orientation can be estimated from the analysis of pore pressure response to solid earth tidal strain.

Subsequent work by Terra Tek Research (Salt Lake City, Utah), has extended the theory to allow for the more complex situation in which drainage to and from the fracture to the formation takes place. Terra Tek Research has successfully field tested this approach in a hydraulically stimulated oil well in an active western Canadian oil field located adjacent to the Eastern Rocky Mountain thrust belt (Hanson, 1982). In addition to work done at LLNL and Terra Tek Research, an effort is currently underway by the Department of Energy, Mines, and Resources, Canada, to investigate the feasibility of characterization of isolated natural fractures in deep crystalline rock masses using the solid earth tidal strain approach (Bower, 1982). This investigation is directed toward the subsurface containment of radioactive wastes.

It is clear from the above that fracture orientation evaluation using fluid pressure response to solid earth tidal strain has applications in a diverse set of field situations. The rapid development of the method over the past few years derives primarily from the development of the extremely high precision quartz pressure gauge and improvements in numerical data analysis methods for extraction of the small pressure signals in background noise. The

results of the work carried out by LLNL at the Raft River Geothermal Reservoir in Idaho and subsequent work by Terra Tek Research in field-testing the method for fracture orientation analysis in a stimulated oil well has been sufficiently encouraging to permit Terra Tek Research to offer this fracture diagnostic method as a commercial service.

The purpose of this report is to describe in detail the current state of this technology. Chapter II discusses the nature of solid earth tidal strain and surface load deformation due to the influence of gravitational forces and barometric pressure loading. Chapter III investigates in detail the pore pressure response to these types of deformation, including the cases of a confined aquifer intersected by a well and a discrete fracture intersected by a well. For the case in which the fracture intersects a permeable formation, the solution for the fracture orientation is under-determined. That is, unless the formation hydraulic parameters are known a priori, there is insufficient information to calculate the fracture orientation based on simply the measurement of fluid pressure to tidal strain. Chapter IV discusses the integration of the tidal response method with conventional pump tests in order to independently calculate the hydraulic parameters of the fracture-formation system. With this information available, the solution for fracture orientation is again over-determined. Chapter V shows how advanced spectral analysis methods, coupled with correlation analysis can be used to extract the tidal response signals from the pressure record. Uncertainties in the signals are estimated using various information-theoretic methods in order to place a confidence level at which we can safely assume that the measured signal is indeed of tidal origin. Chapter VI presents a detailed case study of the method carried out at the Raft River Geothermal Reservoir in Idaho. This study details the background geology and geophysics of the area and summarizes the

current understanding of the geothermal system. All of the analyzed tidal data is presented and the results of the computed fracture orientation using the solid earth tidal strain approach are compared with the extensive field work carried out at Raft River by the Department of Geothermal Energy (U.S. DOE) over the past decade. Chapter VII discusses the direction that future work in the continuing development of this technology should take, including: 1) the present need for an expanded data base for the confirmation of present tidal strain response models, and 2) improvement in response models.

CHAPTER II

NATURE OF SOLID EARTH TIDAL STRAIN AND SURFACE LOAD DEFORMATION

Solid earth tidal strain is a global phenomenon. Every point on the surface and within the earth is subject to two forces: the force of gravity due to Newtonian attraction of the mass of the Earth, Moon, and Sun, and the centrifugal force due to the rotation of the earth. Because the relative location of the Moon and Sun with respect to a fixed point within the earth varies with time, the forces at that point will also vary with time and with the orbital paths of these bodies. The tidal gravitational potential, and consequently the tidal force, can be evaluated if the various orbital parameters are known. Taking advantage of the work performed by astronomers of the last century, it has been possible to determine with extraordinary precision these orbital parameters. A description of the method by which these parameters are translated into an expression for the tidal gravitational potential is beyond the scope of this report. However, a detailed description of this development is given by Melchior (1966, 1978), Longman (1959), and Harrison (1971). The tidal spectrum is not a simple distribution. Because of the several gravitational periodicites involved, corresponding to rotational and revolutional periodicities, the major tidal energy bands (i.e. diurnal, semi-diurnal, etc.) are broken down into a complex, but well understood, "fine structure". Figure 2.1 shows the main spectral lines of the tidal potential. Melchior (1966) points out that, although the total number of lines in the tidal spectrum is quite large, only five of the lines have real importance geophysically. These five are the two diurnal tides (O_1, K_1) and the three semi-diurnal tides (N_2, M_2, and S_2).

If the Earth was an ideally rigid body, then these applied gravitational forces would induce no deformation. However, the Earth is not rigid, but

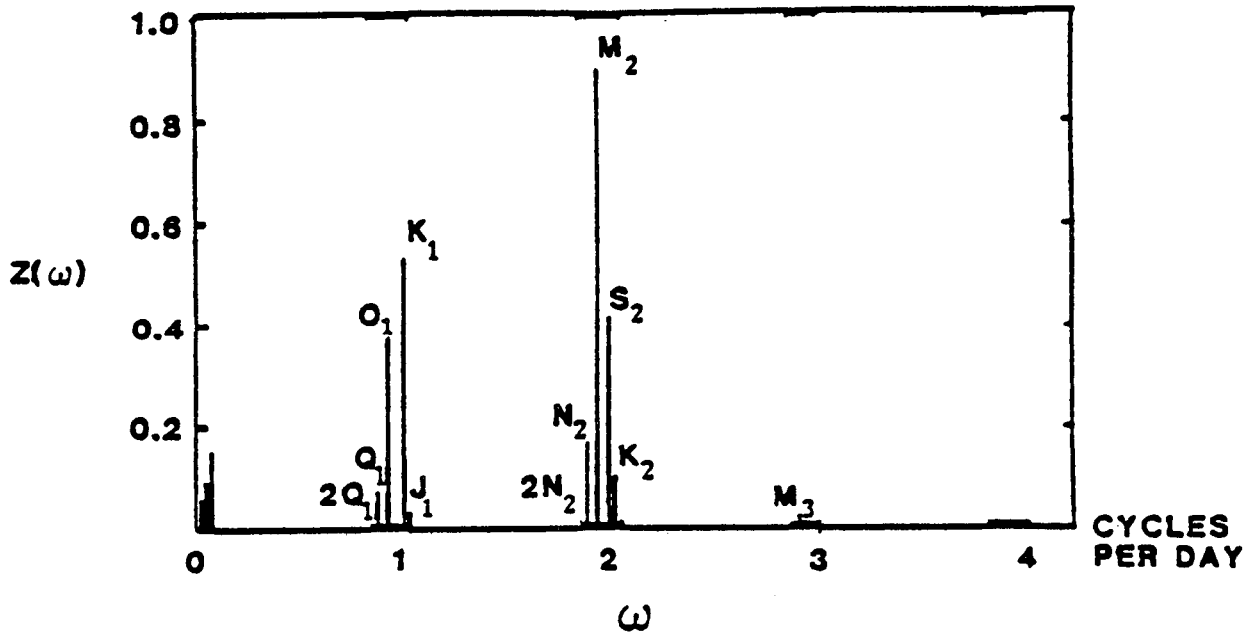

Figure 2.1. The main lines of the spectrum of the tidal potential (from Godin, 1972).

behaves as an elastic-viscoplastic body with complex rheological behavior. For our present purpose, the Earth can be considered to behave in a purely linear-elastic (Hookean) manner to good first approximation. Because of the non-rigid nature of the Earth, gravitational forces will cause strain deformation -- both cubic expansion and shear. In order to quantify the magnitude of these deformations, a knowledge of the distribution of density ρ and elastic Lamé parameters λ and μ from the center of the Earth to the surface is required. This information can be estimated from tabulated seismic velocity data for P and S waves. Sources of this data are given by the Jeffreys-Bullen and Gutenberg-Bullen models (Bullen, 1975). Takeuchi (1950) was the first to integrate this data to obtain the theoretical deformation characteristics of the Earth under applied gravitational forces. His calculations assumed a Hookean Earth. The results can be easily expressed in terms of three parameters: the Love numbers h and k and the Shida number ℓ. These three parameters allow a very practical representation of all deformation phenomena produced by a gravitational potential. The various theoretical tidal strain tensor components are simply linear combinations of the tidal gravitational potential and its spatial derivatives. The coefficients of the linear combinations are the Love and Shida numbers. Further details can be found in Melchior (1966, 1978). The desired result obtained by combining the elastic parameters of the Earth (i.e. the Love and Shida numbers) and the tidal gravitational potential is the tidal strain tensor $\varepsilon(t)$ which is a function of time. $\varepsilon(t)$ is represented as:

$$\varepsilon(t) = \begin{bmatrix} e_{rr}(t) & o & o \\ o & e_{\lambda\lambda}(t) & \tfrac{1}{2}e_{\lambda\theta}(t) \\ o & \tfrac{1}{2}e_{\lambda\theta}(t) & e_{\theta\theta}(t) \end{bmatrix} \qquad \text{(II.1)}$$

where e_{rr}, $e_{\lambda\lambda}$, and $e_{\theta\theta}$ are tidal strains in the radial, E-W, and N-S directions, respectively. $e_{\lambda\theta}$ is the shear strain in a plane tangent to the earth's surface. It should also be pointed out that the strain tensor components depend on location (latitude and longitude) at the Earth's surface.

The depth range of interest, namely a few to tens of kilometers, is much less than the wavelengths of the tidal strain. Therefore, to very good approximation, measurements to these depths can be considered measurements at a free surface (Melchoir, 1978). Therefore, $e_{\lambda r} = e_{r\theta} = 0$, as reflected in the form of the tidal strain tensor. The cubic dilatation Δ, which will be useful in the discussion of pore pressure response in isotropic homogeneous porous rock, is given by the trace of the strain tensor, namely:

$$\Delta(t) = e_{rr}(t) + e_{\lambda\lambda}(t) + e_{\theta\theta}(t) \qquad \text{(II.2)}$$

Since the tidal strain can be represented as a finite sum of constituents, each of which exists at a specific frequency, it is appropriate to recast the strain tensor into its Fourier components. Each tidal constituent (e.g. O_1, K_1, N_2, M_2, or S_2) is represented by a strain tensor cast in the frequency domain,

$$\hat{\varepsilon}(\hat{\omega}_k) = \begin{bmatrix} \hat{e}_{rr}(\omega_k) & o & o \\ o & \hat{e}_{\lambda\lambda}(\omega_k) & \tfrac{1}{2}\hat{e}_{\lambda\theta}(\omega_k) \\ o & \tfrac{1}{2}\hat{e}_{\lambda\theta}(\omega_k) & \hat{e}_{\theta\theta}(\omega_k) \end{bmatrix} \qquad \text{(II.3)}$$

$$k = 1, 2, \ldots, N$$

where the index k corresponds to a particular frequency (i.e. tidal constituent).

The following numerical exercise is presented in order to get a feeling for the magnitude of the volumetric tidal strain at the Earth's surface. As

Melchior (1978) points out, Δ can be cast as a function of the Love and Shida numbers h and ℓ and Poisson's ratio ν as:

$$\Delta = \frac{1-2\nu}{1-\nu} (2h - 6\ell) \frac{W_2}{ag} \qquad \text{(II.4)}$$

where a is the radius of the Earth, W_2 is the tidal potential, and g is the acceleration of gravity (not tidal) due to the Earth's mass. Taking Takeuchi's values of h, and ℓ, and noting that the tidal gravity perturbation Δg is given by (Melchior, 1978):

$$\Delta g = - \frac{2W_2}{a}$$

then

$$\Delta = \frac{1-2\nu}{1-\nu} (2h - 6\ell) \frac{\Delta g}{2g} \qquad \text{(II.5)}$$

$$= 0.49 \frac{\Delta g}{2g}$$

where Poisson's ratio has been taken to be $\nu = 0.25$ and h, ℓ are 0.606 and 0.082, respectively. Figure 2.2 shows the variation of Δg for the major tidal constituents as a function of latitude. It is noted that

$$1 \text{ μgal} = 1\text{x}10^{-6} \text{ cm/sec}^2$$

$$g = 980 \text{ cm/sec}^2$$

Therefore, using the above expression for tidal cubic expansion, the M_2-tide has a maximum volumetric strain of:

$$\Delta_{M_2} \cong \frac{(0.49)(80\text{x}10^{-6})}{(2)(980)}$$

$$= 2\text{x}10^{-8}$$

It is clear from the above exercise that tidal strains are exceedingly small.

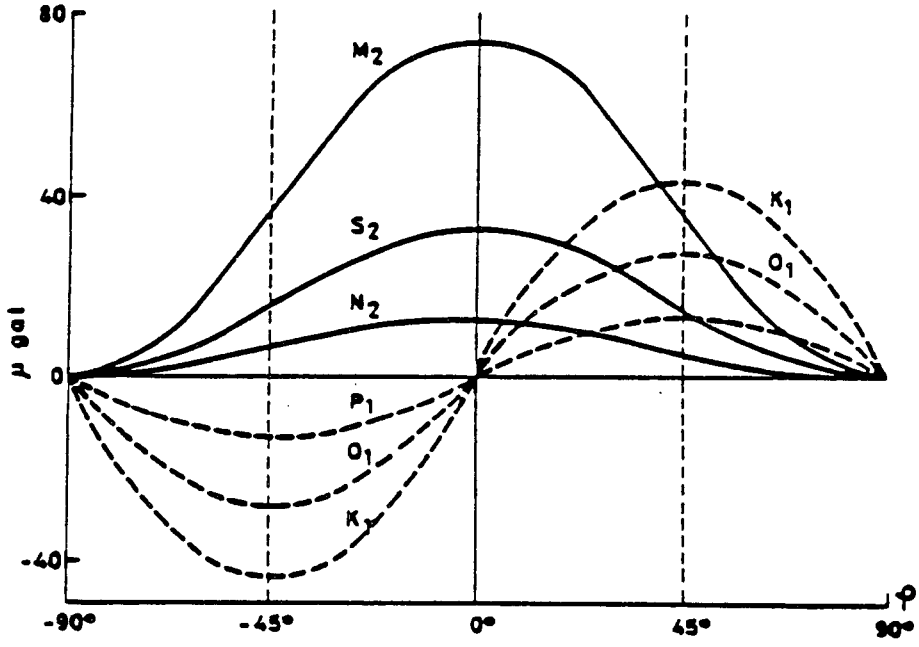

Figure 2.2. Amplitude variation of the principal tidal constituents as a function of latitude for the vertical component of gravity (from Melchior, 1978).

Because strain is a tensor quantity, tidal deformation will depend upon spatial direction. The best way to see this is to evaluate the strain quadric. This is accomplished by evaluating the strain amplitude δ_n along a given direction in space defined by the unit vector $\hat{n}$, where

$$\hat{n} = (\text{Cos}\alpha_1, \text{Cos}\alpha_2, \text{Cos}\alpha_3)^T$$

and $\text{Cos}\alpha_1$, $\text{Cos}\alpha_2$, $\text{Cos}\alpha_3$ are the direction cosines between n and the (vertical, N, E) coordinates, respectively. Thus,

$$\delta_n = \hat{n} \quad \varepsilon \quad \hat{n} \tag{II.6}$$

or, upon multiplication:

$$\delta_n = \text{Cos}^2\alpha_1 \, e_{rr} + \text{Cos}^2\alpha_2 \, e_{\theta\theta} + \text{Cos}^2\alpha_3 \, e_{\lambda\lambda} + \text{Cos}\alpha_2 \, \text{Cos}\alpha_3 \, e_{\theta\lambda}$$

Figure 2.3 shows horizontal and vertical slices through the quadratic surface for the O_1 and M_2 strain tensors evaluated at a latitude of 45°. The quadric surfaces have been normalized so that $W_2/(ag) = 1$. It is clear that from this figure that the O_1 tide has a distinctly different deformation distribution than the M_2 tide. The maximum deformation for the M_2 tide is in the N-S direction whereas the maximum for the O_1 tide is in the E-W direction. As will be seen in a later chapter, this will play a major role in determining the spatial orientation of a fluid-filled fracture.

Deviations of the measured tidal strain from the theoretical strain determined from radially stratified earth models mentioned above come about through a variety of reasons. The most important of those are: 1) the effect of loading due to ocean tides, 2) local geologic inhomogeneities and/or discontinuities in the elastic parameters near the region of strain measurement, and 3) topographic effects. The observed deviations, and various attempts to model them, have been documented by many authors, including Beaumont and

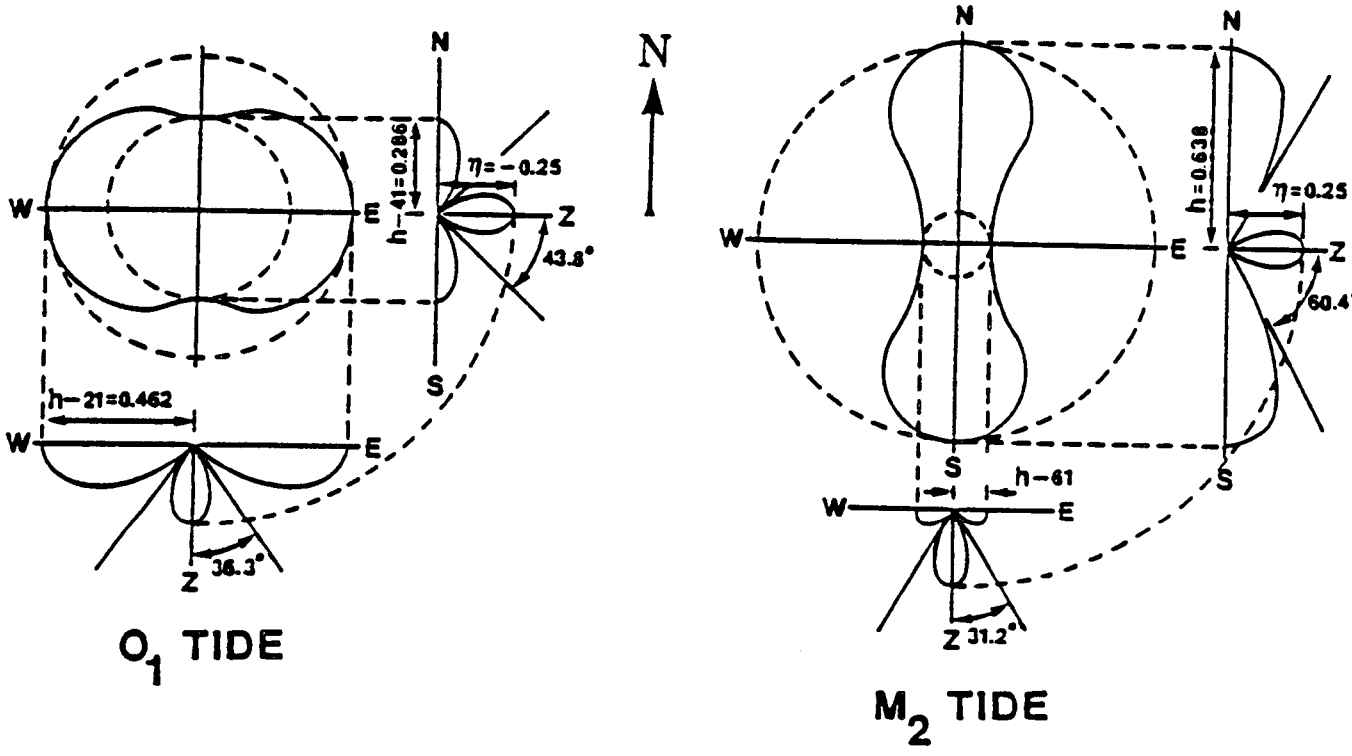

Figure 2.3. Distribution of tidal deformation amplitudes as a function of azimuth and dip for the O_1 and M_2 tides (from Melchior, 1978).

Berger (1975), Berger and Beaumont (1976), Alsop and Kuo (1964), Harrison (1976), Prothero and Goodkind (1972), Harrison, et al. (1963), Lambert (1970), Berger and Wyatt (1973), Farrell (1972, 1979), King and Bilham (1973), and Kuo, et al. (1970). The results of these investigations can be summarized as follows.

1. The effect of loading due to ocean tides can be significant -- up to 44 percent of the total tidal strain tide for the M_2 constituent and 13 percent of the total tidal strain for the O_1 constituent (Beaumont and Berger, 1975). These extreme variations are found near coastlines where the loading effect is most significant, and in most cases, diminish to a second-order effect a few hundred kilometers inland. If cotidal and cophase charts are available for the oceans adjacent to the nearest coastline, the loading effect can be approximated and therefore removed from the observed strain tide.

2. Geologic effects are theoretically important near interfaces between rock types that have radically differing elastic properties. As Berger and Beaumont (1976) point out, "it is difficult to make general statements on the effects of lateral variations in the crust's elastic properties due to geology on the local strain field. This results not so much from a lack of mathematical tools to solve the problem as from the uncertainty in the three-dimensional structure. Were these local variations better known, finite element models could readily be constructed to estimate their effects." Topographic and geologic effects at some strain meter sites have been found to be as large as 25 percent of strain calculated from the radially-stratified whole earth model. Typically topographic effects are considerably smaller than geologic effects. In the case

of geologic effects, however, the spatial variations in the elastic parameters will be a necessary input to a model for tidal strain. Berger and Beamont (1976) have carried out such an analysis at several sites using relatively simple representations of local variations in elastic parameters obtained from regional geology and seismic surveys. This kind of information is often times typically available for geothermal and petroleum reservoirs. Berger and Beaumont's modeling results were consistent with the measured tidal strains. If this kind of site-specific information is not available, an estimate of the uncertainty in elastic parameter anisotropy must be made before the effect of geology on the uncertainty in derived fracture orientation can be evaluated. Clearly more work needs to be done regarding the effect of local geology on the evaluation of fracture geometry using solid earth tidal strain.

It is noteworthy that none of the above investigations of anomalous tidal strain have included the effects of loading due to barometric pressure. There is considerable evidence in the literature to indicate that variations in barometric pressure can induce measureable ground deformation (Tanaka, 1968 a, b; Trubytsyn and Makalkin, 1976; Khorosheva, 1958; Urmantsev, 1970, 1975; and Zschau, 1976). Tanaka (1968 a) found that the ground strain response at Oura, Japan due to atmospheric loading was roughly 1×10^{-8}/mb in the N-S direction and 2.5×10^{-8}/mb in the E-W direction for loading periods between 5 minutes and 60 minutes. Chapman and Westfold (1956) report barometric loads at tidal frequencies ranging from 2.8 to 91 μb for the M_2 tide and 208 to 1482 μb for the S_2 tide. We have measured barometric loads at tidal frequencies computed over a two month period at the Imperial Valley in Southern California, of 18.3 μb, 1358.4 μb, 14.5 μb, 82.3 μb, and 829.7 μb corresponding to the O_1, K_1, N_2,

M_2, and S_2 constituents. Thus, barometric pressure induced strain, based on Chapman and Westfold's barometric load amplitudes and Tanaka's response values, may be as high as 3.71×10^{-8} for the S_2 tide and 0.23×10^{-8} for the M_2 tide. Using our barometric loads measured at the Imperial Valley, we obtain barometric pressure induced strains of 4.6×10^{-10}, 3.4×10^{-8}, 3.6×10^{-10}, 2.05×10^{-9}, and 2.07×10^{-8} corresponding to the O_1, K_1, N_2, M_2, and S_2 tides, respectively. It is evident from the above that the effect of barometric loads must be accounted for in addressing the question of deviations in tidal strain from its theoretical value.

For the purposes of this report, we have accounted for the effect of barometric loading on strain by finding the correlation coefficient between barometric pressure and pore fluid pressure. Having obtained the correlation coefficient, the effect of barometric loads can easily be removed from the fluid pressure data. This approach circumvents the intermediate step of estimating barometric pressure-induced strain, since for this report we are not particularly interested in this parameter. The correlation method will be discussed elsewhere in this report (see Chapter V).

CHAPTER III

PORE PRESSURE RESPONSE TO TIDAL STRAIN AND SURFACE LOADS

Many examples of pore pressure response to solid earth tidal strain and barometric pressure loading have been documented in the literature (Robinson, 1939; Richardson, 1956; Robinson and Bell, 1971; Bredehoeft, 1967; Sterling and Smets, 1971; Marine, 1975; George and Romberg, 1951; Arditty and Ramey, 1978; Bower and Heaton, 1978; Witherspoon, et al., 1978; Rhoads, 1976; Kanehiro, 1980; Hanson, 1979; Hanson and Owen, 1982; and Bower, 1982). Models used to interpret the fluid pressure data are typically based on the theoretical response of a homogeneous isotropic fluid-filled porous elastic rock (Arditty, 1978; Bodvarsson, 1970; Moreland, 1978; Bodvarsson and Hanson, 1978; Bredehoeft, 1967; Van der Kamp and Gale, 1983). Most of the models do not include: a) borehole storage and well-completion effects, and/or b) the presence of discrete fluid-carrying fractures. In the following, we present two models for pressure response to solid earth tidal strain. The first model, based on Biot's theory of consolidation, is similar to previously published models for aquifer response to tidal strain. It is presented here primarily for completeness and will be used later for interpretation of data from the Raft River Geothermal Reservoir. The second model addresses the question of fluid pressure response in a single discrete fracture. Both models include the effects of borehole storage and wellhead completion.

A. Homogeneous Isotropic Aquifer Response to Solid Earth Tidal Strain and Barometric Loads

Consider a confined single-phase fluid-filled aquifer of thickness L, permeability k, and porosity ϕ, subject to an applied volumetric tidal strain

$$\Delta = e_{rr} + e_{\theta\theta} + e_{\lambda\lambda} \tag{III.1}$$

where $e_{rr} + e_{\theta\theta} + e_{\lambda\lambda}$ is the trace of the tidal strain tensor. Using Biot's (1941) linearized theory of consolidation, the volumetric strain Δ and change in pore volume fraction θ can be written as:

$$\begin{aligned} \Delta(\sigma,p) &= \frac{\sigma}{K} + \frac{p}{H} \\ \theta(\sigma,p) &= \frac{\sigma}{H} + \frac{p}{R} \end{aligned} \tag{III.2}$$

with the inverse relationship:

$$\begin{aligned} \sigma(\Delta,\theta) &= \left[\frac{\Delta}{R} - \frac{\theta}{H}\right] /D \\ p(\Delta,\theta) &= \left[\frac{\theta}{K} - \frac{\Delta}{H}\right] /D \end{aligned} \tag{III.2'}$$

where $D = (KR)^{-1} - H^{-2}$

and where p is the change in pore pressure, σ is the change in hydrostatic stress, K is the drained wet rock bulk modulus, and H, R are elastic moduli defined by Biot (1941). Assuming that the fluid is only slightly compressible so that the mass of fluid per unit pore volume is a linear function of σ and p, the change of fluid mass per unit volume can be expressed as:

$$m = \rho_f \left[\theta + \frac{\phi p}{K_f}\right] \tag{III.3}$$

where ρ_f, K_f are the density and bulk modulus, respectively, of the fluid. Conservation of fluid mass within an elemental volume of the aquifer requires that:

$$\partial_t m + \nabla\cdot\vec{q} = 0 \tag{III.4}$$

where $\vec{q}$ is the mass flux through the surface of the volume, given by Darcy's law:

$$\vec{q} = - (\rho_f \, k_r/\mu) \, \nabla p \qquad \text{(III.5)}$$

where μ is the viscosity of the fluid and k_r is the formation permeability. Inserting equations (III.5) and (III.2) into equation (III.4) and rearranging terms, we obtain:

$$\frac{k_r}{\mu} \nabla^2 p - \left[\frac{1}{R} + \frac{\phi}{K_f}\right] \partial_t p = \frac{1}{H} \partial_t \sigma \qquad \text{(III.6)}$$

in terms of an applied stress σ, or:

$$\frac{k_r}{\mu} \nabla^2 p - \left[\frac{1}{R} + \frac{\phi}{K_f} - \frac{k}{H^2}\right] \partial_t p = \frac{K}{H} \partial_t \Delta \qquad \text{(III.7)}$$

in terms of an applied strain. Equation (III.7) is the classical Biot storage equation. The ratio K/H can be identified as the effective stress constant α (Nur and Byerlee, 1971) which is the ratio of the volume of fluid squeezed out of the rock to the total volume change of the rock in the drained condition. A cased well fully penetrates the aquifer and is open to flow over the total thickness L. Flow is assumed to be radial from the well axis and in the horizontal plane only. Conservation of mass at the well-aquifer interface requires that:

$$(\partial_t p + \Lambda \partial_r p)\Big|_{r = r_w} = 0 \qquad \text{(III.8)}$$

where r_w is the well radius and Λ is a constant to be defined later. Using the results of Rice and Cleary (1976), one can show that the expression in brackets in equation (III.7), is identified as:

$$\frac{1}{R} + \frac{\phi}{K_f} - \frac{K}{H^2} = \frac{\alpha - \phi}{K} + \frac{\phi}{K_f} \qquad \text{(III.9)}$$

This equality is valid only under the condition that all void space of any elemental volume of rock is continuous and allows free fluid filtration. It

is useful to compare equation (III.9) with the definition (DeWeist, 1966) of specific storage S_s of a homogeneous isotropic aquifer:

$$\frac{S_s}{\rho_f g} = \frac{(1-\phi)}{K} + \frac{\phi}{K_f} \qquad \text{(III.10)}$$

where g is the acceleration of gravity. We see that the expression in brackets in equation (III.7) closely resembles the specific storage coefficient. Indeed, setting $\alpha = 1$ obtains:

$$\frac{1}{R} + \frac{\phi}{k_f} - \frac{K}{H^2} = \frac{S_s}{\rho_f g}$$

We suggest here that a more realistic expression for the specific storage coefficient is given by:

$$\frac{S_s}{\rho_f g} = \frac{(\alpha-\phi)}{K} + \frac{\phi}{K_f} \qquad \text{(III.11)}$$

This is based on taking the limit of equations (III.10) and (III.11) as $\phi \to 0$. Equation (III.10) implies that a rock with zero porosity has a finite storage, which is clearly a non-physical result. On the other hand, equation (III.11) has a limiting specific storage of

$$\frac{S_s}{\rho_f g} \to \frac{\alpha}{K} \qquad \text{(III.12)}$$

as $\phi \to 0$. Noting that (Nur and Byerlee, 1971) $\alpha = 1 - K/K_g$, where K_g is the grain modulus of the rock, as $\phi \to 0$, $K \to K_g$ and hence $\alpha \to 0$. Thus, the specific storage given by equation (III.11) goes to zero as $\phi \to 0$, which is the desired physical result. We will therefore use equation (III.11) as the definition of specific storage coefficient in the remainder of this report. We point out here that for many, if not most, rocks, K is sufficiently less

than Kg sugh that $\alpha > 0.9$, and to good approximation $\alpha \cong 1$ is sufficient for the current work. With the help of equation (III.11), we can rewrite equation (III.7) as:

$$\frac{k_r}{\mu} \nabla^2 p - \frac{S_s}{\rho_f g} \partial_t p = \alpha \partial_t \Delta \qquad \text{(III.7')}$$

Assuming an oscillating volumetric strain field of the form $\Delta = \Delta_0 \exp(i\omega t)$, equation (III.7') along with the boundary condition given by equation (III.8) can be solved in cylindrical coordinates to obtain:

$$p\big|_{r = r_w} = - \frac{\alpha \rho_f g}{S_s} \frac{T}{1+T} \Delta_0 \qquad \text{(III.13)}$$

where T is a function given by:

$$T = - \frac{i\Lambda}{\omega r_w} \frac{\lambda r_w K_1(\lambda r_w)}{K_0(\lambda r_w)} \qquad \text{(III.14)}$$

and where

$$\lambda^2 = \frac{i\omega\mu S_s}{\rho_f g k_r} \qquad \text{(III.15)}$$

The constant Λ, which is determined by the well completion, is easily shown to be:

$$\Lambda = \begin{cases} - \dfrac{2g\rho_f}{\mu r_w} k_r L, & \text{open well with free liquid surface} \\ - \dfrac{2K_f}{\mu r_w L^*} k_r L, & \text{shut-in well with positive wellhead pressure} \end{cases}$$

where L^* is the depth of the well. The function $T/(1+T)$ has been evaluated numerically for its amplitude and phase characteristics. Figure 3.1 shows these results in terms of three-dimensional surfaces for dimensionless pressure amplitude and phase in terms of the dimensionless parameters $\Lambda/(\omega r_w)$ and λr_w. It is noted that λ^{-1} can be interpreted as a hydraulic skin

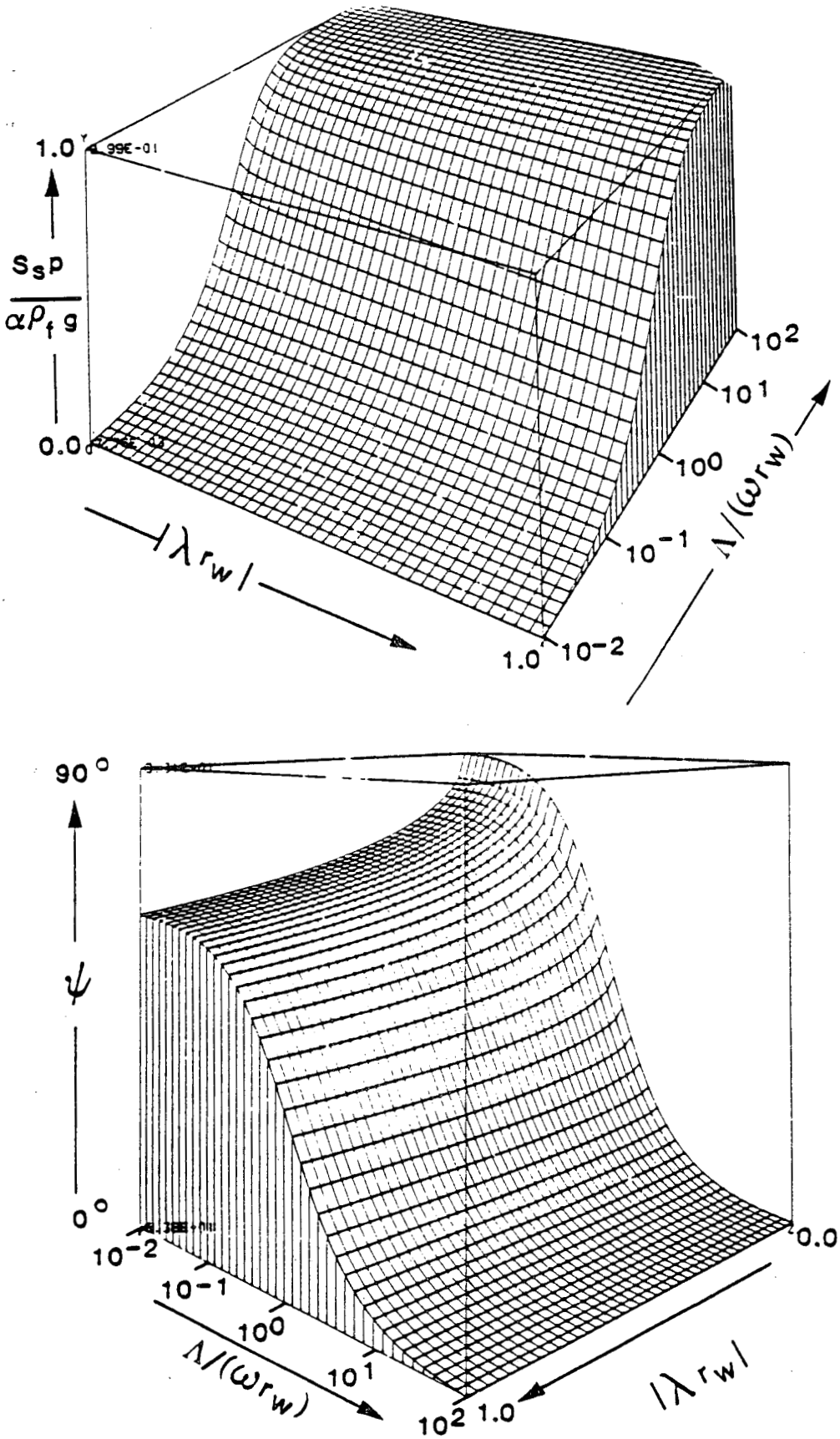

Figure 3.1. Amplitude (top) and phase (bottom) response of a confined homogeneous isotropic aquifer penetrated by a well. The $|\lambda r_w|$ axis is linear whereas the $\Delta/(\omega r_w)$ axis is logarithmic. Parameters are defined in text. Phase lag is relative to the applied volumetric strain.

depth, or in terms of conventional well testing, a "radius of influence." It is clear from Figure 3.1 that, for $\Lambda/(\omega r_w) > 100$, the fluid pressure oscillates in phase with the applied volumetric strain, with pressure amplitude given as:

$$p = \frac{\alpha \rho_f g}{S_s} \Delta_0 \qquad \text{(III.16)}$$

For $\Lambda/(\omega r_w) < 100$, the pressure response falls off with decreasing Λ and also exhibits a phase lag (with respect to Δ_0) that can be as large as 90°. To good approximation, equation (III.16) holds if the permeability-thickness product of the aquifer is:

$$k_r L \geqq \begin{cases} 2.4\text{x}10^4 \text{ md·ft}, & \text{open well} \\ 10.4\text{x}10^{-3} L^* \text{ md·ft}, & \text{closed well, positive well-head pressure } (L^* \text{ in feet}) \end{cases}$$

where we have assumed $r_w = 0.1$ m, $\mu = 1$ cp, $K_f = 2.3\text{x}10^9$ Pa, and $\rho_f = 10^3$ kg/m^3.

The weight of the atmosphere pressing on a confined aquifer will cause a pore deformation and consequently a pore pressure change. The ratio of the pore pressure change to the atmospheric pressure change is referred to as the "barometric efficiency" of the reservoir. Jacob (1940) was the first to show the relationship between the barometric efficiency and the specific storage for a porous aquifer. We can obtain his result from the simple exercise that follows. Consider a reservoir under non-flowing conditions, then from equation (III.6), we can write:

$$\frac{\partial p}{\partial \sigma} = - \frac{\frac{1}{H}}{\frac{1}{R} + \frac{\phi}{K_f}}$$

where p is the change in pore pressure and σ is the change in applied hydrostatic stress. Thus, the product of $\partial p/\partial\sigma$ with specific storage is:

$$S_s \frac{\partial p}{\partial \sigma} = - \rho_f g \left[\frac{\frac{1}{H}}{\frac{1}{R} + \frac{\phi}{K_f}} \left[\frac{1}{R} + \frac{\phi}{K_f} - \frac{K}{H^2} \right] \right]$$

we assume incompressible grains so that $\alpha = 1 - K/K_g = 1$. Also, we make use of the identity (Rice and Cleary, 1976)

$$\frac{1}{R} - \frac{1}{H} = - \frac{\phi}{K_g}$$

where K_g is the grain modulus. Thus, we can write:

$$S_s \frac{\partial p}{\partial \sigma} = - \frac{\rho_f g \phi}{K_f} \left[\frac{\frac{1}{R} + \frac{\phi}{K_g}}{\frac{1}{R} + \frac{\phi}{K_f}} \left[1 - \frac{K_f}{K_g} \right] \right]$$

now $\frac{1}{R} \equiv \frac{1}{H} - \frac{\phi}{K_g} = \frac{1}{K} - \frac{1}{K_g} - \frac{\phi}{K_g}$ where K is the "drained" bulk modulus. Using typical values for loosely bound rocks, we have that

$$K_g > K_f >> K$$

Hence, $\frac{1}{R} \approx \frac{1}{K} >> \frac{\phi}{K_f} > \frac{\phi}{K_g}$ and the term in brackets is approximately units.

Thus,
$$S_s \frac{\partial p}{\partial \sigma} = \frac{-\rho_f g \phi}{K_f} \qquad \text{(III.17)}$$

we see that the product of specific storage with barometric efficiency is directly proportional to the formation porosity ϕ.

B. Discrete Fracture Response to Solid Earth Tidal Strain

In the following discussion, the pressure response of a liquid-filled fracture to solid earth tidal strain will be derived. The simplest model for

this situation is a fluid-filled planar fracture of infinite (or very large) permeability within an impermeable host rock. The definition of "very large" permeability in this case is that the hydraulic skin depth of the fracture is larger than any dimension of the fracture. The orientation of the fracture is defined by the unit vector $\hat{n}$ which is normal to the fracture plane. The unit vector $\hat{n}$ is defined in terms of direction cosines by:

$$\hat{n} = (\text{Cos } \alpha_1, \text{ Cos } \alpha_2, \text{ Cos } \alpha_3) \qquad \text{(III.18)}$$

within the North, East and vertical coordinate system. Maximum volume change of the fracture is caused by applied strain normal to the fracture plane. This strain is given, in terms of the tidal strain tensor, as:

$$\delta(t) = \hat{n}\, \varepsilon(t)\hat{n} \qquad \text{(III.19)}$$

where the explicit time dependence of the strain tensor is shown. The fluid pressure response measured at a well which intersects the fracture will be proportional to the applied normal strain, or:

$$p(t) = K\hat{n}\, \varepsilon(t)\hat{n} \qquad \text{(III.20)}$$

where the proportionality constant K, which is unknown, will depend on fracture size, elastic parameters of the host rock, fluid compressibility, wellbore storage effects, etc. If strain is taken to be positive under compression, K will be a positive constant. For a fracture with hydraulic skin depth less than the fracture dimensions, equation (III.20) becomes a convolution integral in time reflecting the pressure memory of the fracture. The memory is manifested as a time dependence of K, which depends on fracture permeability. Equation (III.20) may be transformed to the frequency domain using Fourier methods to obtain:

$$\tilde{p}(\omega_k) = K\hat{n}\,\tilde{\varepsilon}(\omega_k)\hat{n} \qquad \text{(III.21)}$$

where the finite set of frequencies (ω_k, k = 1,2, ...,N) are those shown in Table 3.1.

The tidal strain tensor near the surface of the earth takes the form:

$$\varepsilon(t) = \begin{bmatrix} e_{rr}(t) & o & o \\ o & e_{\lambda\lambda}(t) & \tfrac{1}{2}e_{\lambda\theta}(t) \\ o & \tfrac{1}{2}e_{\lambda\theta}(t) & e_{\theta\theta}(t) \end{bmatrix} \qquad \text{(III.22)}$$

Therefore, equation (III.21) can be rewritten as:

$$\begin{aligned} \tilde{p}(\omega_k) = &- K\frac{\nu}{1-\nu}\left[|\tilde{e}_{\theta\theta}(\omega_k)|+|e_{\lambda\lambda}(\omega_k)|\right]e^{i\Phi_k} \\ &+ \frac{K}{1-\nu}\left[|\tilde{e}_{\lambda\lambda}(\omega_k)|+\nu|\tilde{e}_{\theta\theta}(\omega_k)|\right]e^{i\Phi_k}\,\mathrm{Cos}^2\alpha_2 \\ &+ \frac{K}{1-\nu}\left[|\tilde{e}_{\theta\theta}(\omega_k)|+\nu|\tilde{e}_{\lambda\lambda}(\omega_k)|\right]e^{i\Phi_k}\,\mathrm{Cos}^2\alpha_3 \\ &\mp iK\,|\tilde{e}_{\lambda\theta}(\omega_k)|e^{i\Phi_k}\,\mathrm{Cos}\,\alpha_2\,\mathrm{Cos}\,\alpha_3,\quad k = 1,2,\ldots,N \end{aligned} \qquad \text{(III.23)}$$

where the following relationships have been used to simplify the expression:

$$e_{rr} = -\frac{\nu}{1-\nu}\,(e_{\theta\theta} + e_{\lambda\lambda})$$

$$\mathrm{Cos}^2\,\alpha_1 + \mathrm{Cos}^2\,\alpha_2 + \mathrm{Cos}^2\,\alpha_3 = 1$$

$$\arg\,[\tilde{e}_{\theta\theta}(\omega_k)] = \arg\,[\tilde{e}_{\lambda\lambda}(\omega_k)] = \Phi_k$$

(see Major, et al., 1964)

$$\text{and } \Phi_k - \arg\,[\tilde{e}_{\lambda\theta}(\omega_k)] = \pm\,\pi/2 \qquad \text{(III.24)}$$

(see Major, et al., 1964)

Table 3.1

Frequencies of Major Tidal Constituents

Name	ω_k (cycles/h)	k
$2Q_1$	0.0357063506	1
Q_1	0.0372185025	3
O_1	0.0387306544	5
K_1	0.0417807462	12
J_1	0.0432928982	16
$2N_2$	0.0774870968	19
N_2	0.0789992487	21
M_2	0.0805114006	24
S_2	0.0833333333	29
K_2	0.0835614924	31
M_3	0.1207671010	34

The (-/+) in equation (III.23) and the (+/-) in equation (III.24) refer to (diurnal/ semidiurnal) tides. If the measured pressure response at frequency ω_k is now referenced to the tidal potential, and if a value of Poisson's ratio is assumed, then:

$$\tilde{p}(\omega_k)e^{-i\Phi_k} = K\ a_1(\omega_k) + a_2(\omega_k)\ \mathrm{Cos}^2\alpha_2 + a_3(\omega_k)\ \mathrm{Cos}^2\alpha_3 + ia_4(\omega_k)\ \mathrm{Cos}\alpha_2\mathrm{Cos}\alpha_3\ ,\ k = 1,2,\ldots,N \qquad \text{(III.25)}$$

where the coefficients $a_j(\omega_k)$ and the phase of the tidal potential Φ_k are known.

The possibility of computing α_1, α_2 and α_3 (and hence fracture dip and strike) based on a single-well measurement of the pressure response at various tidal frequencies is evident in equation (III.25). The solution of the set of coupled equations given by equation (III.25) can be carried out with either of two fundamentally different approaches. One approach is simply to solve the set of N equations as a nonlinear least-squares problem to obtain not only fracture orientation, but also the proportionality constant K. The latter may yield useful information regarding fracture size and/or effective fracture storage given an appropriate elastic model for the fracture. The other approach, the one used in the analysis of the Raft River data (see Chapter VI), is to recognize that although equation (III.25) includes both real and imaginary parts, K is real. Therefore, the phase of the measured pressure signal, when referenced to the tidal potential, will be independent of K. Amplitude of the measured pressure response, however, depends strongly on K. The dependence can be eliminated from the problem by evaluating equation (III.25) for different frequencies ω_k. Since the fracture is assumed to have large permeability, K will be independent of frequency and therefore will cancel when ratios of equation (III.25) are computed for different frequencies.

It is useful to note that equation (III.23) reduces, for a vertical fracture ($\alpha_1 = 90^o$) to:

$$\tilde{p}(\omega_k)e^{-i\Phi_k} = K \left| e_{\theta\theta}(\omega_k)\right| Cos^2\alpha_3 + \left| e_{\lambda\lambda}(\omega_k)\right| Cos^2\alpha_2 \pm i \left| \tilde{e}_{\lambda\theta}(\omega_k)\right| Cos\alpha_2 \; Cos\alpha_3 \;, \; k = 1,2,...N \tag{III.26}$$

and consequently, a vertical fracture with a N-S strike ($\alpha_3 = 90^o$, $\alpha_2 = 0^o$) has the response:

$$\tilde{p}(\omega_k)e^{-i\Phi_k} = K \left| e_{\lambda\lambda}(\omega_k)\right|, \; k = 1,2,...,N \tag{III.27}$$

and with an E-W strike ($\alpha_3 = 0^o$, $\alpha_2 = 90^o$), has the response:

$$\tilde{p}(\omega_k)e^{-i\Phi_k} = K \left| e_{\theta\theta}(\omega_k)\right|, \; k = 1,2,...,N \tag{III.28}$$

Thus, for a vertical fracture with either a N-W strike or an E-W strike, the measured fluid pressure responds in-phase with the tidal potential. Furthermore, based on equation (III.25), a fracture strike in the northwest quadrant ($Cos\alpha_2 Cos\alpha_3 > 0$) and a fracture strike in the northeast quadrant ($Cos\alpha_2 Cos\alpha_3 < 0$) exhibit equal phase shifts with respect to the tidal potential, but of opposite sign for a given tide. Similarly, for the same strike quadrant, the diurnal and semidiurnal tides also exhibit phase shifts with respect to the tidal potential of opposite sign.

The fracture response model given above does not take into account fluid leakage into the formation or the effect of a finite fracture permeability. In the following discussion, we develop a model of a discrete vertical bi-wing or penny-shaped fracture in a permeable formation (see Figure 3.2). These fracture geometries approximate the actual geometries of a stimulated (hydrau-

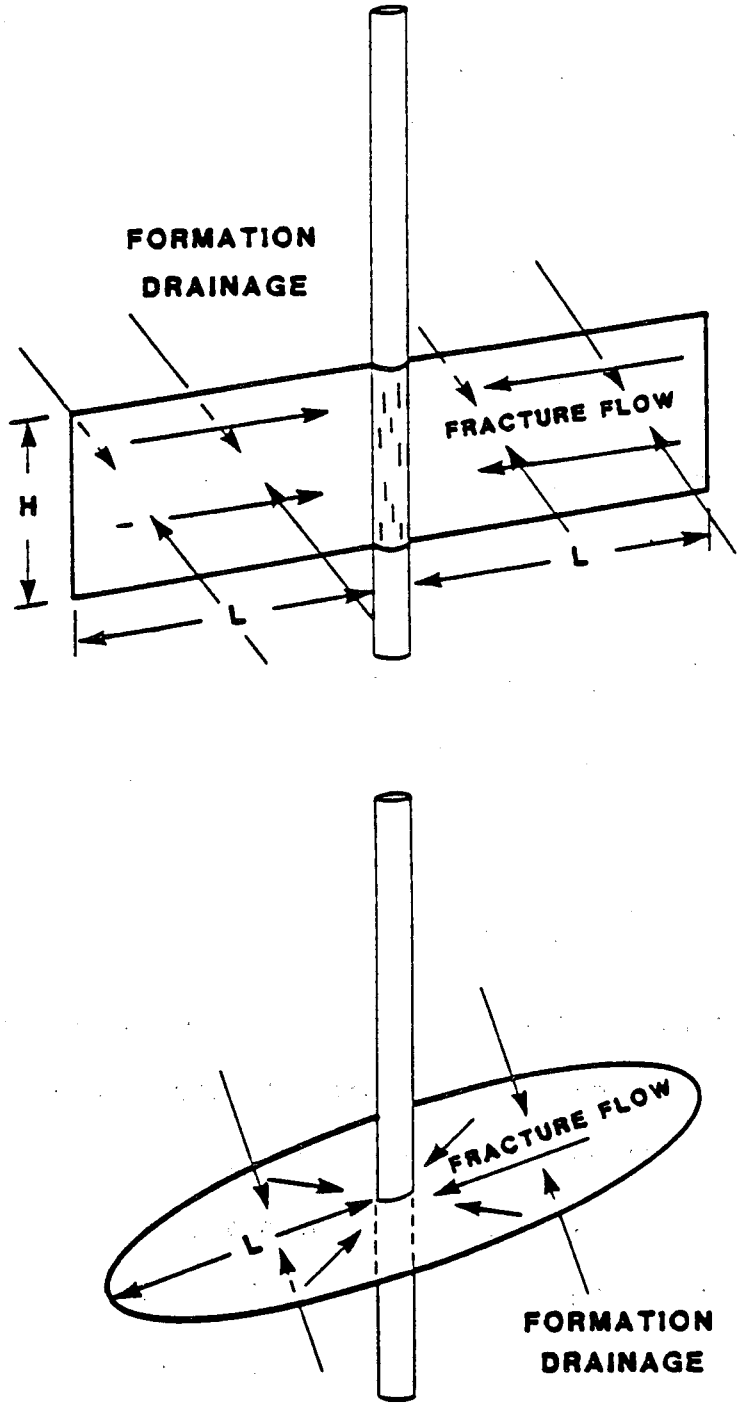

Figure 3.2. Finite vertical bi-wing fracture model and finite penny-shaped fracture model. Formation drainage is normal to the fracture plane.

lically fractured) well. The motivation for choosing these geometries is primarily for comparison with conventional pump test models that are currently being used by the oil and gas industry for characterizing stimulated wells (Cinco-Ley and Samaniego-V, 1981; Rosato, et al., 1982).

We begin by observing an element V of volume bounded by the surface within a fracture. The fracture opening has porosity ϕ and the fluid filling the open spaces of the fracture has density ρ_f. The continuity equation can be written (Duguid and Lee, 1977) as:

$$\frac{d}{dt}\int_V \rho_f \phi \, dV = 0 = \int_V \frac{\partial}{\partial t}(\rho_f \phi) \, dV + \int_S \hat{n} \cdot \rho_f \phi \langle \vec{V}_f \rangle ds \qquad \text{(III.29)}$$

where $\hat{n}$ is the normal to the surface S and $\langle \vec{V}_f \rangle$ is the space-averaged velocity field of the fluid. The fluid velocity can be represented as the sum of the velocity of the solid $\langle \vec{V}_s \rangle$ plus the velocity of the fluid with respect to the solid, $\langle \vec{V}_{fs} \rangle$, or:

$$\langle \vec{V}_f \rangle = \langle \vec{V}_s \rangle + \langle \vec{V}_{fs} \rangle \qquad \text{(III.30)}$$

Now including fluid velocity components along the fracture and normal to the fracture (due to drainage to the formation), we may write, in accordance with Darcy's law:

$$\langle \vec{V}_{fs} \rangle = -\frac{k_f}{\mu} \frac{\partial p}{\partial \ell} \hat{\ell} - \frac{k_r}{\mu} \frac{\partial p}{\partial z} \hat{z} \qquad \text{(III.31)}$$

where $\hat{\ell}$ and $\hat{z}$ are the coordinates along the fracture and normal to the fracture, respectively. k_f and k_r are the permeabilities of the fracture and the formation, respectively. Assuming a slightly compressible fluid so that

$$\rho_f = \rho_o \left(1 + \frac{p}{K_f}\right) \qquad \text{(III.32)}$$

we can combine equations (III.29) through (III.32) to obtain, setting $\phi = 1$ and using the divergence theorem for the surface integral in (III.29),

$$\frac{1}{K_f}\frac{\partial p}{\partial t} + \frac{1}{K_f}\langle\vec{V}_{fs}\rangle \cdot \nabla p + \frac{1}{\rho_o}\nabla \cdot (\rho_f \langle\vec{V}_s\rangle) - \frac{k_f}{\mu}\nabla_2{}^2 p - \frac{k_r}{\mu}\frac{\partial^2 p}{\partial z^2} = 0 \qquad \text{(III.33)}$$

where $\nabla_2{}^2$ is the two-dimensional Laplacian operator in the plane of the fracture. We now make the observation that:

$$\frac{p}{K_f} << 1 \quad \text{and} \quad \langle\vec{V}_{fs}\rangle \cdot \nabla p << \frac{\partial p}{\partial t}$$

Thus, we arrive at the diffusion equation:

$$\nabla_2{}^2 p = \frac{\mu}{k_f K_f}\frac{\partial p}{\partial t} + \frac{\mu}{\rho_o k_f}\nabla\cdot(\rho_f\langle\vec{V}_s\rangle) - \frac{k_r}{k_f}\frac{\partial^2 p}{\partial z^2} \qquad \text{(III.34)}$$

If we assume that the fracture width b_f is constant and is propped open, either by asperities or injected proppant, with material with an incompressibility C (see Snow, 1968), then

$$\langle\vec{V}_s\rangle = -\frac{z}{b_f C}\frac{\partial}{\partial t}(\sigma_n - p)\,\hat{z} \qquad \text{(III.35)}$$

where σ_n is the normal applied stress change on the fracture. In our particular case, σ_n will be the normal component of the tidal stress. Inserting equation (III.35) into equation (III.34), and averaging the fluid pressure across the fracture width, we obtain:

$$\nabla_2{}^2 p - \frac{\mu}{k_f K_f}\frac{\partial p}{\partial t} + \frac{\mu}{k_f b_f C}\frac{\partial(\sigma_n - p)}{\partial t} + \frac{k_r}{k_f b_f}\int_{-b_{f/2}}^{b_{f/2}}\frac{\partial^2 p}{\partial z^2}\,dZ = 0 \qquad \text{(III.36)}$$

where the fluid pressure p, with the exception of the integral term, is taken to be an average value across the fracture. The integral in the last term in equation (III.36) can be written as

$$\int_{-b_{f/2}}^{b_{f/2}} \frac{\partial^2 p}{\partial z^2}\, dz = 2 \left.\frac{\partial p}{\partial z}\right|_{z = b_{f/2}} \qquad \text{(III.37)}$$

where we have assumed a symmetric fluid pressure distribution about the mid-plane of the fracture.

Assuming an oscillating normal stress of the form:

$$\sigma_n(t) = \sigma_n \exp(i\omega t) \qquad \text{(III.38)}$$

It is easy to show that:

$$\left.\frac{\partial p}{\partial z}\right|_{z = b_{f/2}} = -\sqrt{\frac{i\omega}{C_r}}\, p \qquad \text{(III.39)}$$

where C_r is the hydraulic diffusivity of the formation which is given by

$$C_r = \frac{k_r \rho_f g}{\mu S_s} \qquad \text{(III.40)}$$

Combining equations (III.36) through (III.39), we obtain:

$$\nabla_2{}^2 p - \frac{i\omega\mu}{b_f k_f C}\left(1 + \frac{b_f C}{K_f}\right) p - \frac{2k_r}{k_f b_f}\sqrt{\frac{i\omega}{C_r}}\, p = -\frac{i\omega\mu}{k_f b_f C}\,\sigma_n \qquad \text{(III.41)}$$

The above diffusion equation can be simplified considerably by redefining the parameters into a dimensionless form:

$$\sigma_{fD} = \frac{k_f b_f}{k_r L} \qquad \text{(dimensionless fracture conductivity)}$$

$$\eta_{fD} = \frac{k_f}{k_r}\frac{\phi C_t}{(\phi C_t)_f} \quad \text{(dimensionless fracture diffusivity)} \qquad \text{(III.42)}$$

$$d = \frac{\phi C_t \mu L^2}{k_r} \quad \text{(characteristic time)}$$

$$\text{where } \phi C_t = \frac{k_r}{C_r \mu} \quad \text{(porosity - total compressibility product for formation)}$$

$$\text{and } (\phi C_t)_f = \frac{1}{Cb_f} + \frac{1}{K_f} \quad \text{(porosity - total compressibility product for fracture)}$$

We have adopted the porosity-total compressibility notation as opposed to the specific storage notation to be consistent with the common well testing literature. L can be taken to be a characteristic fracture length, which is equal to the half-length of a bi-wing fracture or radius for a penney-shaped fracture.

With these definitions, equation (III.41) can be rewritten as:

$$\nabla_2{}^2 p - \left[\frac{i\omega d}{L^2\eta_{fD}} + \frac{2}{L^2\sigma_{fD}}\cdot\sqrt{i\omega d}\right] p = -i\left[\frac{\omega d}{L^2\eta_{fD}} - \frac{\omega\mu}{k_f K_f}\right]\sigma_n \qquad \text{(III.43)}$$

The expression given by equation (III.43) can be simplified even further by noting that

$$\left[\frac{\mu}{k_f K_f}\right] \div \left[\frac{d}{L^2\eta_{fD}}\right] = \frac{1}{\left[1 + \frac{K_f}{Cb_f}\right]} \qquad \text{(III.44)}$$

Snow (1968) quotes a typical value for asperity incompressibility C of 4.33 x 10^8 Pa/m. Thus, assuming the fluid is water, the ratio $K_f/(Cb_f)$ yields a value of $5.6\text{x}10^2$ for b_f as large as 1 cm. This ratio increases for smaller fracture apertures. Therefore, we can to good approximation set the ratio

$$\left[\frac{\mu}{k_f K_f}\right] \div \left[\frac{d}{L^2\eta_{fD}}\right] \ll 1$$

and equation (15) reduces to:

$$\nabla_2{}^2 p - \left[\frac{i\omega d}{L^2\eta_{fD}} + \frac{2}{L^2\sigma_{fD}}\sqrt{i\omega d}\right] p = -\frac{i\omega d}{L^2\eta_{fD}}\sigma_n \qquad \text{(III.43')}$$

The two dimensional Laplacian takes the form

$$\nabla_2{}^2 = \frac{\partial^2}{\partial r^2} + \frac{1}{r}\frac{\partial}{\partial r}$$

for a penny-shaped fracture in which flow is purely radial, and

$$\nabla_2{}^2 = \frac{\partial^2}{\partial x^2}$$

for linear flow. The conservation of mass boundary condition at the well-fracture interface takes the form:

$$\partial_t p\Big|_{r=r_w} = -\Lambda\, \partial_\ell p\Big|_{r=r_w} \qquad \text{(III.45)}$$

Furthermore, we require a no-flow boundary condition at the crack tip, or:

$$\frac{\partial p}{\partial \ell}\Big|_{\ell = L} = 0 \qquad \text{(III.46)}$$

For the case of a vertical bi-wing fracture with height = H,

$$\Lambda = \begin{cases} -\dfrac{2g\rho_f b_f}{\pi r_w{}^2 \mu} Hk_f & \text{, open-well with free liquid surface} \\ -\dfrac{2b_f K_f}{\pi r_w{}^2 \mu H^x} Hk_f & \text{, shut-in well with positive wellhead pressure} \end{cases}$$

For the case of a penny-shaped fracture,

$$\Lambda = \begin{cases} -\dfrac{2gb_f\rho_f}{\mu r_w}\, k_f\,, & \text{open-well with free liquid surface} \\ -\dfrac{2b_f K_f}{\mu r_w H^*}\, k_f\,, & \text{shut-in well with positive wellhead pressure} \end{cases}$$

The solution of equation (III.43') subject to the boundary condition given by equations (III.45) and (III.46) is:

$$p_{r=r_w} = \frac{T}{1+T}\,\frac{a_2}{a_1}\,\sigma_n$$

where $a_1 = a_2 + a_3$

$$a_2 = \frac{i\omega d}{\eta_{fD}}\,,\quad a_3 = \frac{2}{\sigma_{fD}}\sqrt{i\omega d} \qquad \text{(III.47)}$$

and $$T = -\frac{i\Lambda\sqrt{a_1}}{\omega L}\tanh\left[\sqrt{a_1}\left(1-\frac{r_w}{L}\right)\right] \quad \text{(bi-wing fracture)}$$

or $$T = -\frac{i\Lambda\sqrt{a_1}}{\omega L}\,\frac{K_1(\sqrt{a_1})I_1(\sqrt{a_1}\,\frac{r_w}{L}) - K_1(\sqrt{a_1}\,\frac{r_w}{L})I_1(\sqrt{a_1})}{I_1(\sqrt{a_1})K_0(\sqrt{a_1}\,\frac{r_w}{L}) + I_0(\sqrt{a_1}\,\frac{r_w}{L})K_1(\sqrt{a_1})}$$

(penny-shaped fracture)

It is important to point out that equation (III.47) has been derived under the assumption that the pore structure in the formation is not deforming under the influence of tidal stress. That is, far from the fracture, the pore pressure is constant. This is clearly not the case, as we showed in the earlier discussion of pore pressure response in an isotropic homogeneous aquifer. Therefore, both the deformation of the fracture (i.e. deformation of asperities or proppant) as well as the deformation of the pore structure of the formation will influence the measured pore pressure response to tidal stress. It is easy to show that, under the condition that the formation pore structure is allowed to deform, equation (III.47) becomes:

$$p\Big|_{r=r_w} = \frac{T}{1+T}\left[\frac{a_2}{a_1}\,\sigma_n + \frac{a_3}{a_1}\,p_\infty\right] \qquad \text{(III.47')}$$

where p_∞ is the pore pressure response to tidal strain far from the fracture, given by equation (III.16),

$$p_\infty = \frac{\alpha\rho_f g}{S_s}\,\Delta_o$$

From equation (III.47'), we see that:

for $a_2 = 0$

corresponding to $\dfrac{\omega\mu L^2(\phi C_t)_f}{k_f} = 0$

that $$p\Big|_{r=r_w} = \frac{T}{1+T}\,p_\infty \qquad \text{(III.48)}$$

and

for $a_3 = 0$

corresponding to $\dfrac{(\omega\mu\phi C_t k_r)^{1/2} L^2}{k_f b_f} = 0$

That $$p\Big|_{r=r_w} = \frac{T}{1+T}\,\sigma_n \qquad \text{(III.49)}$$

In the first case ($a_2 = 0$), the fracture has no storage and the pressure perturbation at the well is driven totally by formation pore deformation. In the second case ($a_3 = 0$), the formation has either no storage or no permeability so that the pressure perturbation at the well is driven totally by fracture deformation. Clearly, a realistic case will fall somewhere between these two extreme cases, determined by the ratio

$$R = \frac{a_3}{a_2} = \frac{2\eta_{fD}}{\sigma_{fD}}\,(\omega d)^{-1/2} = \frac{2}{\mu(\phi C_t)_f b_f}\left[\frac{\phi C_t \mu k_r}{\omega}\right]^{1/2} \qquad \text{(III.50)}$$

If R<<1, the pore pressure response will be due primarily to fracture deformation. If R>>1, the pore pressure response will be due primarily to drainage effects caused by pore structure deformation in the formation. In order to get a feeling for the dependence of R on the host rock permeability, we have evaluated equation (III.50) under the assumption that the pore fluid is water, $\phi C_t = 1.5 \times 10^{-10}$ Pa and that the asperity incompressibility is 4.33×10^8 pa/m. With these assumptions,

$$R \approx 0.9 \sqrt{k_r(md)}$$

Hence, we see that if the formation permeability is on the order of 1 md, the pore pressure response to tidal stress is divided roughly equally between fracture deformation and formation pore structure deformation. With the exception of the case in which the formation has a permeability in the microdarcy range (e.g. crystalline granite), it is clear from the above exercise that equation (III.47') must be used as the appropriate general tidal response model.

Hooke's law for isotropic elastic bodies, written in tensor form, is:

$$\sigma_{ik} = \lambda \Delta \delta_{ik} + 2\mu e_{ik}$$

where λ and μ are Lame's parameters, defined in terms of Young's modulus E and Poisson's ratio ν, as

$$\lambda = \frac{E}{(1+\nu)(1-2\nu)}$$

$$\mu = \frac{E}{2(1+\nu)}$$

Thus, the normal stress σ_n in equation (III.47') can be written as:

$$\sigma_n = \lambda \Delta + 2\mu \, \hat{n} \varepsilon \hat{n}$$

where $\hat{n}\varepsilon\hat{n}$ is the normal component of the strain tensor. Therefore, equation (III.47') can be rewritten as:

$$p\Big|_{r=r_w} = \frac{T}{1+T}\left[\frac{a_2}{a_1}(2\mu\hat{n}\varepsilon\hat{n}) + \frac{a_2}{a_1}(\lambda\Delta) + \frac{a_3}{a_1}p_\infty\right] \qquad \text{(III.51)}$$

The first term in the brackets is the response due to shear deformation of the fracture. The second term is the response due to a volumetric (isotropic) strain of the fracture. The last term in the brackets is the response due to pore deformation in the formation. The multiplier T/(1+T) can be considered a tidal "transfer function" between the fluid pressure in the fracture and the measured fluid pressure in the well.

For a vertical bi-wing fracture whose spatial orientation depends only on strike, it is clear from equations (III.47') and (III.51) that in the most general case, the measured pressure response depends on four hydraulic parameters and one orientation parameter. The hydraulic parameters are: a_2, a_3, S_s/α, and Λ/L. For the case of a penny-shaped fracture in which dip is not constrained, the total number of free parameters is six. We have assumed that λ and μ are known and that the strain tensor can be estimated (see Chapter II). The number of free parameters is reduced for the case in which the formation permeability $k_r = 0$. In this case, $a_3 = 0$ and $a_1 = a_2$. For a vertical fracture, there are three free parameters and for an unconstrained orientation case, there are four free parameters. Since under most practical situations we usually have amplitude and phase information at the two tidal frequencies corresponding to the O_1 and M_2 tides, we have a total of four equations. Therefore, the solution will be unique only under the situation in which there is little or no drainage to the formation. If there is drainage, the solution will be under-determined. Recovery from the latter situation can

be accomplished if some of the hydraulic parameters are known a priori or if information at other tidal frequencies is available. The next chapter shows how this information can be obtained using a conventional pump test if pressure response data at other tidal frequencies is not available.

CHAPTER IV

INTEGRATION OF TIDAL RESPONSE WITH CONVENTIONAL PUMP TESTS FOR FRACTURE CHARACTERIZATION

The previous chapter indicates that, under some conditions, additional information will be required to calculate a unique fracture orientation solution. A conventional well pump test will, in principal, yield the needed information. Indeed, with proper test design, it will be possible to obtain the tidal pressure response information simultaneously with a conventional well pump test.

Another possible method for determining system hydraulic parameters from a pressure transient test is that of multi-frequency flow testing (Hanson, 1983). This method is a variation of conventional testing methods that may allow for better parameter resolution and can also be carried out simultaneously with tidal response monitoring.

As an example of the integration of tidal response with a conventional pump test, we consider a build-up test on a stimulated well with a vertical fracture (Cinco-Ley and Samaniego-V, 1981). A well is flowed for a time t_1 at a constant volume flow rate q and is then shut-in. The diffusion equation appropriate to this situation is (see Equation III.36):

$$\nabla_2^2 p - \frac{\mu}{k_f K_f}\left(1 + \frac{K_f}{b_f C}\right)\frac{\partial p}{\partial t} + \frac{k_r}{k_f b_f}\int_{-b_{f/2}}^{b_{f/2}} \frac{\partial^2 p}{\partial z^2}\, d_z = 0 \qquad \text{(IV.1)}$$

Rather than assuming an oscillating solution, as we did in equation III.38, we Laplace transform equation (IV.1) to obtain

$$\nabla_2^2 p - \frac{s\mu}{b_f k_f C}\left(1 + \frac{b_f C}{k_f}\right)\left(p - \frac{p\big|_{t=0}}{s}\right) - \frac{2k_r}{k_f b_f}\,\frac{s}{C_r}\left(p - \frac{p\big|_{t=0}}{s}\right) = 0 \qquad \text{(IV.2)}$$

where $p|_{t=0}$ is the reservoir pressure prior to the test. Equation (IV.2) is the Laplace transform equivalent to equation (III.41), with the exception that in the present case, the applied external normal stress $\sigma_n = 0$. Following a parallel development with that presented in Chapter III, we recast equation (IV.2) in terms of dimensionless parameters.

$$\nabla_2{}^2 p - \left[\frac{sd}{L^2\eta_{fD}} + \frac{2\sqrt{sd}}{L^2\sigma_{fD}}\right]\left[p - \frac{p|_{t=0}}{s}\right] = 0 \qquad \text{(IV.3)}$$

where d, η_{fD}, σ_{fD}, and L are defined in Chapter III. The conservation of mass boundary condition at the wellface is given by

$$\left.\frac{\partial p}{\partial \ell}\right|_{r=r_w} = \begin{cases} \Lambda, & 0 \leq t \leq t_1 \\ 0, & t > t_1 \end{cases} \qquad \text{(IV.4)}$$

where Λ will be defined later. The no-flow condition at the crack tip takes the form

$$\left.\frac{\partial p}{\partial \ell}\right|_{\ell=L} = 0 \qquad \text{(IV.5)}$$

The solution to equations (IV.3) - (IV.5), under the condition of linear flow within the fracture, is

$$p|_{r=r_w} - \frac{p|_{t=0}}{s} = \frac{\Lambda L}{s} \frac{(1-e^{-t_1 s})}{\sqrt{a_1}\tanh\left[\sqrt{a_1}(1-r_w/L)\right]} \qquad \text{(IV.6)}$$

where

$$\Lambda = \frac{q\mu}{2Hb_f k_f}$$

and

$$a_1 = a_2 + a_3$$

$$a_2 = \frac{ds}{\eta_{fD}} \qquad a_3 = \frac{2\sqrt{ds}}{\sigma_{fD}}$$

H is the height of the fracture at the wellface.

The pressure history from the beginning of flow at t=0 to time of shut-in $t=t_1$ and later can be obtained by calculating the inverse Laplace transform of equation (IV.6). An analytic expression for the inverse is likely to be difficult to obtain. Therefore, a numerical approach (Stehfest, 1969) is the most expedient. Since there is a discontinuity in $\partial p/\partial t$ at $t=t_1$, a direct numerical inverse will not obtain a reasonable precision near $t=t_1$. We therefore modify the numerical inverse procedure to take advantage of the time translation operator associated with the term $\exp(-t_1 s)$. Calling

$$G(s) = \frac{\Lambda L}{s} \frac{1}{\sqrt{a_1}\ \tanh[\sqrt{a_1}(1 - r_w/L)]}$$

it is easy to show that

$$\begin{aligned} p(t)\Big|_{r=r_w} - p(t=0) &= \mathcal{L}^{-1}[(1-e^{-t_1 s})G(s)] \\ &= \mathcal{L}^{-1}[G(s)]_t - \mathcal{L}^{-1}[G(s)]_{t-t_1} U(t-t_1) \end{aligned} \qquad \text{(IV.7)}$$

where U is the Heaviside step function defined by

$$U(t-t_1) = \begin{cases} 0, & t \leq t_1 \\ 1, & t > t_1 \end{cases}$$

and the subscripts t and $t-t_1$ indicate the time at which the Laplace inverse is to be evaluated. By this procedure, the function G(s) which is to be inverted numerically, is well-behaved.

A least-squares fit to equation (IV.7) to obtain the three system parameters ΛL, η_{fD}/d, and $\sigma_{fD}/(2\sqrt{d})$ will require a considerable computational effort unless some a priori information is known about the reservoir. However, under certain conditions, the number of free parameters in the model can be reduced from three to two. Under these conditions, it is a straightforward procedure to calculate the mean squared error, or chi-square, as a function of the remaining two parameters for a reasonable range of parameter values. An approximate value of the two unknown parameters can be obtained from the minimum of the chi-square function. These estimates can serve as an initial, or starting, value for a more refined inversion scheme such as a Marquardt-type scheme or a grid search. The constraints that decrease the number of model parameters from three to two are generated using the following relationships

$$\mathcal{L}^{-1} \lim_{s\to\infty} [s\,F(s)] = \lim_{t\to 0} f(t)$$

$$\mathcal{L}^{-1} \lim_{s\to 0} [s\,F(s)] = \lim_{t\to\infty} f(t),$$

it is easy to show from equation (IV.6) that

(1) $$\lim_{t\to\infty} \frac{dp}{dt} = \mathcal{L}^{-1}\left[\frac{\Lambda L \sigma_{fD}(1-e^{-t_1 s})}{2\sqrt{d}\ \sqrt{s}}\right]$$

or $$\lim_{t\to\infty} \left\{\frac{\sqrt{\pi}\ dp/dt}{1/\sqrt{t} - 1/\sqrt{(t-t_1)}}\right\}_{t>t_1} = (\Lambda L)\ \frac{\sigma_{fD}}{2\sqrt{d}} \qquad \text{(IV.8a)}$$

$$\lim_{t\to\infty} \left\{\sqrt{\pi t}\ \frac{dp}{dt}\right\}_{t<t_1} = (\Lambda L)\ \frac{\sigma_{fD}}{2\sqrt{d}} \qquad \text{(IV.8b)}$$

(2) $$\lim_{t\to 0} \frac{dp}{dt} = \mathcal{L}^{-1}\left[\Lambda L\left\{\frac{\sigma_{fD}}{2\sqrt{d}}\right\}^{\frac{1}{2}} s^{-\frac{1}{4}}\right]$$

or $$\lim_{t\to 0} \left\{(4t)^{3/4}\ \frac{dp}{dt}\right\}_{t<t_1} = \Lambda L\left\{\frac{\sigma_{fD}}{2\sqrt{d}}\right\}^{\frac{1}{2}} \qquad \text{(IV.8c)}$$

We have used the time derivative of pressure to determine the constraints in order to eliminate the requirement of knowing the initial static reservoir pressure. If this information is known, the above conditions of constraint are easily modified.

Equations (IV.8a,b) represent the situation in which linear formation flow regime has been achieved (see Cinco-Ley and Samaniego-V, 1981). This condition is exhibited under the condition of high fracture conductivity, $\sigma_{fD} \geq 300$. The pressure within the fracture equilibrates rapidly and subsequent pressure changes are due to drainage from the formation. Equation (IV.8c) represents the bilinear flow regime in which a linear flow occurs simultaneously in both the formation and the fracture. A detailed description of the conditions under which bilinear flow can be expected is given by Cinco-Ley and Samaniego-V (1981).

As an example, we consider a vertical fracture of half-length L = 100 m, width by b_f = 1 mm, and height H = 50 m. The asperity incompressibility C = 4×10^8 pa/m and the formation fluid is water. The formation has a permeability k_r = 10 md and a porosity-total compressibility product $\phi C_t = 7.3 \times 10^{-11}$ pa^{-1}. The well is flowed for 24 hours at a volume rate of 10 m^3/hr and is then shut-in. Under these conditions, σ_{fD} = 83.3, η_{fD} = 241.5, d = 20.1 hr, and ΛL = 4.8 psi. Thus, the three model parameters are:

$$\frac{\sigma_{fD}}{2\sqrt{d}} = 9.29 \text{ hr}^{-\frac{1}{2}}$$

$$\frac{\eta_{fD}}{d} = 12.02 \text{ hr}^{-1}$$

$$\Lambda L = -4.8 \text{ psi}$$

Figure 4.1a shows the pressure history and Figure 4.1b shows the time derivative of the pressure history based on the numerical Laplace transform inver-

sion of equation (IV.6). Figure 4.2a shows the evaluation of the constraint given by equation (IV.8a) for the limit of linear formation flow. From this figure, it is clear that the plotted function is approaching asymptotically a value roughly -44.5 psi/$\sqrt{hr}$. The actual value is given by:

$$(\Delta L)\left(\frac{\sigma_{fD}}{2\sqrt{d}}\right) = (-4.8\text{psi})(9.29\text{hr}^{-\frac{1}{2}}) = -44.6 \text{ psi}/\sqrt{\text{hr}}$$

Figure 4.2b is a plot of the constraint given by equation (IV.8c). From this figure, we conclude that, at least prior to shut-in, the bi-linear flow regime is not obtained. This observation is substantiated by Figure 4.2c, which is a plot of the constraint given by equation (IV.8b). It is clear that, prior to shut-in, the fracture conductivity is large enough for the flow regime to approach a linear formation flow. This figure shows that the constraint given by equation (IV.8b) asymptotically approaches -44.1 psi/$\sqrt{hr}$ where again the actual value is -44.6 psi/$\sqrt{hr}$.

A second example is presented which is identical to the example given above with the exception that the fracture half-length L is increased from 100 m to 1000 m. With this modification, $\sigma_{fD} = 8.33$, $\eta_{fD} = 241.5$, $d = 2.01 \times 10^{4}$ hrs, and $\Delta L = -48$ psi. Thus, the three model parameters are

$$\frac{\sigma_{fD}}{2\sqrt{d}} = 2.938 \times 10^{-2} \text{ hr}^{-\frac{1}{2}}$$

$$\frac{\eta_{fD}}{d} = 1.2 \times 10^{-2} \text{ hr}^{-1}$$

$$\Delta L = -48 \text{ psi}$$

Figure 4.3a shows the pressure history and Figure 4.3b the time derivative of the pressure history under these conditions. Again, we have plotted the equations of constraint given by equations (IV.8a,b,c). Figure 4.4a shows the linear formation flow constrain given by equation (IV.8a). It is clear that

the asymptotic value of $(\Lambda L)(\sigma_{fD}/\sqrt{d}) = 1.41$ has not been reached after 300 hours into the test. Because of the large fracture length, there is probably still a component of the bilinear flow regime contaminating this information. Bilinear flow is clearly indicated by Figure 4.4b which is a plot of the constraint given by equation (IV.8c). The discrepancy between the theoretical asymptotic value

$$(\Lambda L)\left(\frac{\sigma_{fD}}{2\sqrt{d}}\right)^{\frac{1}{2}} = -8.23 \text{ psi}\cdot\text{hr}^{-\frac{1}{4}}$$

and that shown in the figure, namely $-7.1 \text{ psi}\cdot\text{hr}^{-\frac{1}{4}}$, is likely due to the approximation inherent in a numerical Laplace transform inversion.

The fact that the bilinear flow dominates prior to shut-in is substantiated by Figure 4.4c which shows a plot of the constraint given by equation (IV.8b). The theoretical asymptotic value, which is not reached prior to shut-in, is

$$(\Lambda L)\left(\frac{\sigma_{fD}}{2\sqrt{d}}\right) = -1.41 \text{ psi}/\sqrt{\text{hr}}$$

The examples presented above are primarily for illustrating the fact that the flow parameters for a fractured reservoir can in principle be obtained given some realistic model for the reservoir. We have chosen a vertical bi-wing fracture model to be consistent with the tidal strain response model given in Chapter III. It is not surprising, therefore, that the model presented here shares the same hydraulic parameters as the tidal response model. Given an evaluation of these parameters by a conventional pump test, the non-uniqueness of the fracture orientation model given by equation (III.47) can be overcome.

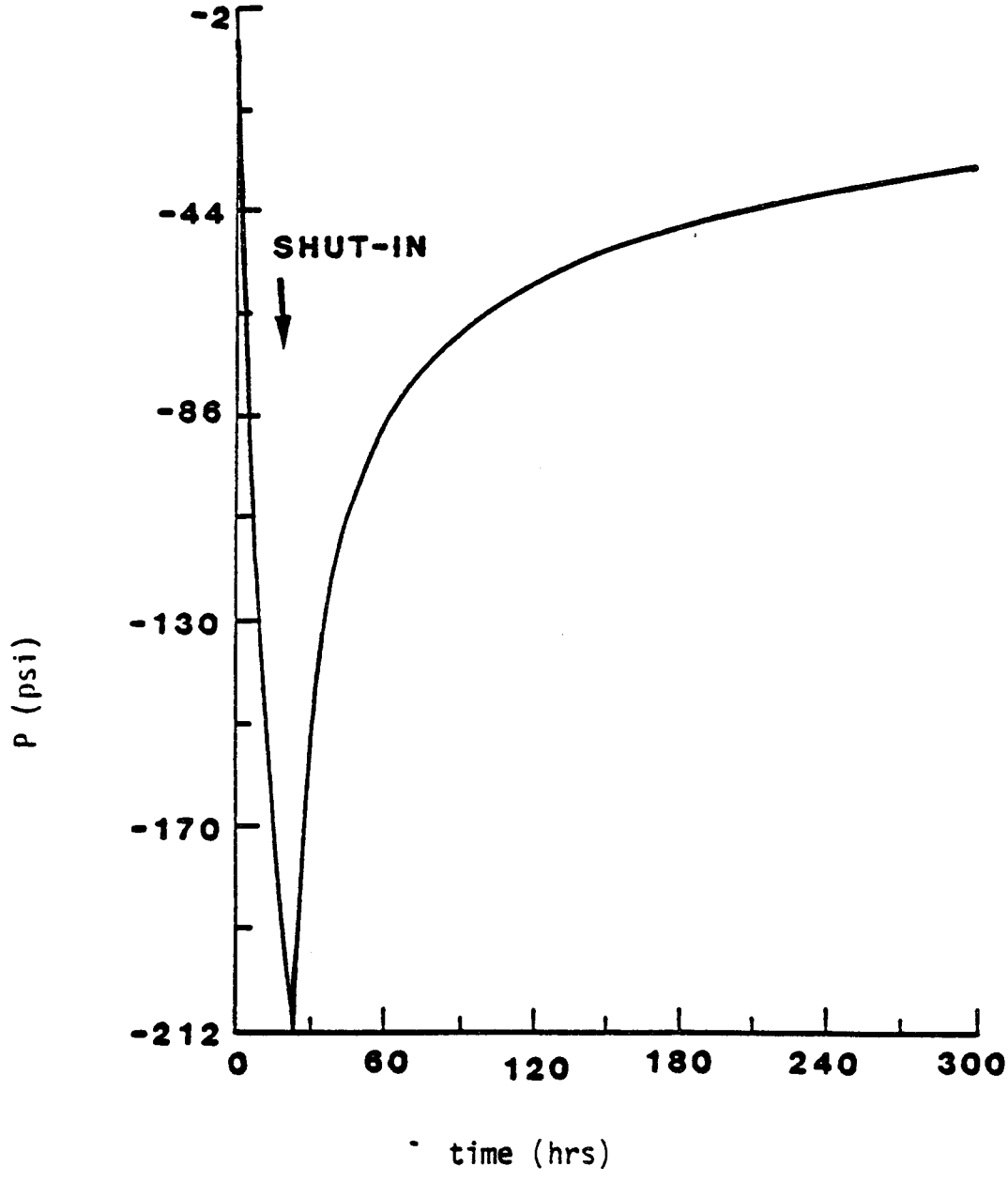

Figure 4.1a. Pressure history during a drawdown-buildup pressure transient test. Well is shut-in at t = 24 hours and L = 100 m.

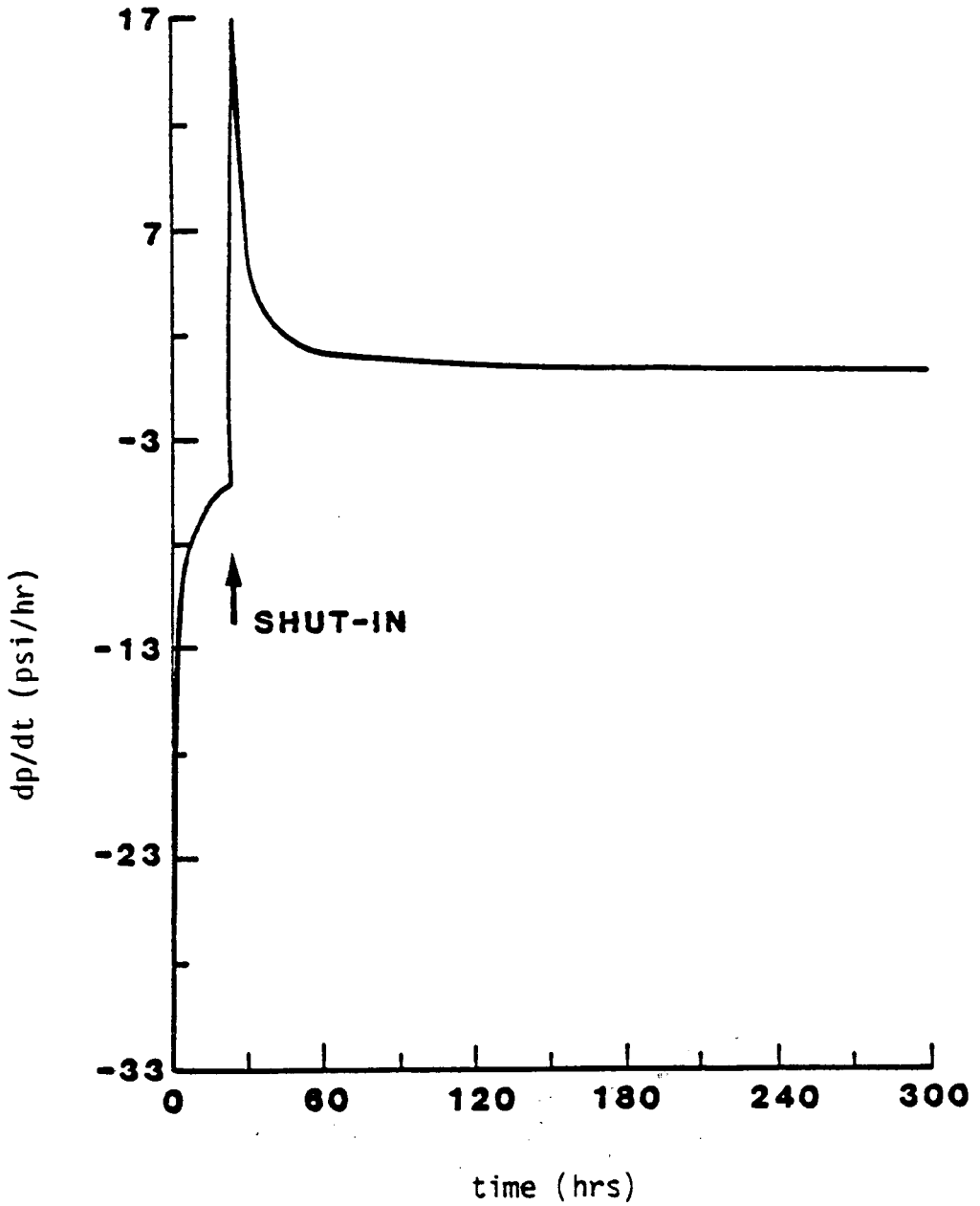

Figure 4.1b. Time derivative of data shown in Figure 4.1a.

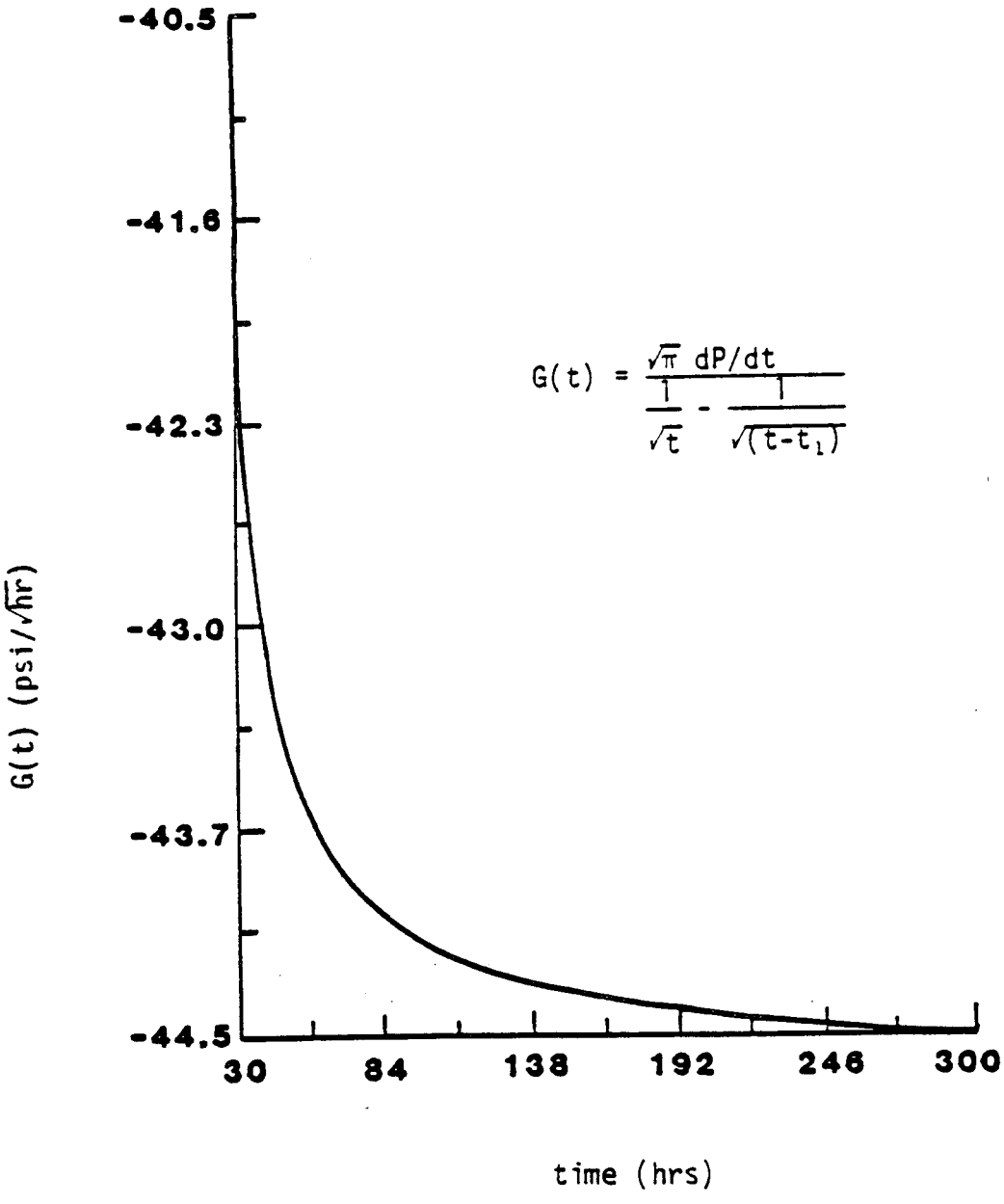

Figure 4.2a. Linear formation flow constraint given in equation (IV.8a).

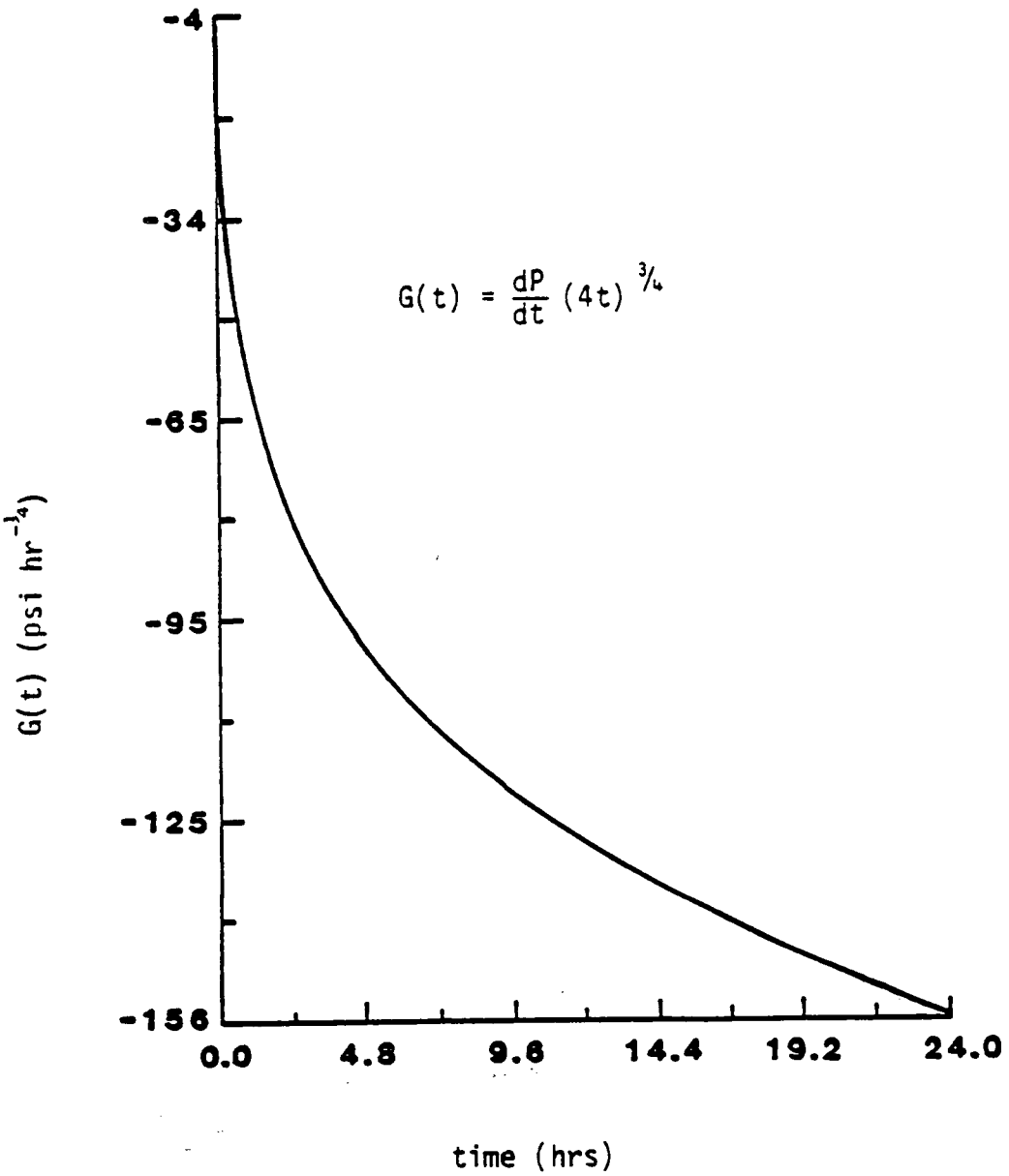

Figure 4.2b. Bilinear flow constraint after shut-in given by equation (IV.8c).

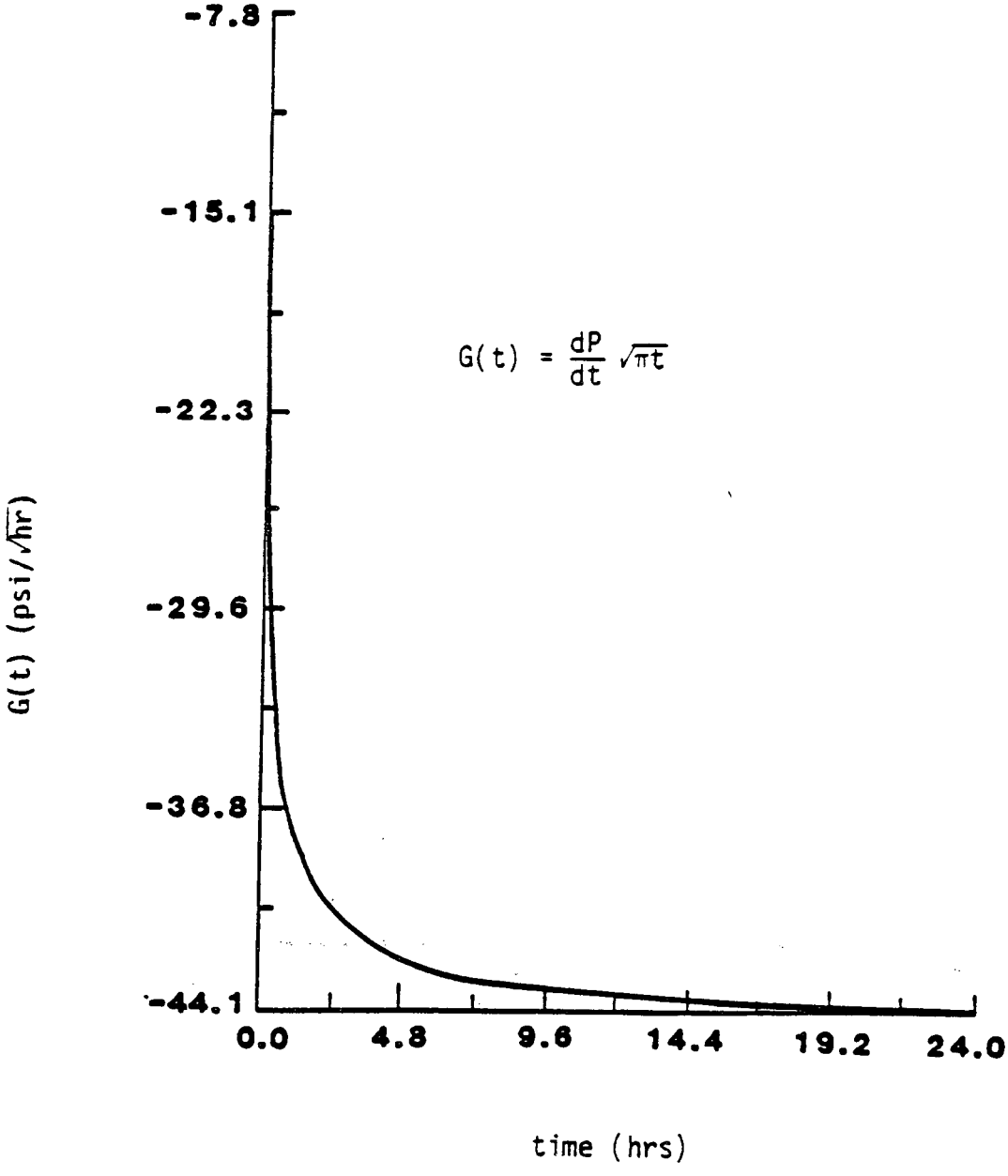

Figure 4.2c. Bilinear flow constraint before shut-in given by equation (IV.8b).

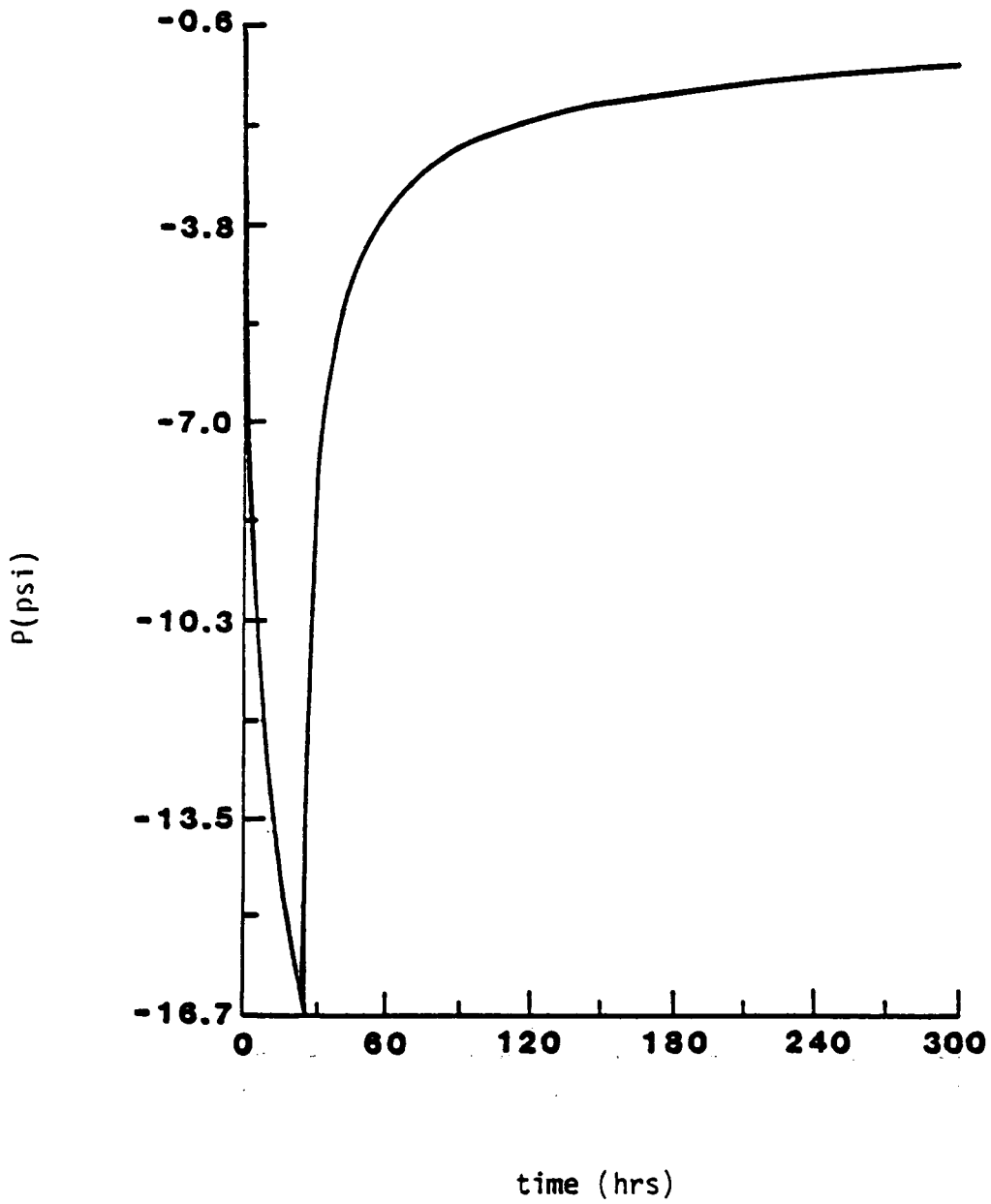

Figure 4.3a. Pressure history during a drawdown-buildup pressure transient test. Well is shut-in at t = 24 hours and L = 1000 m.

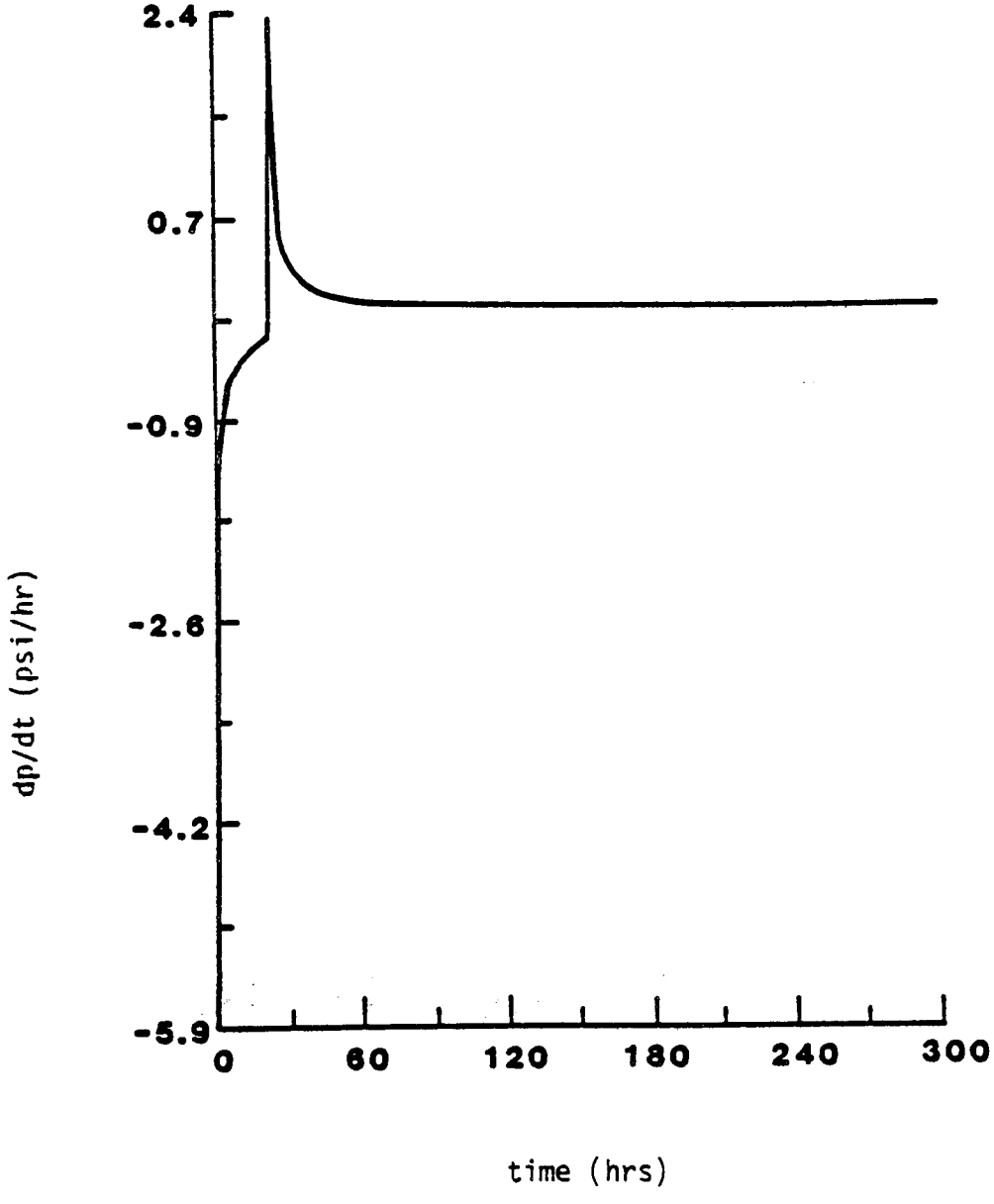

Figure 4.3b. Time derivative of data shown in Figure 4.3a.

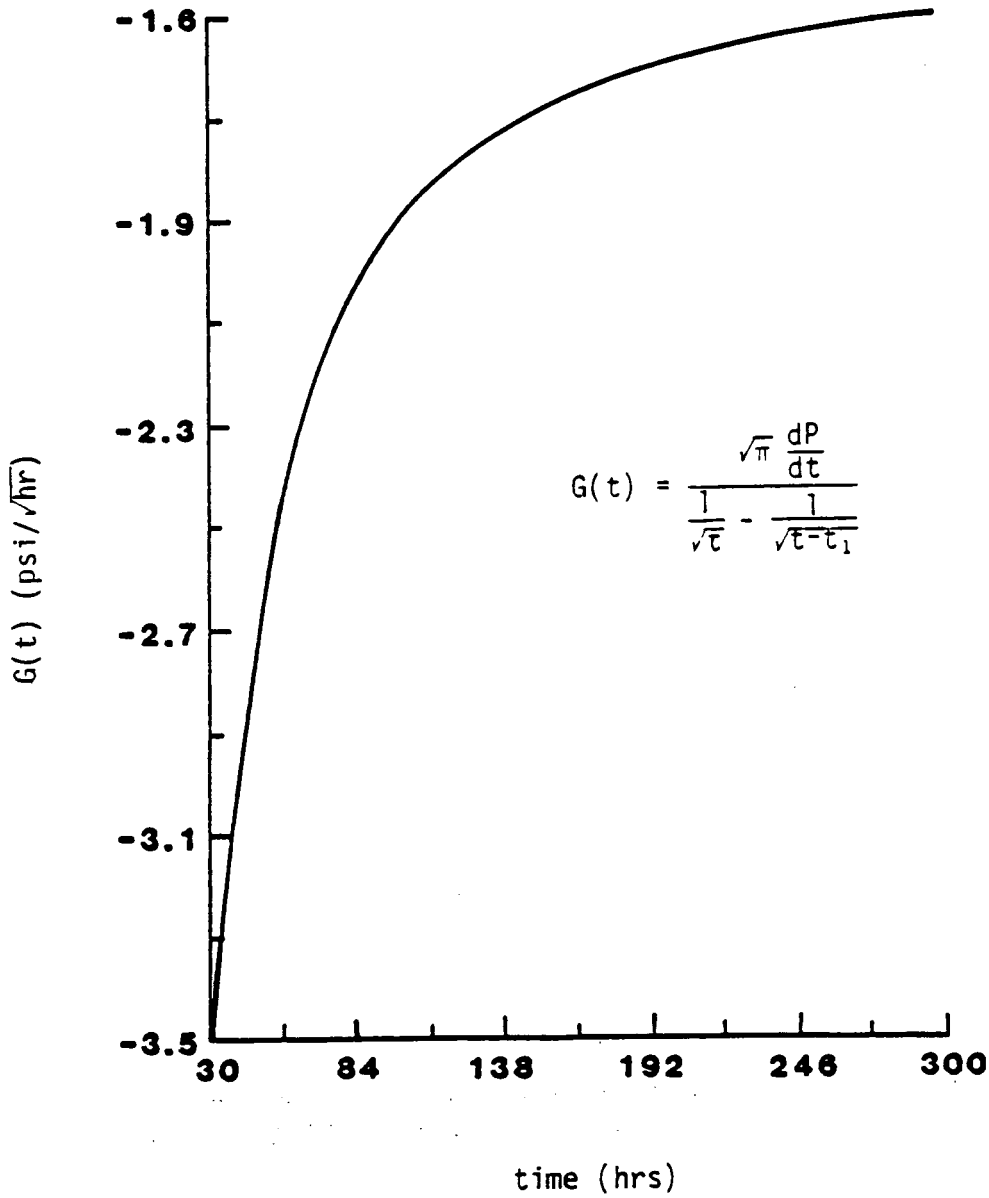

Figure 4.4a. Linear formation flow constraint given in equation (IV.8a).

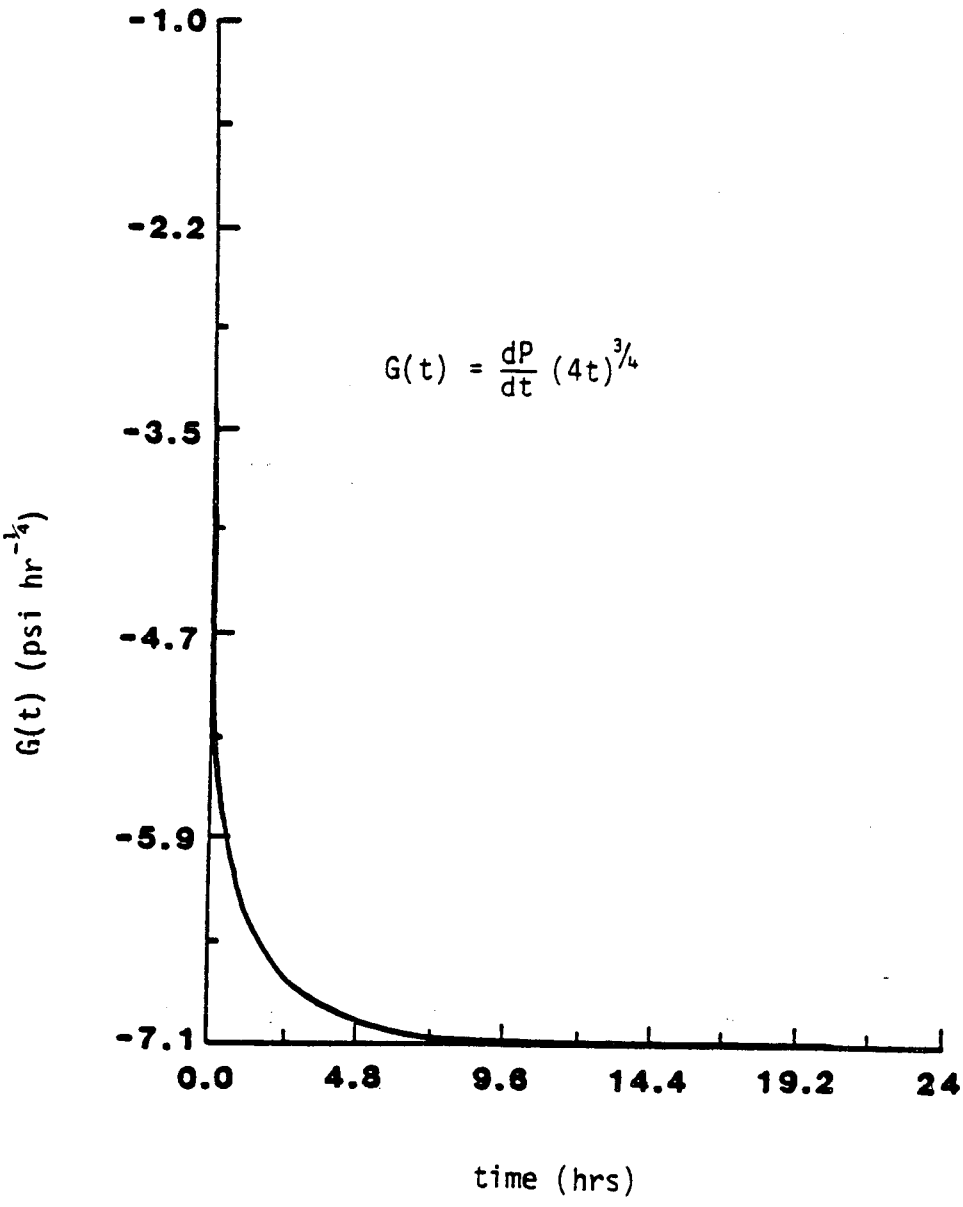

Figure 4.4b. Bilinear flow constraint after shut-in given by equation (IV.8c).

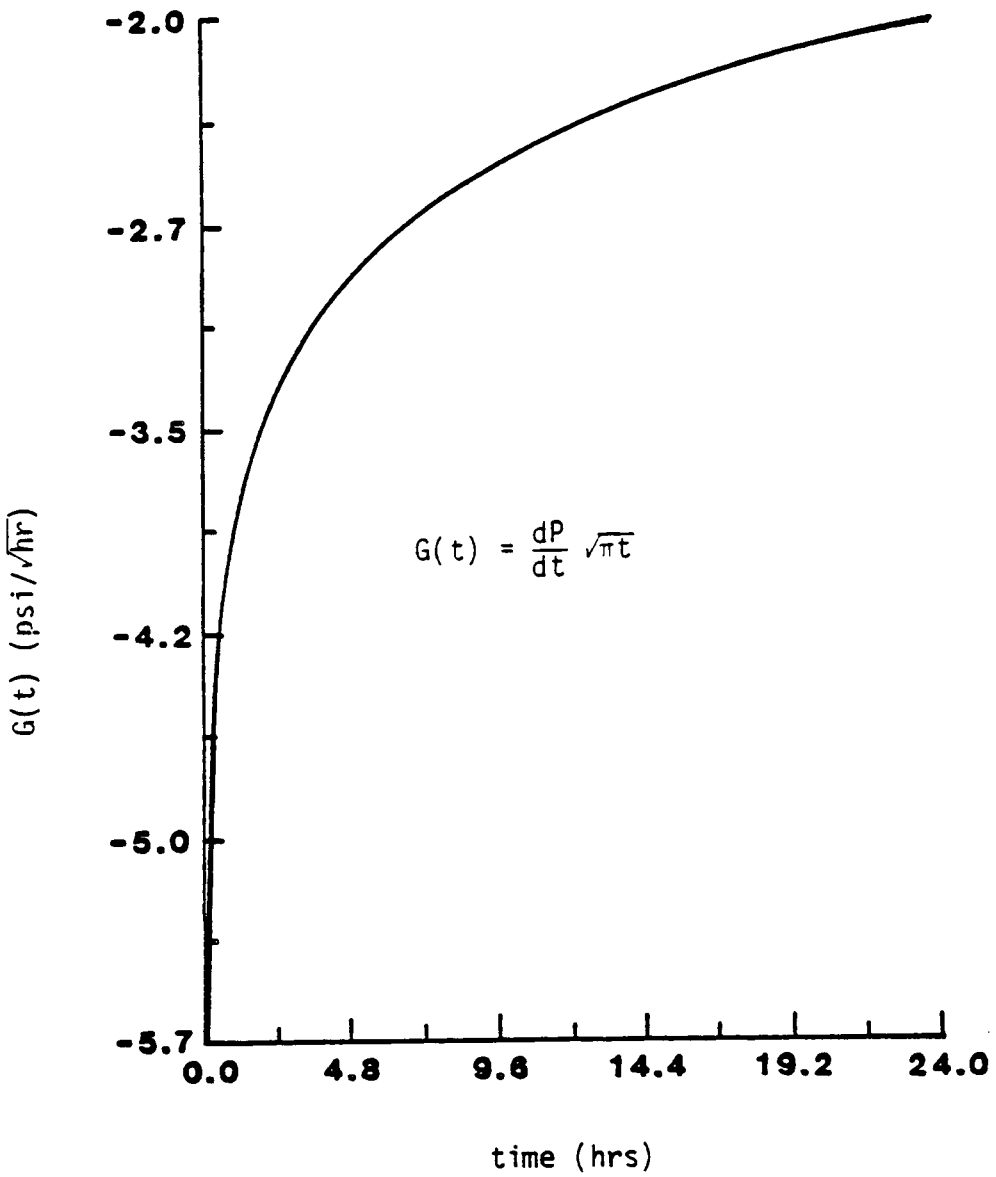

Figure 4.4c. Bilinear flow constraint before shut-in given by equation (IV.8b).

CHAPTER V

SPECTRAL ANALYSIS, CORRELATION, AND ERROR ESTIMATION

Extraction of information from signals of tidal origin requires the use of Fourier spectral analysis methods. However, due to the fact that the tidal spectrum is a line spectrum with all energy contained within a finite Dirac delta distribution (ignoring the small non-linearity introduced by the ocean tide loading effects), certain modifications of conventional spectral analysis methods are required. These modifications make use of the fact that the tidal frequencies are known with great precision which consequently reduces the number of degrees of freedom of the problem and therefore improves the tidal amplitude and phase estimates. This improvement of tidal signal resolution was first discussed by Munk and Hasselman (1964) for the simple case of two neighboring spectral lines. An extension of this approach to the full tidal spectrum is discussed in some detail by Godin (1972). One can show that this approach can improve signal resolution over the classical Rayleigh resolution criterion. The latter states that, for a signal record length L, two spectral lines separated in frequency by Δf can be resolved if $L\Delta f \geqq 1/2$.

In the following, we will present a discussion of line spectral analysis, beginning with the idealized case of a continuous signal of finite duration followed by the case of a discretely sampled signal of finite duration. Assuming that, in the practical case, some amount of noise will be present in the signal, a formulation of the variance-covariance matrix and the subsequent translation to uncertainty in the amplitude and phase for each tidal constituent will be presented.

We will first begin with the ideal case of a noiseless continuous tidal signal $f(t)$ on the time interval $-L/2 \leqq t \leqq L/2$ consisting of N discrete fre-

quencies $\{\omega_1, \omega_2, \ldots, \omega_N\}$ with amplitude and phase distribution $\{a_1,\phi_1; a_2,\phi_2; \ldots; a_N,\phi_N\}$. The signal can be represented by the sum:

$$f(t) = \sum_{n=1}^{N} a_n \mathrm{Cos}(\omega_n t + \phi_n) \tag{V.1}$$

The finite Fourier transform of f(t) evaluated at frequency ω_k is given by:

$$\tilde{F}(\omega_k) = \frac{2}{L} \int_{-L/2}^{L/2} e^{i\omega_k t} f(t)\, dt \tag{V.2}$$

which, upon insertion of equation (V.1), obtains the following expression:

$$\tilde{F}(\omega_k) = \frac{2}{L} \sum_{n=1}^{N} a_n \left[e^{i\phi_n} \frac{\mathrm{Sin}[(\omega_k + \omega_n)\, L/2]}{(\omega_k + \omega_n)} + e^{-i\phi_n} \frac{\mathrm{Sin}[(\omega_k - \omega_n)\, L/2]}{(\omega_k - \omega_n)} \right] \tag{V.3}$$

If we now define:

$$Z_n = a_n e^{i\phi_n} \tag{V.4}$$

$$\vec{Z} = \{Z_1, Z_2, \ldots, Z_N\}^T \tag{V.5}$$

$$\vec{F} = \{\tilde{F}(\omega_1), \tilde{F}(\omega_2), \ldots, \tilde{F}(\omega_N)\}^T \tag{V.6}$$

$$A^{\pm}_{kn} = \frac{\mathrm{Sin}[(\omega_k \pm \omega_n)\, L/2]}{(\omega_k \pm \omega_n)\, L/2} \tag{V.7}$$

Equation (V.3) can be recast as a set of N equations and N unknowns, given by the matrix equation:

$$A^+ \vec{Z} + A^- \vec{Z^*} = \vec{F} \tag{V.8}$$

where the elements of A^+ and A^- are given by equation (V.7) and $\vec{Z^*}$ is the complex conjugate of $\vec{Z}$. The unknowns, namely amplitude and phase the tidal constituents, are contained in the complex vector $\vec{Z}$.

Separating the real and imaginary parts of equation (V.8),

$$\begin{aligned} \text{Re } \vec{F} &= (A^+ + A^-) \text{ Re } \vec{Z} \\ \text{Im } \vec{F} &= (A^+ - A^-) \text{ Im } \vec{Z} \end{aligned} \tag{V.9}$$

The complex vector $\vec{Z} = \text{Re } \vec{Z} + i\text{Im } \vec{Z}$ can be written as:

$$\vec{Z} = H^+ \text{ Re } \vec{F} + i\, H^- \text{ Im } \vec{F} \tag{V.10}$$

where

$$H^+ = (A^+ + A^-)^{-1} \tag{V.11}$$

$$H^- = (A^+ - A^-)^{-1}$$

Equation (V.10) gives the vector of N unknown complex tidal constituents in terms N complex finite Fourier transforms and two real symmetric matrices H^+ and H^- that serve to couple F with $\vec{Z}$. The finite Fourier transforms can easily be estimated using numerical integration methods. It is important to point out that the coupling coefficients depend on the duration L of the signal and the location of the frequencies in the tidal spectrum, as indicated by equation (V.7). It is also noted that, as the duration of the signal L gets large, that

$$A^+_{kn} \to 0 \quad \text{and} \quad A^-_{kn} \to \delta_{kn}$$

and thus

$$H^+ \to I \quad \text{and} \quad H^- \to -I$$

where δ_{kn} is the Kronecker delta and I is the unity matrix. In this limit,

$$\vec{Z} \to \vec{F^*} \tag{V.12}$$

and the complex tidal constituents become uncoupled from each other. It is clear from the above that, if a conventional Fourier analysis of a <u>finite</u> length of data is carried out for the purpose of extracting the tidal constit-

uents (see equation (V.2)), an error in the estimates will be found due simply to the finite length of data independent of any noise that may also exist on the record. This is discussed in some detail by Blair (1979). Therefore, equation (V.10) should be used over equation (V.12) for the purpose of extracting tidal information from a record.

If the tidal signal is a discretely sampled function and not a continuous function, the form of equation (V.10) is maintained although the expression for the matrix elements $A^{\pm}_{kn}$ given by equation (V.7) is modified to take into account the discrete sampling. The derivation of this expression is similar to that presented for the continuous case although the algebra is somewhat more involved. Therefore, the results will simply be stated:

$$\tilde{F}(\omega_k) = \frac{2\Delta t}{L} \sum_{n=-M}^{M} f(n\Delta t) e^{in\Delta t \omega_k} \qquad (V.2')$$

$$A^{\pm}_{kj} = \frac{\Delta t}{L} \frac{\mathrm{Sin}[(\omega_k \pm \omega_j)\, L/2]}{\mathrm{Sin}[(\omega_k \pm \omega_j)\, \Delta t/2]} \qquad (V.7')$$

where $L=(2M-1)\Delta t$ and the solution vector $\vec{Z}$ is obtained by equations (V.10) and (V.11). It is evident from equation (V.7') that as $\Delta t \to 0$, the expression for $A^{\pm}_{kn}$ approaches that for the continuous case, namely equation (V.7).

The variance-covariance matrix, which contains the necessary information to estimate the uncertainties in the computed amplitude and phase of the tidal constituents, can be formulated relatively easily. The formulation presented here assumes that the noise, $\eta(t)$, is "white" -- that is, the amplitude of its ensemble average is uniformly distributed with respect to frequency. If the noise is random, it is automatically "white" noise (Goldman, 1968). We assume that the noise-contaminated signal is given by:

$$g(t) = f(t) + \eta(t) \qquad (V.13)$$

where f(t) is given by equation (V.1). Assuming again for the purpose of illustration a continuous signal, as opposed to a discretely sampled signal, we may define:

$$\vec{G} = A^+ \vec{Z} + A^- \vec{Z}^* + \frac{2}{L} \int_{-L/2}^{L/2} \left[e^{i\omega_k t} \eta(t)\, dt \right]_{col} \qquad (V.14)$$

where we have simply replaced f(t) with g(t) in equation (V.2). The last term in brackets is a column vector whose elements range from k = 1 to k = N. $\vec{Z}$ is again the true spectrum (no noise) of the tidal record. If $\vec{r}$ is defined as the measured value of the spectral constituents, then we can also write:

$$\vec{G} = A^+ \vec{r} + A^- \vec{r}^* \qquad (V.15)$$

Defining an error vector between the true values and the estimated values of the spectral constituents as:

$$\vec{\delta r} = \vec{r} - \vec{Z}$$

we can use equations (V.14) and (V.15) to derive the following expressions:

$$\begin{aligned} \text{Re } \vec{\delta r} &= \frac{2}{L} (A^+ + A^-)^{-1} \int_{-L/2}^{L/2} \left[\text{Cos } (\omega_k t)\, \eta(t)\, dt \right]_{col} \\ \text{Im } \vec{\delta r} &= \frac{2}{L} (A^+ - A^-)^{-1} \int_{-L/2}^{L/2} \left[\text{Sin } (\omega_k t)\, \eta(t)\, dt \right]_{col} \end{aligned} \qquad (V.16)$$

where the terms in brackets are column vectors whose elements range from k=1 to k=N. The ensemble averages of the following expressions are now obtained:

$$\begin{aligned} &(a)\ \langle (\text{Re } \vec{\delta r})_j\ (\text{Re } \vec{\delta r})_k \rangle \\ &(b)\ \langle (\text{Im } \vec{\delta r})_j\ (\text{Im } \vec{\delta r})_k \rangle \\ &(c)\ \langle (\text{Re } \vec{\delta r})_j\ (\text{Im } \vec{\delta r})_k \rangle \end{aligned} \qquad (V.17)$$

with the assumptions that the noise is a stationary time series and is also "white", then the ensemble average of $\eta(t)\eta(t')$ is given by:

$$\langle \eta(t)\ \eta(t') \rangle = 2\pi\ S_o(\omega)\ \delta(t-t')$$

where $S_o(\omega)$ is the noise power spectrum. If we assume that the signals are band-limited such that no energy exists beyond the Nyquist band, then

$$S_o(\omega) = \frac{v^2 \Delta t}{4\pi} \tag{V.18}$$

where v^2 is the mean-squared error of the signal and Δt is the sampling rate. With the same algebra, it can be shown that the ensemble averages of equations (V.17) are given by:

$$\begin{aligned}
\langle (\mathrm{Re}\ \vec{\delta r})_j\ (\mathrm{Re}\ \vec{\delta r})_k \rangle &= \frac{v^2 \Delta t}{L} H_{jk}^{+} \quad , \ j,k = 1,N \\
\langle (\mathrm{Im}\ \vec{\delta r})_j\ (\mathrm{Im}\ \vec{\delta r})_k \rangle &= \frac{v^2 \Delta t}{L} H_{jk}^{-} \quad , \ j,k = 1,N \\
\langle (\mathrm{Re}\ \vec{\delta r})_j\ (\mathrm{Im}\ \vec{\delta r})_k \rangle &= 0 \qquad\quad , \ j,k = 1,N
\end{aligned} \tag{V.19}$$

where $H^{\pm}$ is given by equation (V.11). For a discretely sampled signal, the definition for $A^{\pm}$ given by equation (V.7') is used. v^2 can be estimated by:

$$v^2 = \frac{1}{L} \int_{-L/2}^{L/2} [g(t) - f(t)]^2\ dt \tag{V.20}$$

where f(t) is the least-squares approximation of f(t) using the computed tidal constituents $\vec{r}$. It is easily shown that $\vec{r}$ is the best estimate of $\vec{Z}$ in the least-squares sense.

Expressions given by equation (V.19) represent the variance-covariance in the real and imaginary components of the N spectral estimates. It is important to point out that, based on these equations, the uncertainty of the

spectral estimates can be reduced either by increasing the sampling rate (i.e. decreasing Δt) or increasing the duration L of the record length. Therefore, at least in principle, signals of tidal origin, or any stationary repetitive signal for that matter, can be resolved regardless of the background noise if the sampling rate is sufficiently fast or the record length is made sufficiently long.

Probabilities can be assigned to the uncertainties in the spectral estimates if a form for the probability density function is assumed. We have assumed a two-dimensional normal distribution where the two random variables, namely $(\text{Re } \vec{\delta r})_j$ and $(\text{Im } \vec{\delta r})_j$, are uncorrelated. The latter is reflected in equation (V.19) where the ensemble average of the product of these two variables is found to be zero.

The probability of finding a point (X,Y) in the ellipse defined by the equation:

$$\left[\frac{X - \mu_x}{\sigma_x}\right]^2 + \left[\frac{Y - \mu_y}{\sigma_y}\right]^2 = k^2 \qquad \text{(V.21)}$$

is equal to $1-e^{-k^2}$. For the case under consideration, (μ_x, μ_y) are the expectations of the real and imaginary parts of a given tidal constituent and (σ_x^2, σ_y^2) are the variances of these estimates, respectively. Therefore, at a confidence level ξ, ranging from 0 to 1, the axes of the error ellipse in the complex plane have half-lengths of:

$$a = \sqrt{-2 \ln(1-\xi)}\, \sigma_x$$

$$b = \sqrt{-2 \ln(1-\xi)}\, \sigma_y$$

where

$$\sigma_x = \left[\frac{v^2 \Delta t}{L} H_{jj}^{+}\right]^{\frac{1}{2}}$$

$$\sigma_y = \frac{v^2 \Delta t}{L} H_{jj}^{-\frac{1}{2}}$$

for the j^{th} tidal constituent. Figure 5.1 serves to illustrate this. Uncertainties in amplitude and phase of the j^{th} tidal constituent at the confidence level ξ can easily be obtained by numerically mapping the above error ellipse from the complex domain (real, imaginary axes) to the amplitude-phase domain.

In the practical case, the measured pressure record will include effects due to barometric loading and well pumping. These effects must be removed from the measured pressure record prior to carrying out the spectral analysis procedure discussed above. A somewhat involved, but straightforward procedure, is used to accomplish this. Figure 5.2 shows a data analysis flow chart from data measurement through data interpretation. We begin by assuming that the measured fluid pressure data can be represented by:

$$p(t) = f(t) + f_b(t) + f_p(t) + \eta(t) \qquad (V.22)$$

where f, f_b, f_p, and η are the tidal, barometric, pumping, and random noise constituents, respectively. In general, f_b and f_p will have fluctuations with longer periods and larger amplitudes than f. We therefore fit a trend function, using either spline and/or least-squares polynomial fitting, to $p(t)$ to obtain a first approximation to the sum $f_b(t) + f_p(t)$. This trend function is then subtracted from $p(t)$ to obtain a first estimate of $f(t) + \eta(t)$. Using this first estimate of the tidal component, we carry out a tidal line spectral analysis as discussed previously to obtain a first estimate of the amplitudes and phases of the tidal constituents. This signal in turn is subtracted from the measured fluid pressure data to obtain a second estimate $q(t)$ of the sum of the pumping and barometric effects. The barometric loading effect at the tidal frequencies will of course be minimized in this signal. In a similar

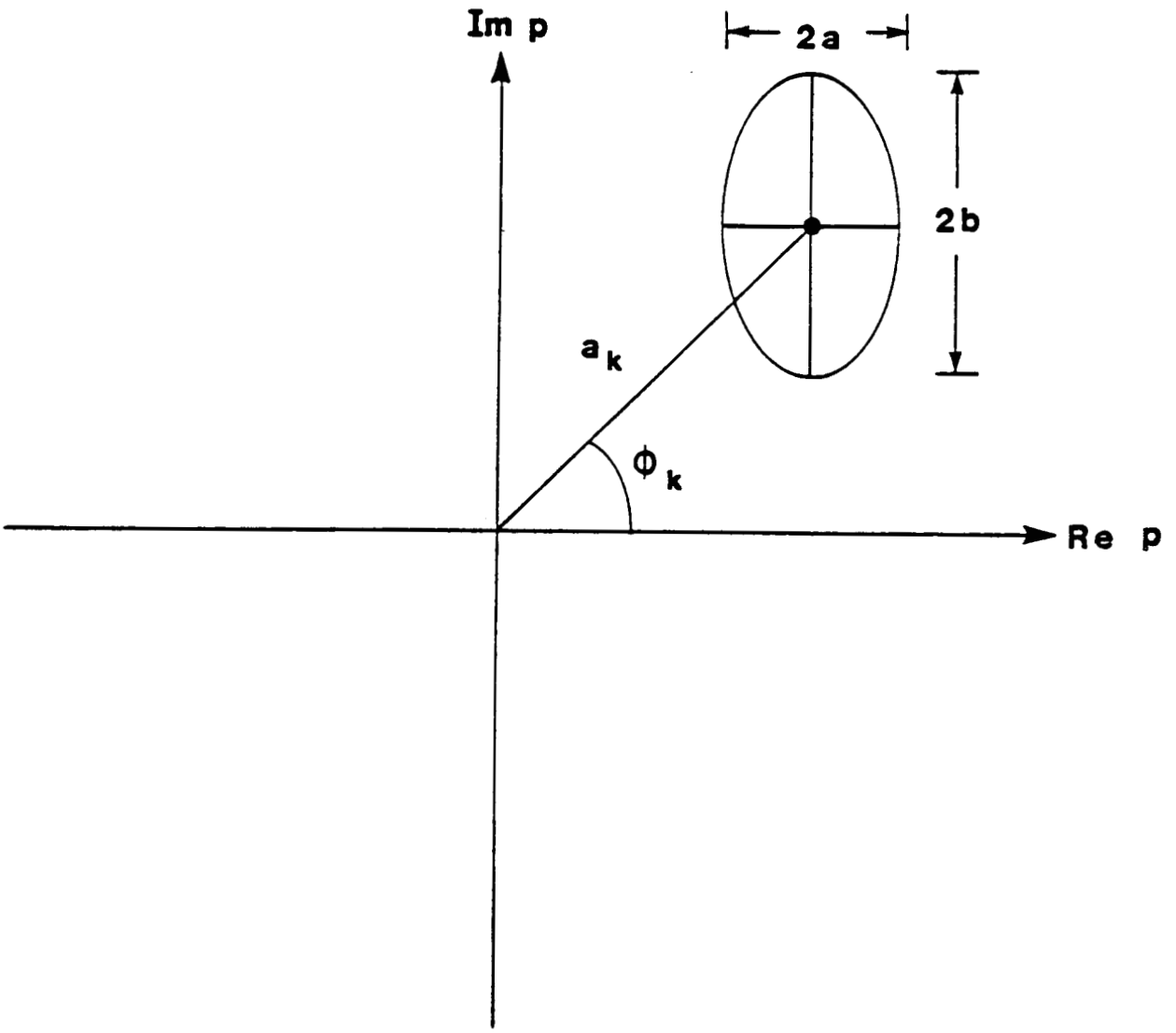

Figure 5.1. Example of uncertainty error ellipse of a tidal constituent in the complex plane.

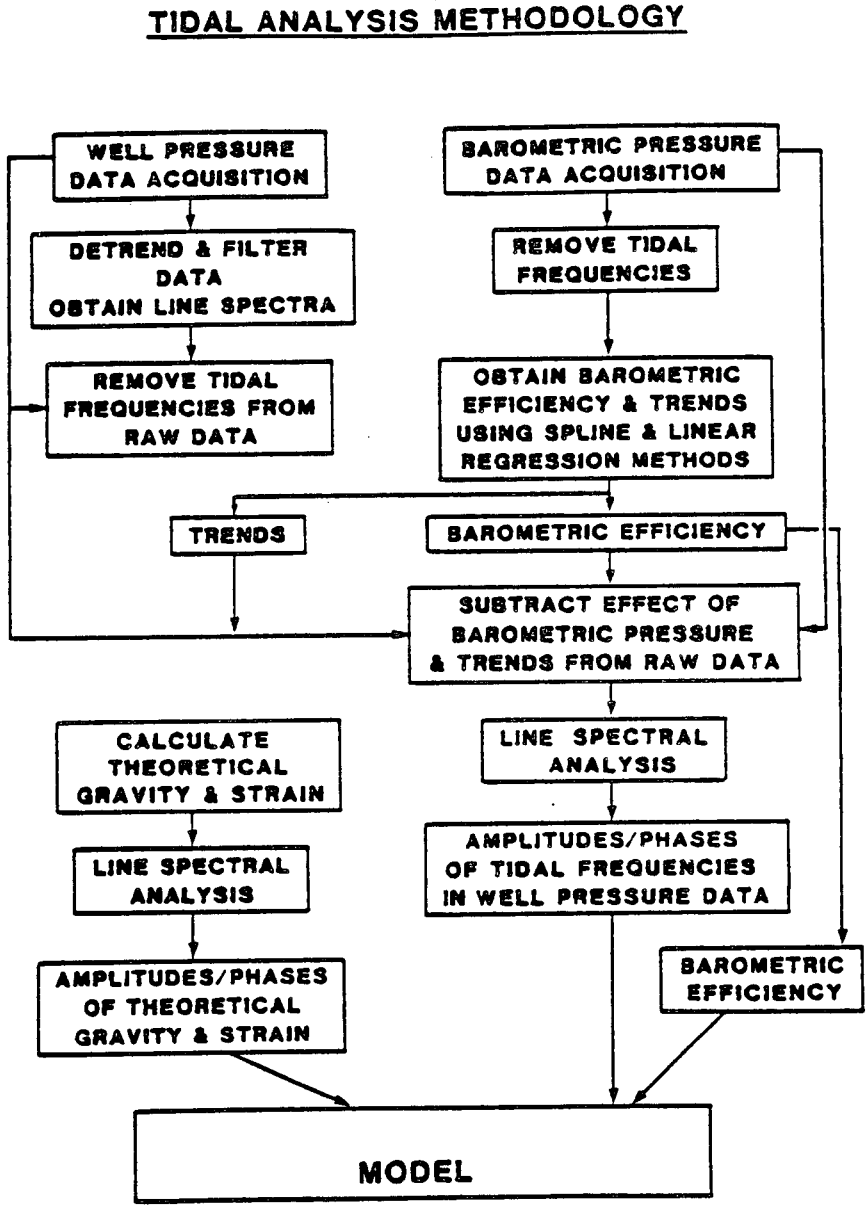

Figure 5.2. Flow chart showing the various stages of tidal data processing and analysis.

fashion, we also remove from the measured barometric pressure $p_b(t)$ signals at the tidal frequencies. The resulting signal r(t) will be used, in conjunction with q(t) to obtain estimates of the pumping and barometric effects. This is carried out by minimizing the following integral:

$$I = \int_{t_1}^{t_2} [q(t) - BE \cdot r(t) - S_N(t)]^2 \, dt \qquad (V.23)$$

with respect to the barometric efficiency, BE. S_N is an N-knot spline. The minimization is carried out by choosing a value of BE, evaluating $q(t) - BE \cdot r(t)$, fitting an N-knot spline to this function, and evaluating the mean squared error between $q(t) - BE \cdot r(t)$ and S_N over the recording period $[t_1, t_2]$. The process is repeated for various values of BE until I is a minimum. The result yields: 1) an estimate of the barometric efficiency BE, and 2) an estimate S_N of the pumping component. It is emphasized that we have assumed that the permeability of the reservoir is sufficiently high so that there will be no time lag between the applied barometric load and the fluid pressure response. Criteria for this assumption are given in Chapter III. An uncertainty in the barometric efficiency BE can be estimated by fitting a straight line to the parametric equation

$$y(t) = q(t) - S_N(t)$$
$$x(t) = r(t)$$

and calculating an uncertainty in the slope BE.

Finally, the pressure signal constituent associated with the tidal response is obtained according to:

$$f(t) + \eta(t) = p(t) - BE \cdot p_b(t) - S_N(t)$$

CHAPTER VI

CASE STUDY - RAFT RIVER GEOTHERMAL AREA

The Raft River geothermal field is a low temperature, single-phase (liquid) system located in southern Idaho near the boundary between the Snake River plain and the Basin and Range province (Figure 6.1). It is situated within a north-trending upper Cenozoic structural basin filled with nearly 1,600 m of tephra and sediments derived from the surrounding mountains.

North of the Raft River basin is the Great Rift system exhibiting open fractures in young basalt flows that extend northward 50 km to Craters of the Moon National Monument. The basin is flanked to the west and south by the Albion and Raft River mountains which expose gneiss-dome complexes of Precambrian adamellite mantled by Precambrian and lower Palezoic metasedimentary rocks (Felix, 1956; Armstrong, 1968; Compton, 1972). Drill hole data have demonstrated that a Precambrian and lower Paleozoic metasedimentary complex directly underlies the Cenozoic fill of the Raft River basin (Dolenc, et al., 1981). The two principal faults exposed within the valley are two north-trending normal fault zones along the west side of the valley called the Bridge and Horsewell fault zones. There is also some geologic and geophysical evidence (Mabey, et al., 1978) suggesting a possible basement shear, called the Narrows Structure, that trends northeast across the valley. It has been noted (Covington, 1980) that the abundance of faults and fractures increases with depth. In the upper part of the basin fill the faults dip steeply (60°-80°) and with increasing depth, fault dip decreases until they become nearly parallel with the contact between the fill and the Precambrian basement. Movement along these normal faults produce abundant, and near-vertical, open fractures near the base of the basin fill (Covington, 1980; Guth, et al.,

1981). A structure cross-section along line of section B-B' in Figure 6.1 is shown in Figure 6.2.

In 1971, the United States Geological Survey declared the Raft River valley a Known Geothermal Resource Area (KGRA). Since 1974, seven deep wells, ranging from 1176 m to 1994 m, have been drilled (Figure 6.3). Four production wells, RRGE-1,2,4, and 5 were drilled near the intersection of the Bridge Fault and the Narrows Structure. Another production well, RRGE-3, was drilled away from the major fault zones to see if the resource extended into the valley. All of the production wells were drilled into the Precambrian basement. Two intermediate-depth wells, RRGI-6 and 7, were drilled further east for the purpose of reinjecting spent geothermal fluid. These wells are completed in the Salt Lake formation, a tuffaceous sandstone, siltstone, conglomerate sequence. Figure 6.4 shows the distribution of depths and the formations penetrated by the wells. No significant wellbore skin damage has been observed at the Raft River wells. From 1974 to 1982, extensive geological, geophysical and hydrological testing and analyses were carried out at Raft River under the auspices of the U.S. Department of Energy (Dolenc, et al., 1981). The Raft River reservoir was an ideal location to test the solid earth tide response methods because of the vast amount of conventional reservoir evalution work carried out during the past decade.

Conventional well pumping test data taken between 1975 and 1979 were used for the tidal response analysis. Pump test duration ranged from 6 to 37 days with pressure measurement sampling rates of every half hour or every hour. Wellhead data were obtained during the tests with Paroscientific pressure transducers. The raw data are shown in Figures 6.5-6.11. Downhole data were taken with a Hewlett-Packard temperature-compensated quartz pressure probe. The tidal fluctuations are clearly evident on these data. The pressure record

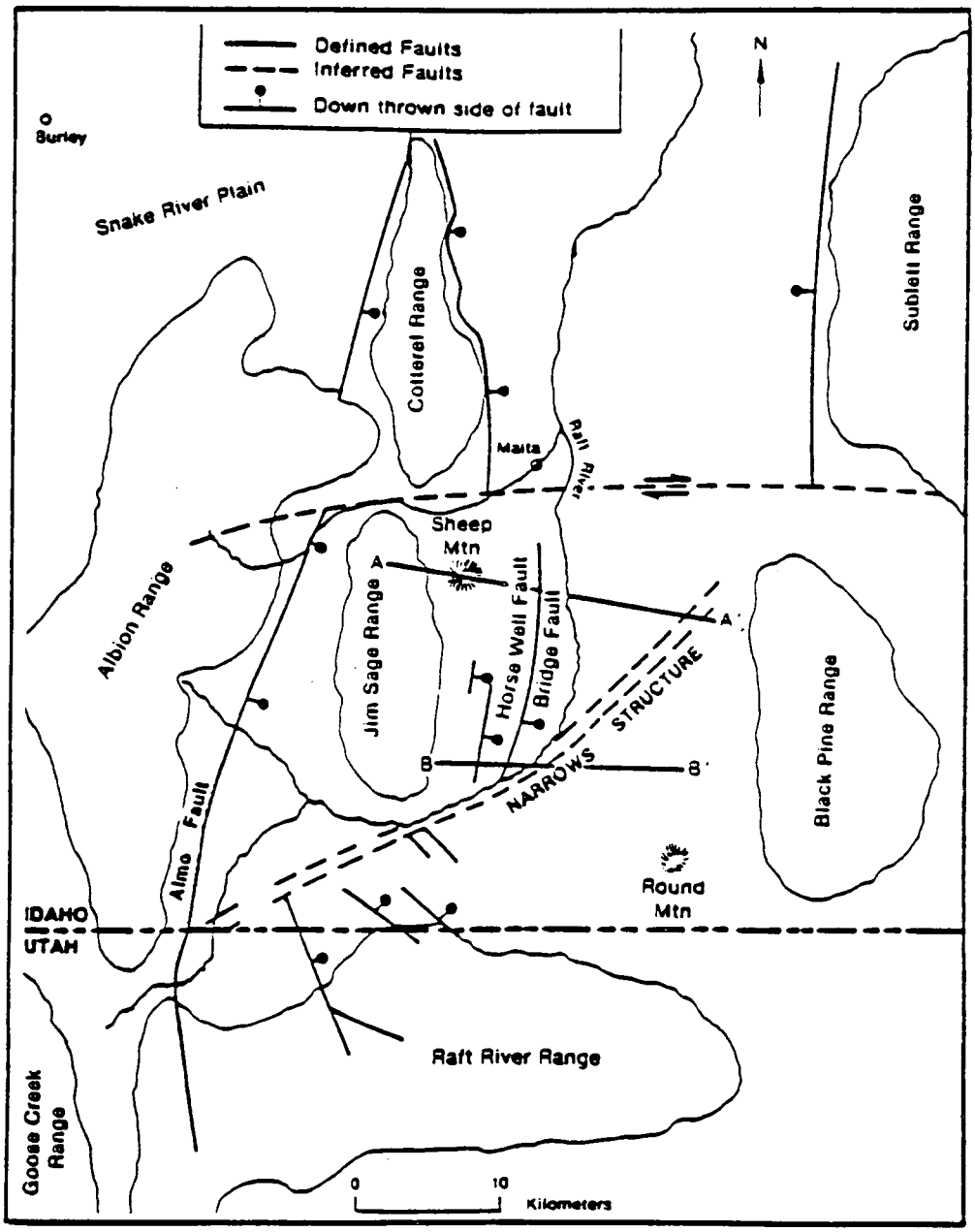

Figure 6.1. Raft River Valley and major structural features adjoining the valley (from Dolenc, et al., 1981).

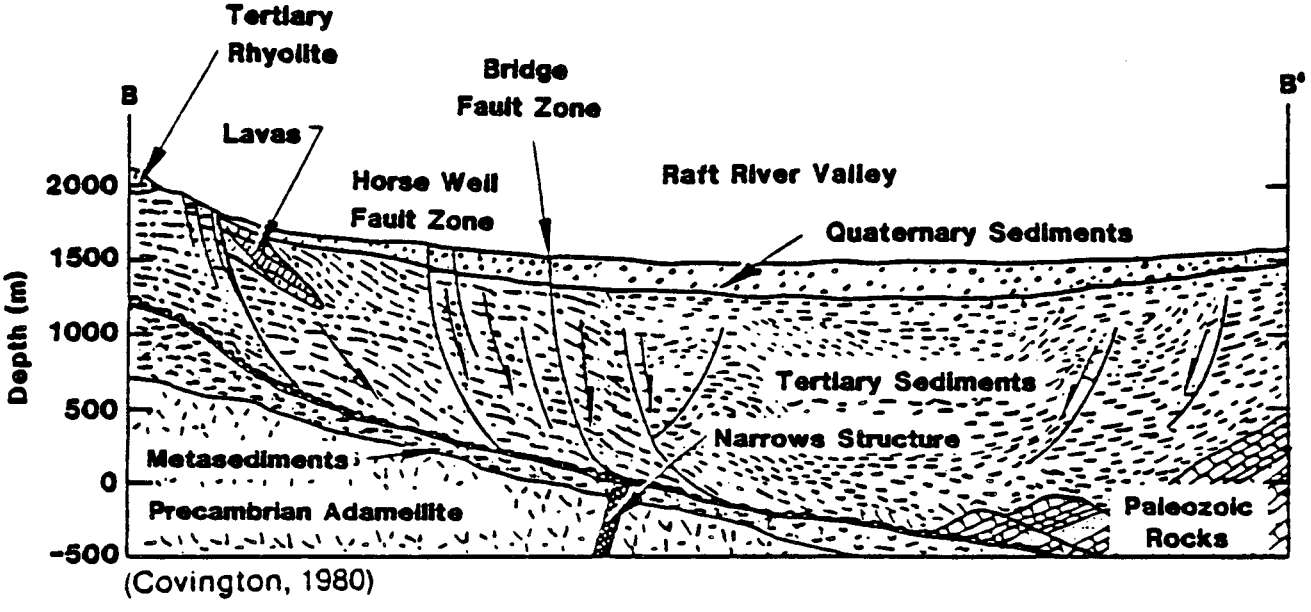

Figure 6.2. Cross-section B-B' of Figure 6.1 (from Covington, 1980).

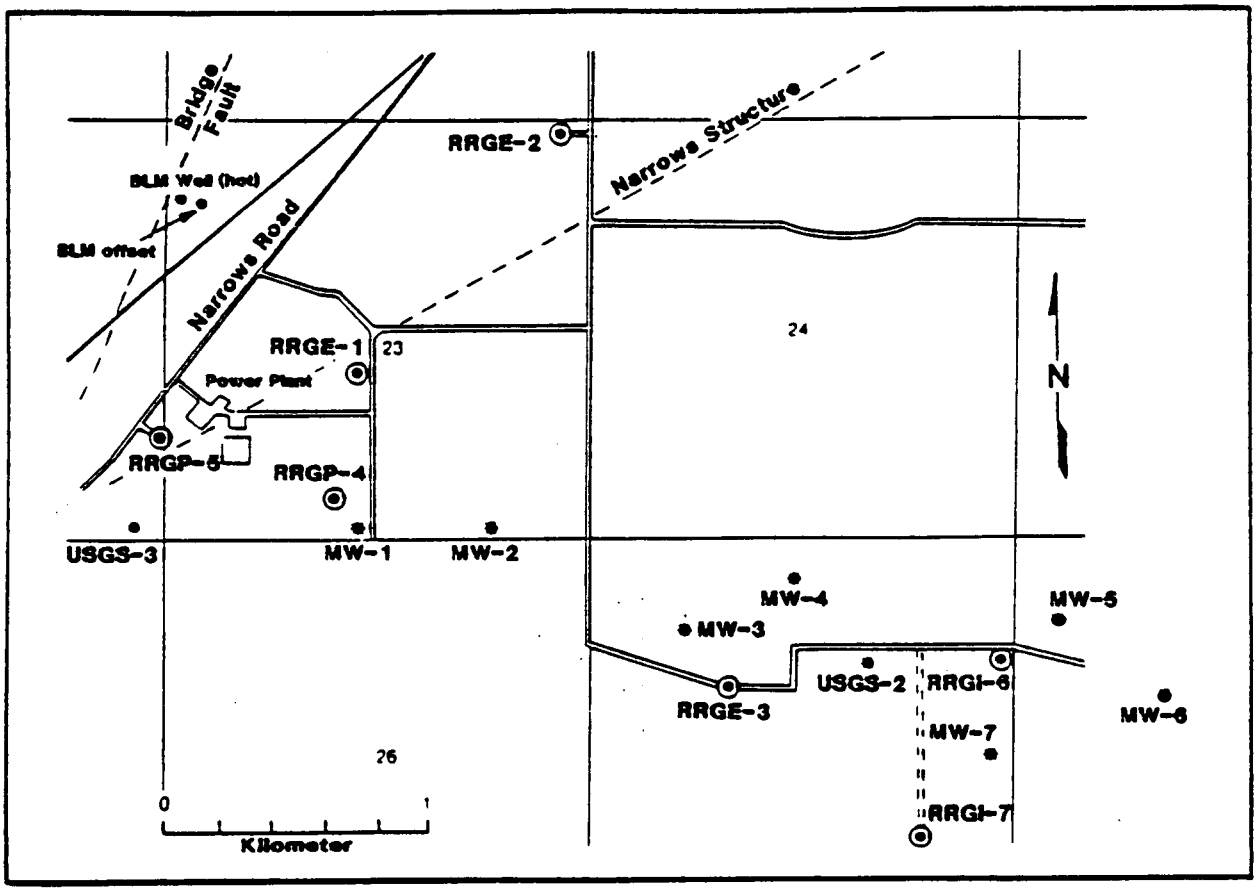

Figure 6.3. Geothermal well locations within the Raft River Geothermal Field.

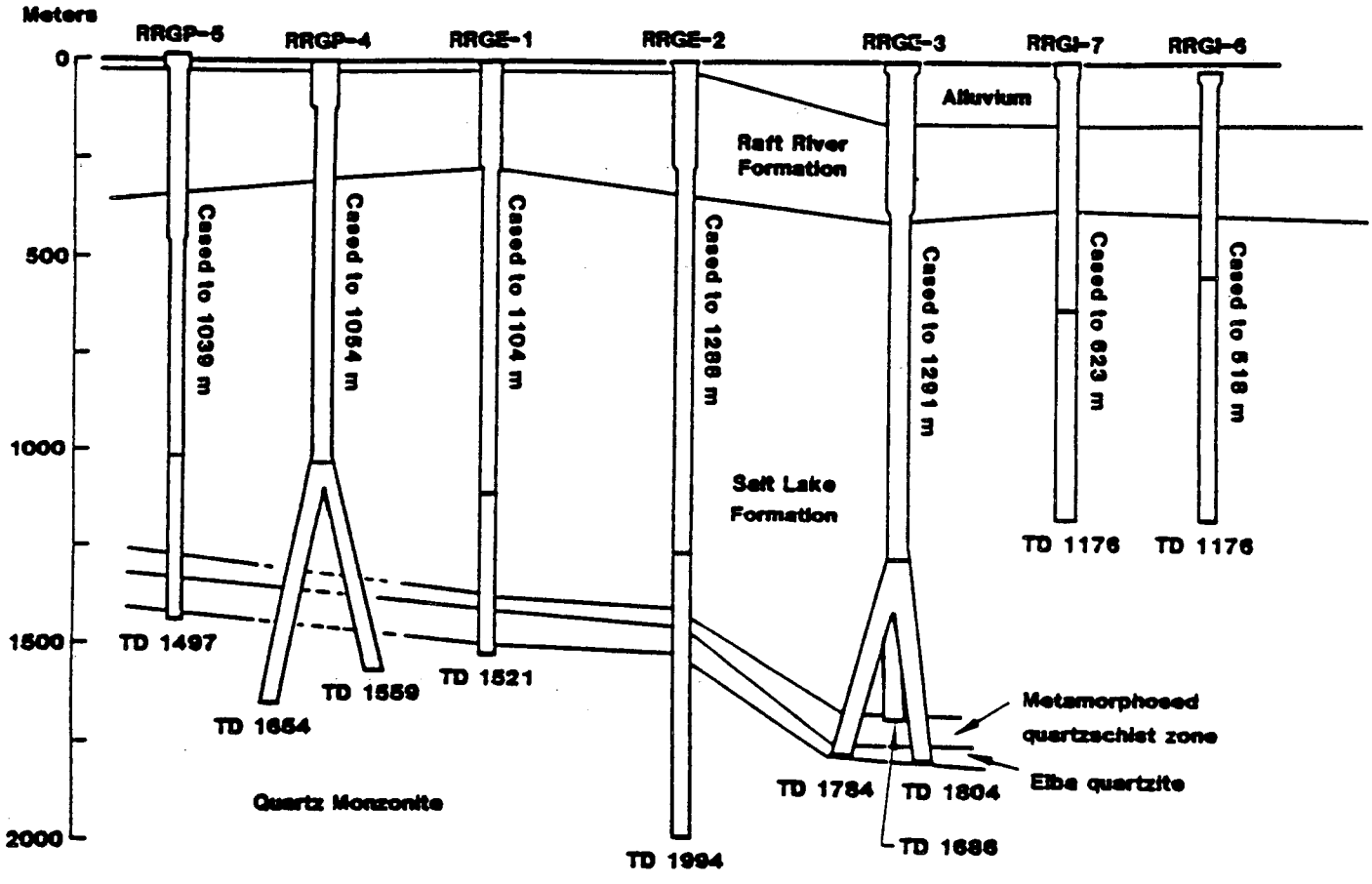

Figure 6.4. Raft River geothermal wells, showing casing depths (from Dolenc, et al., 1981).

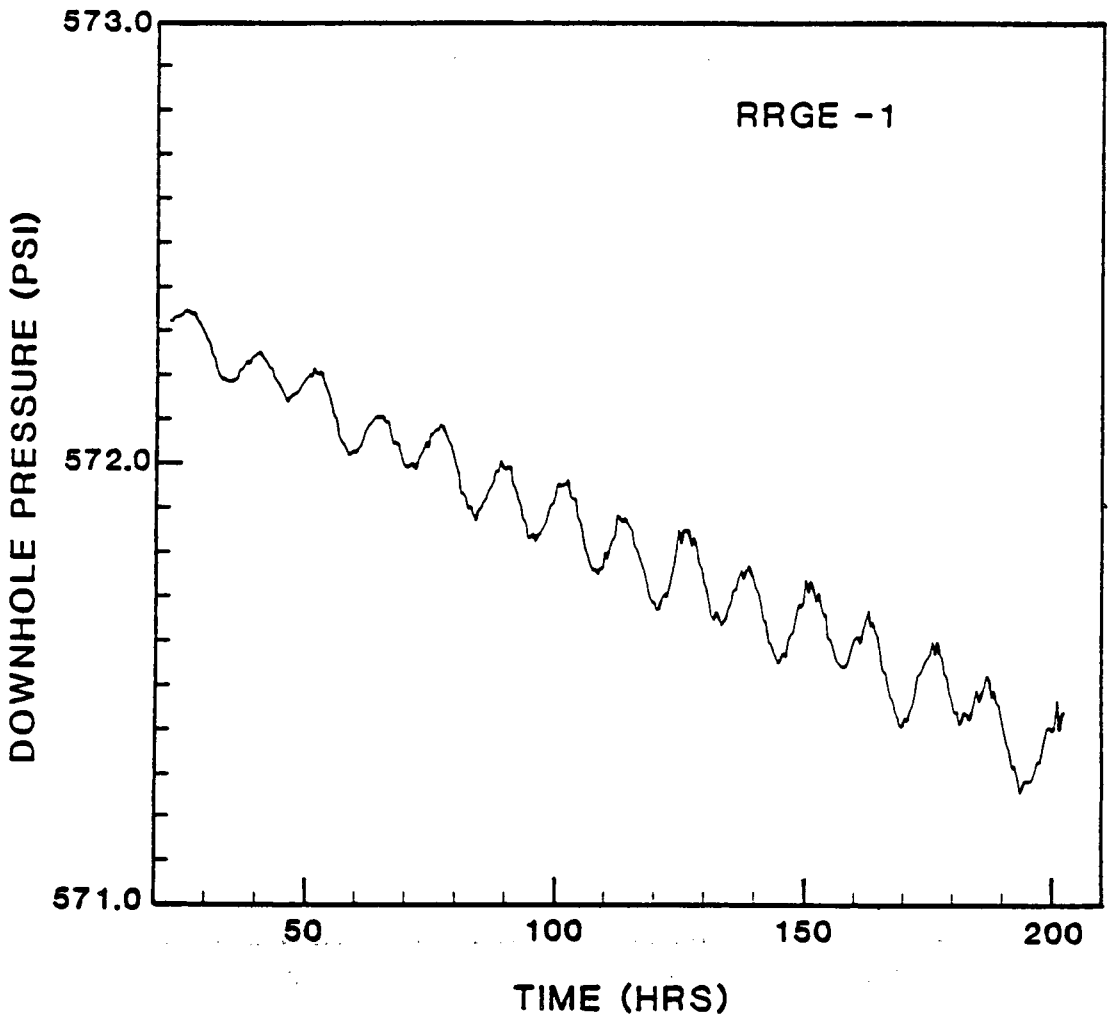

Figure 6.5. Raw downhole pressure data at RRGE-1.

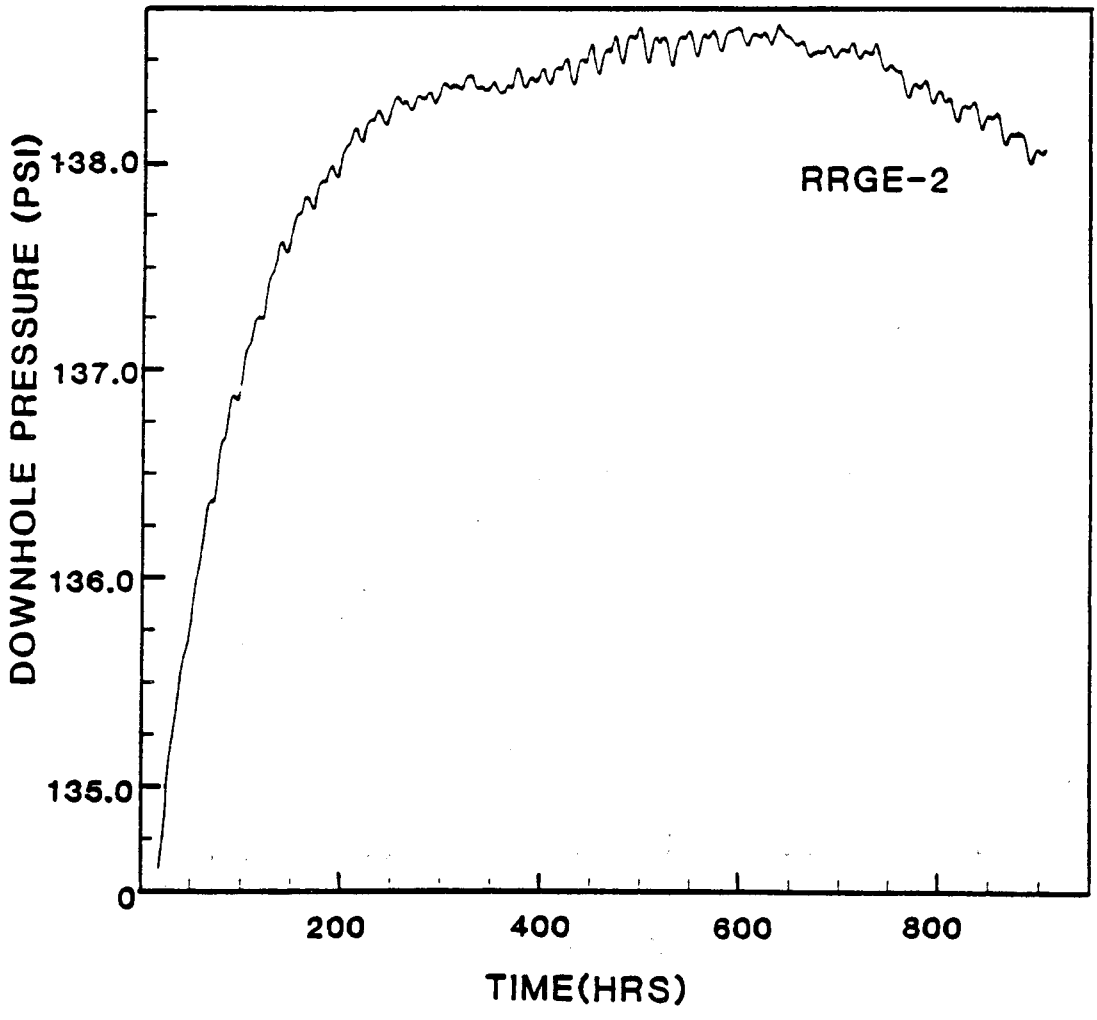

Figure 6.6. Raw downhole pressure data at RRGE-2.

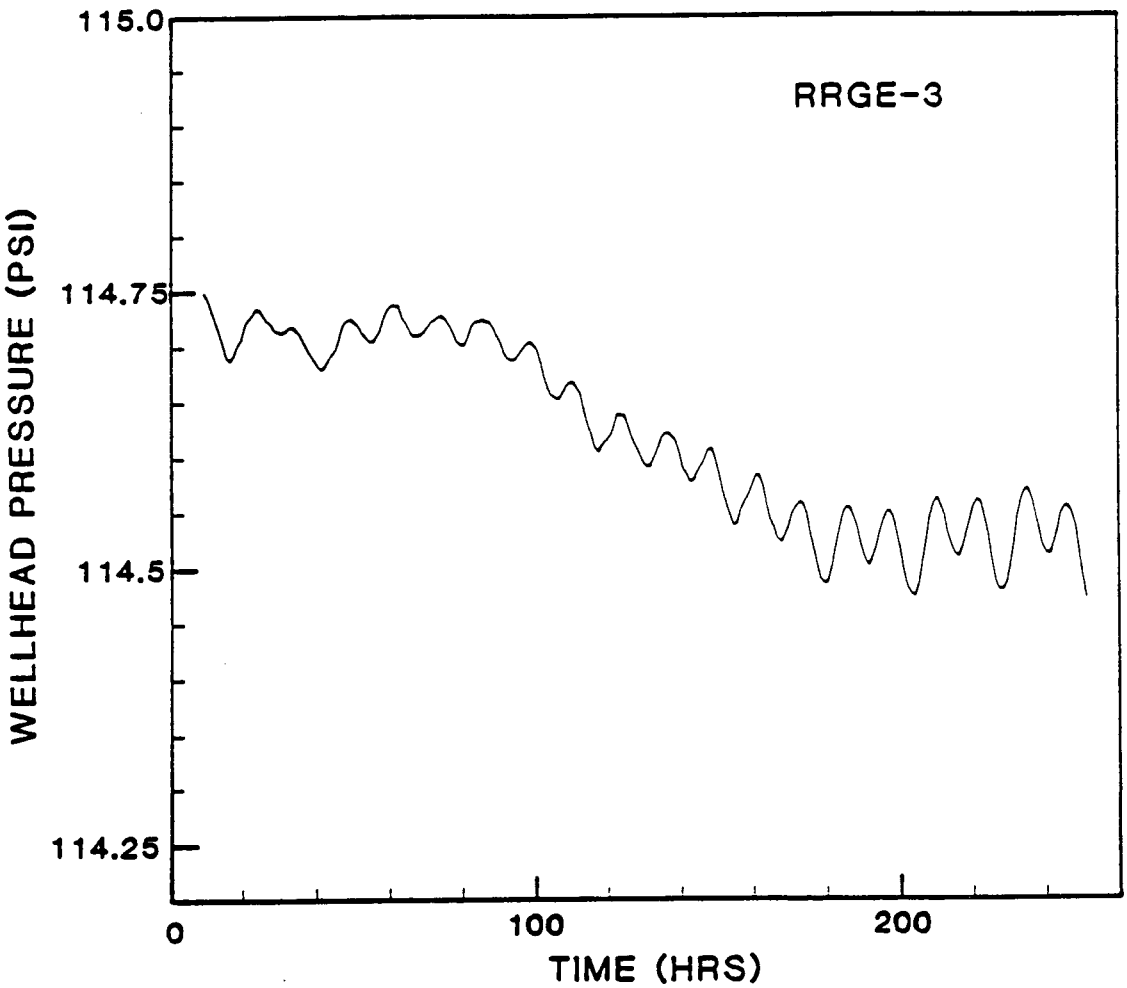

Figure 6.7. Raw wellhead pressure data at RRGE-3.

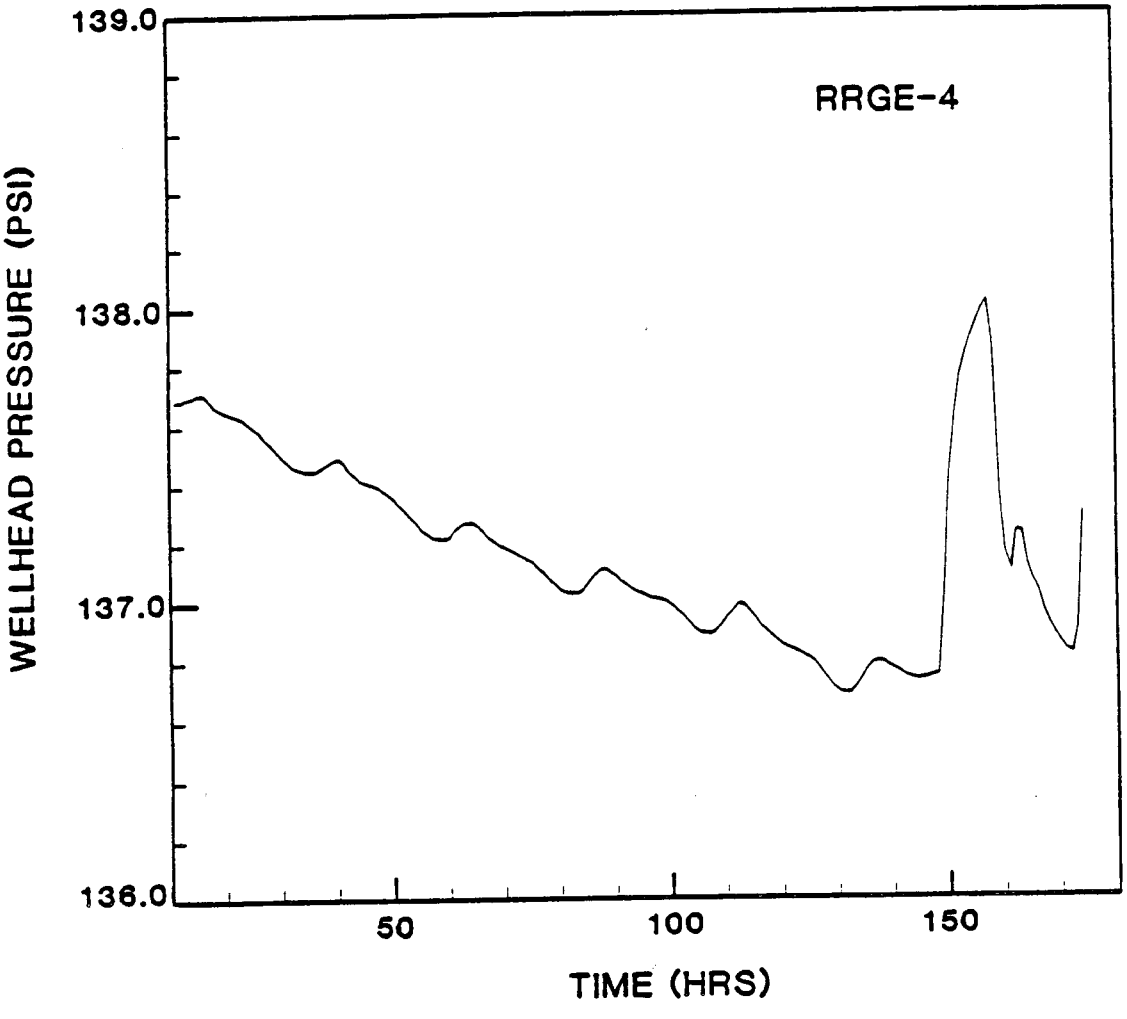

Figure 6.8. Raw wellhead pressure data at RRGE-4 showing pulse test.

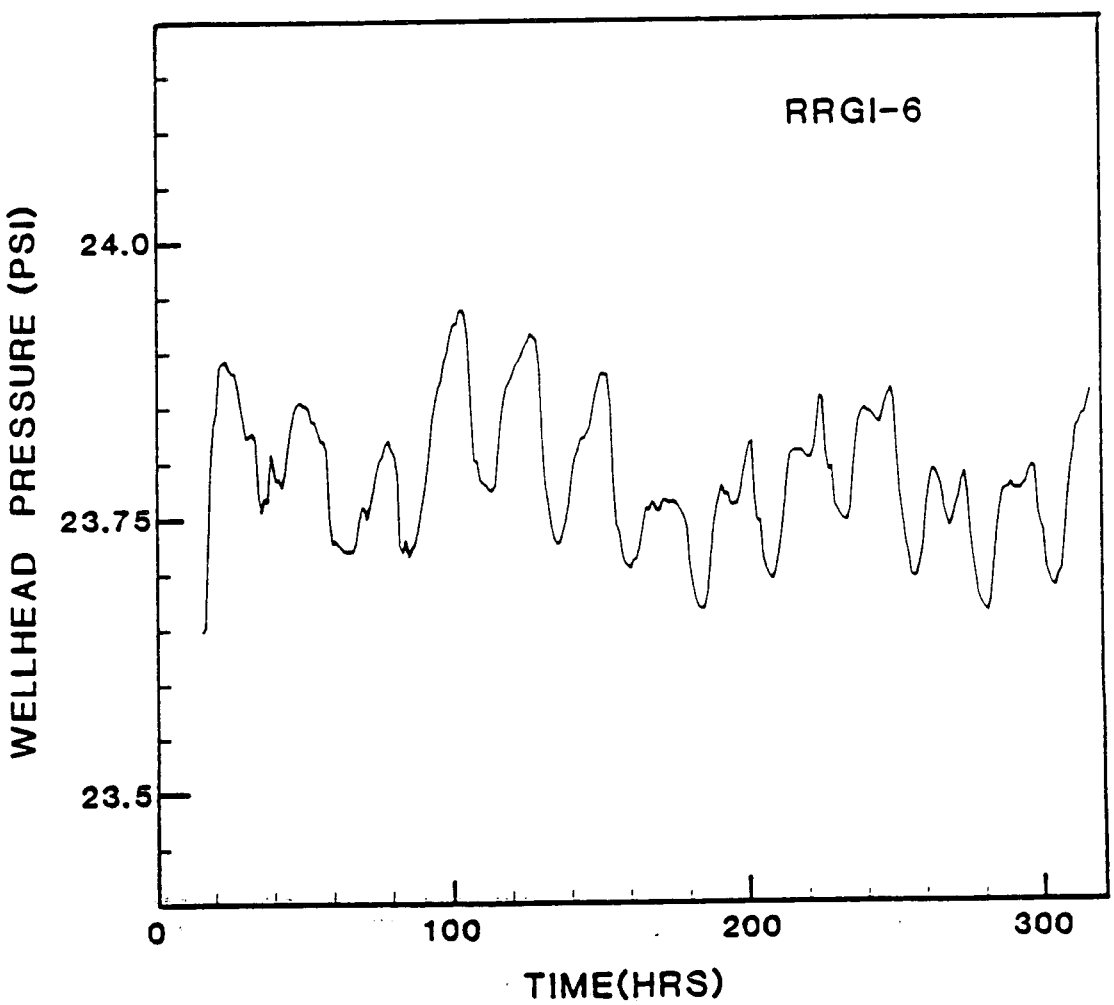

Figure 6.9. Raw wellhead pressure data at RRGI-6.

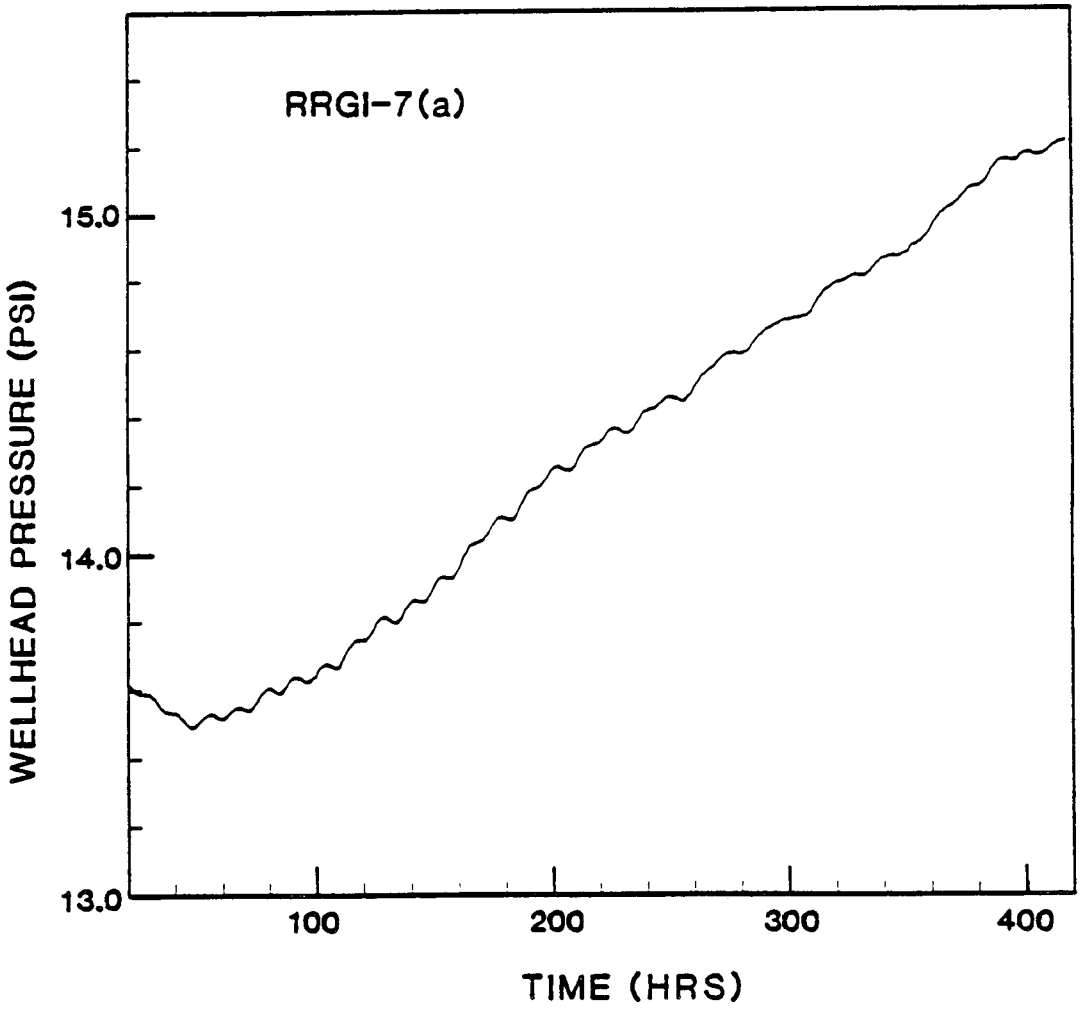

Figure 6.10. Raw wellhead pressure data at RRGI-7.

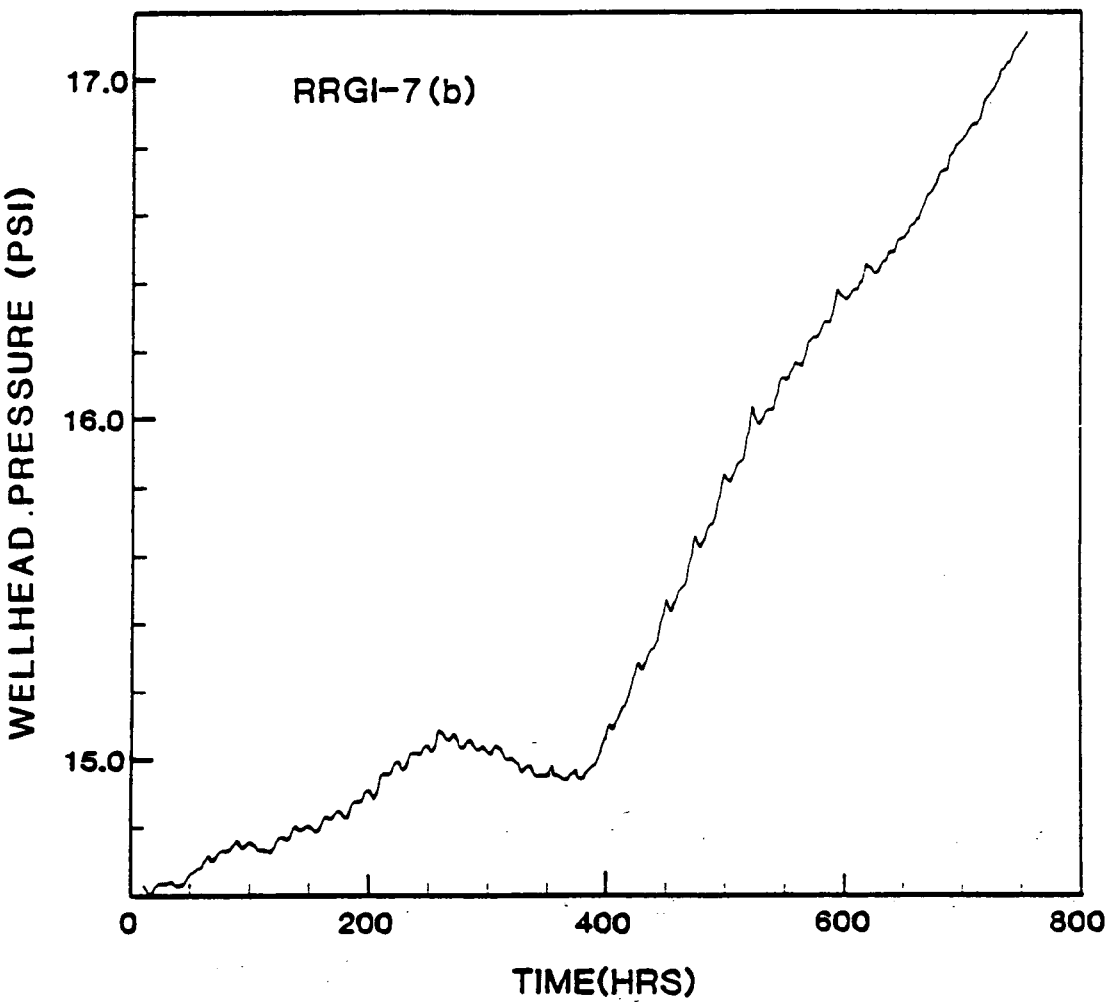

Figure 6.11. Raw wellhead pressure data at RRGI-7.

represents the sum of pumping, barometric loading, and tidal strain effects. In order to isolate the tidal response for further analysis, pumping and barometric effects were removed. This was accomplished by first removing from the measured pressure all signals at tidal frequencies using a combination of least-squares methods and detrending techniques (see Chapter V). Figure 6.12 shows the barometric efficiencies computed in this manner for the wells at Raft River for which data were available. What is remarkable about these results is the large variation in barometric efficiency within the reservoir. These variations are due primarily to the nature of the fluid conduits - i.e., fracture or pore. Figures 6.13-6.19 show the barometric pressure r(t) recorded at Pocatello, Idaho, over the same time periods that fluid pressure was recorded at the wells. Also shown (crosses) is the value of $[q(t) - S_N(t)]/BE$. Having obtained the barometric efficiency and a best estimate for the pumping effects, the barometric and pumping effects can be removed from the measured pressure record to obtain the isolated response to solid earth tidal strain. Figure 6.20 shows the solid earth tide pressure response at RRGE-2 removed from the interference test shown in Figure 6.6 using the above methodology. Tidal gravity is also shown in the figure. The resulting pressure signal, along with the theoretical tidal strain tensor components, are Fourier transformed to obtain amplitude and phase information for the various tidal constituents (see Chapter V). Figures 6.21-6.27 show the Fourier amplitude spectra, as determined from equation (V.2), for the tidal pressure response for the wells. The tidal constituents are clearly seen in these spectra. Line spectral analysis was applied to the tidal pressure data and the theoretical gravity and strain data. Tidal admittance and phase shifts relating the theoretical volumetric strain and the pore pressure response were computed. Figures 6.28-6.39 show this information with 90% confidence levels indicated.

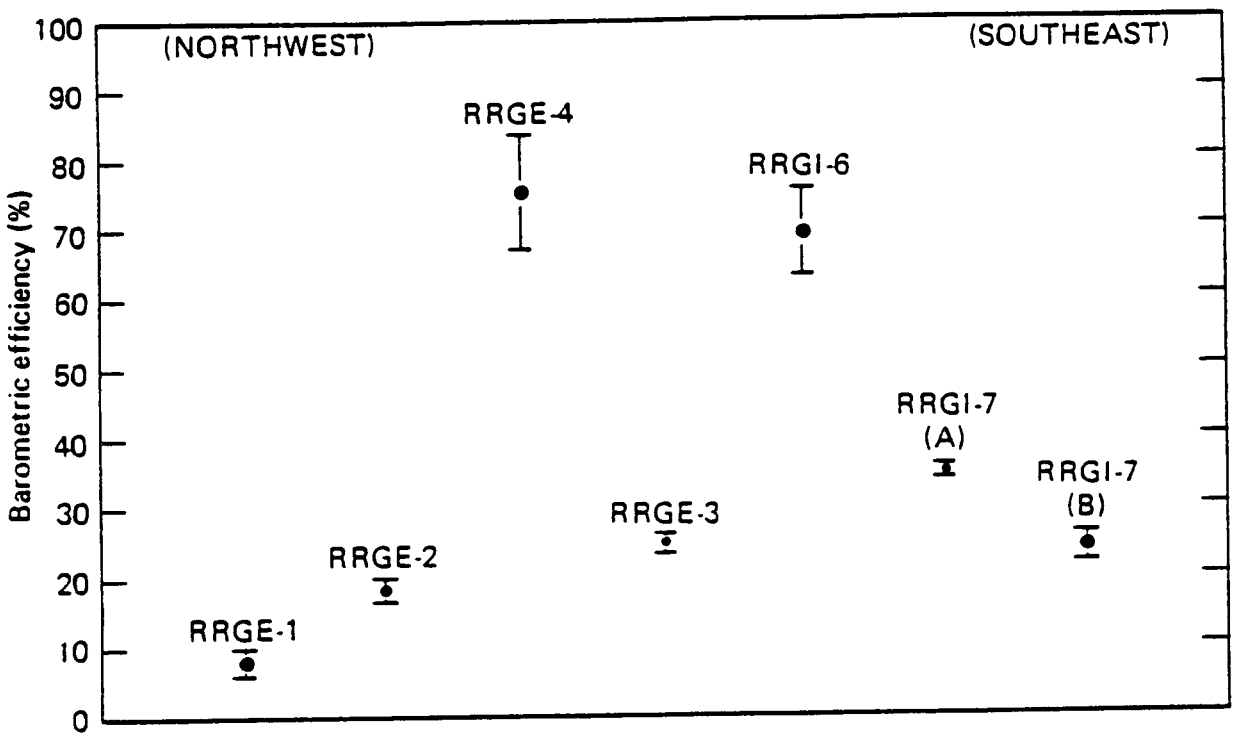

Figure 6.12. Computed barometric efficiencies for the Raft River Geothermal Field. Confidence intervals are at the 90% level.

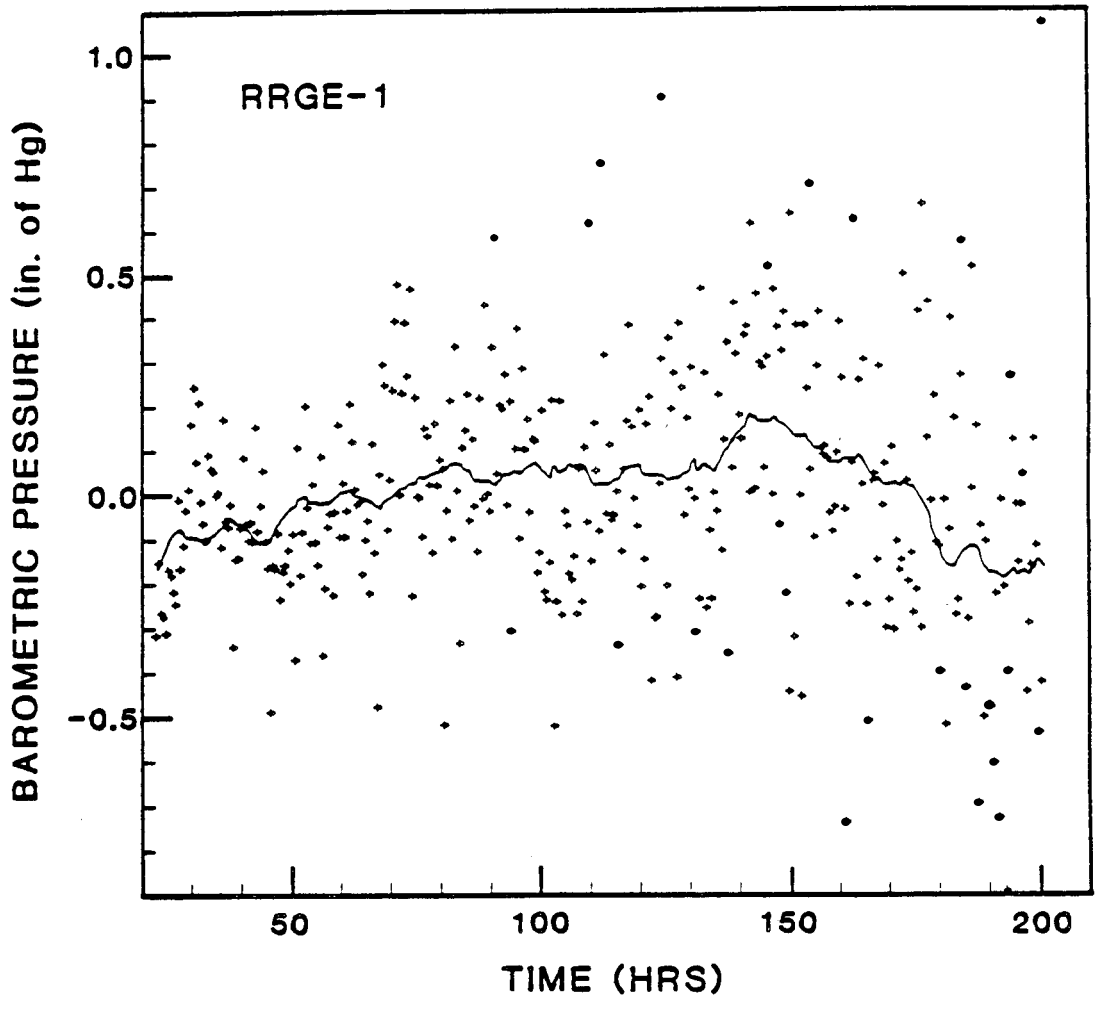

Figure 6.13. Barometric pressure recorded at Pocatello, Idaho (solid line) and measured pressure response to barometric loading divided by barometric efficiency (crosses). Both signals have tidal constituents removed.

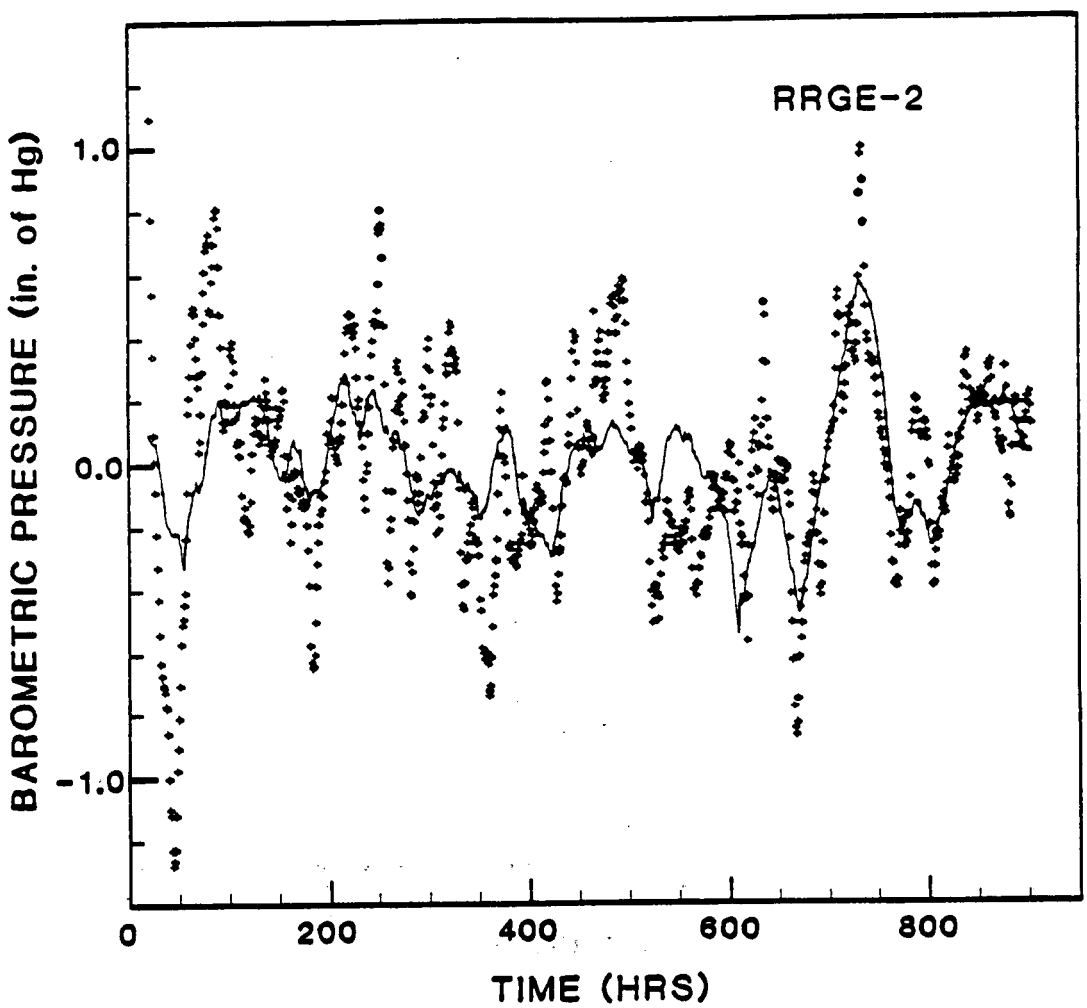

Figure 6.14. Barometric pressure recorded at Pocatello, Idaho (solid line) and measured pressure response to barometric loading divided by barometric efficiency (crosses). Both signals have tidal constituents removed.

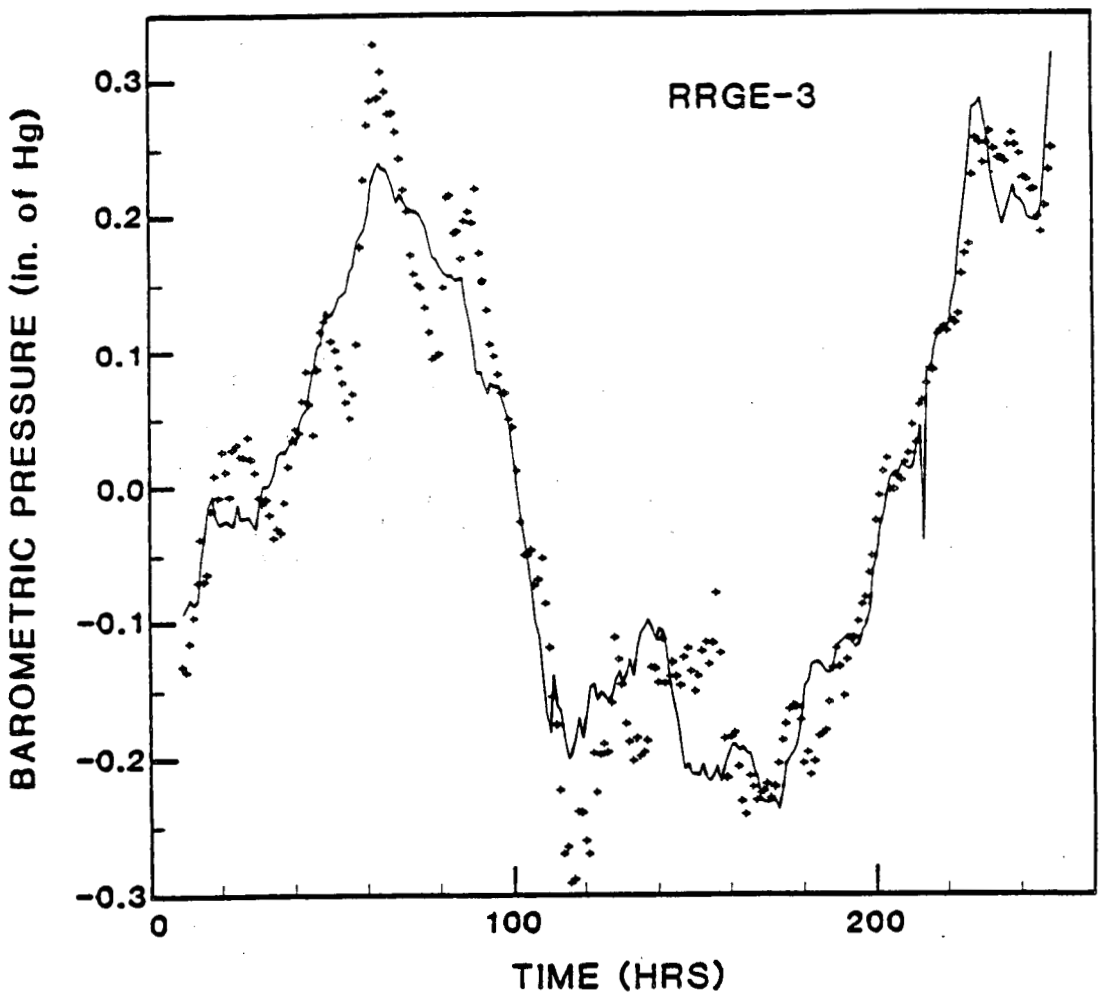

Figure 6.15. Barometric pressure recorded at Pocatello, Idaho (solid line) and measured pressure response to barometric loading divided by barometric efficiency (crosses). Both signals have tidal constituents removed.

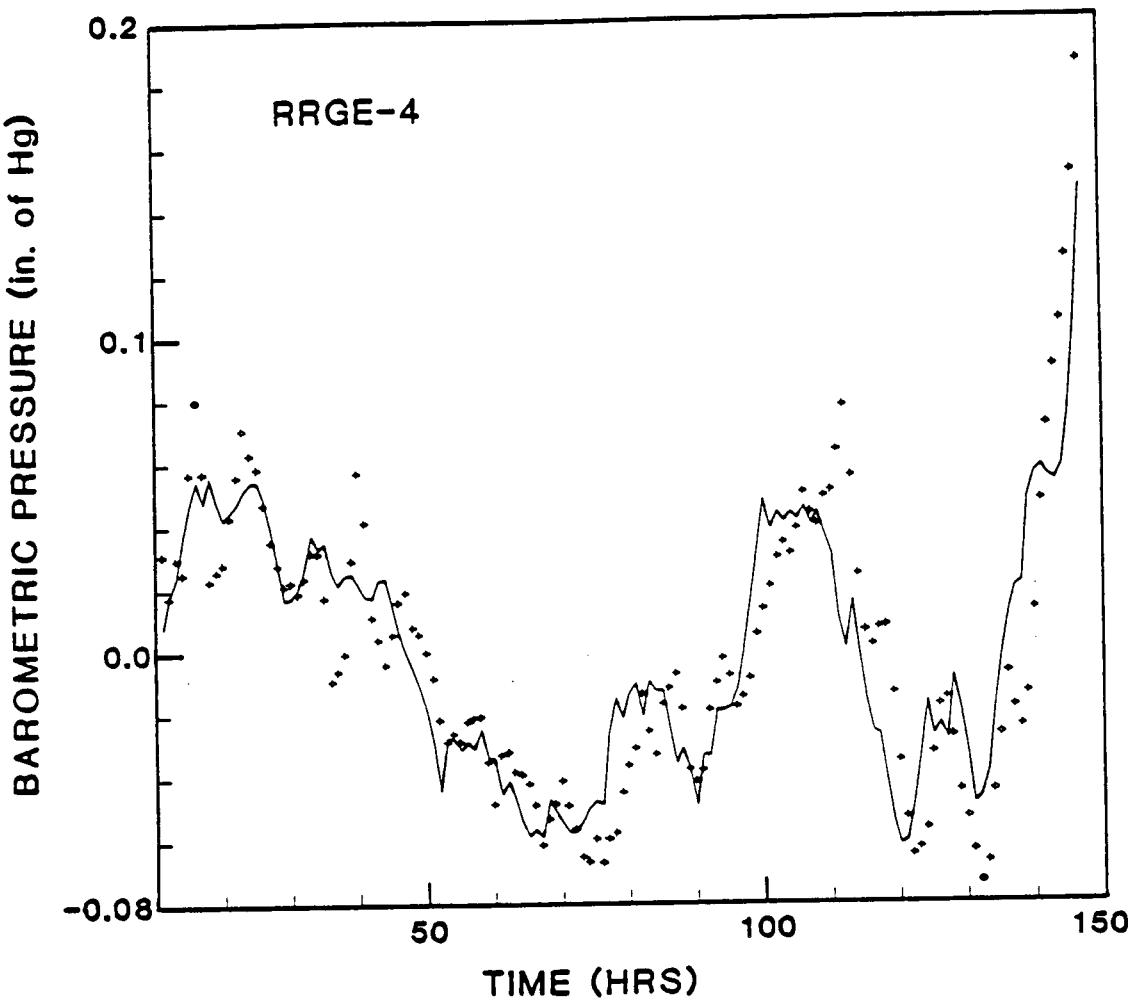

Figure 6.16. Barometric pressure recorded at Pocatello, Idaho (solid line) and measured pressure response to barometric loading divided by barometric efficiency (crosses). Both signals have tidal constituents removed.

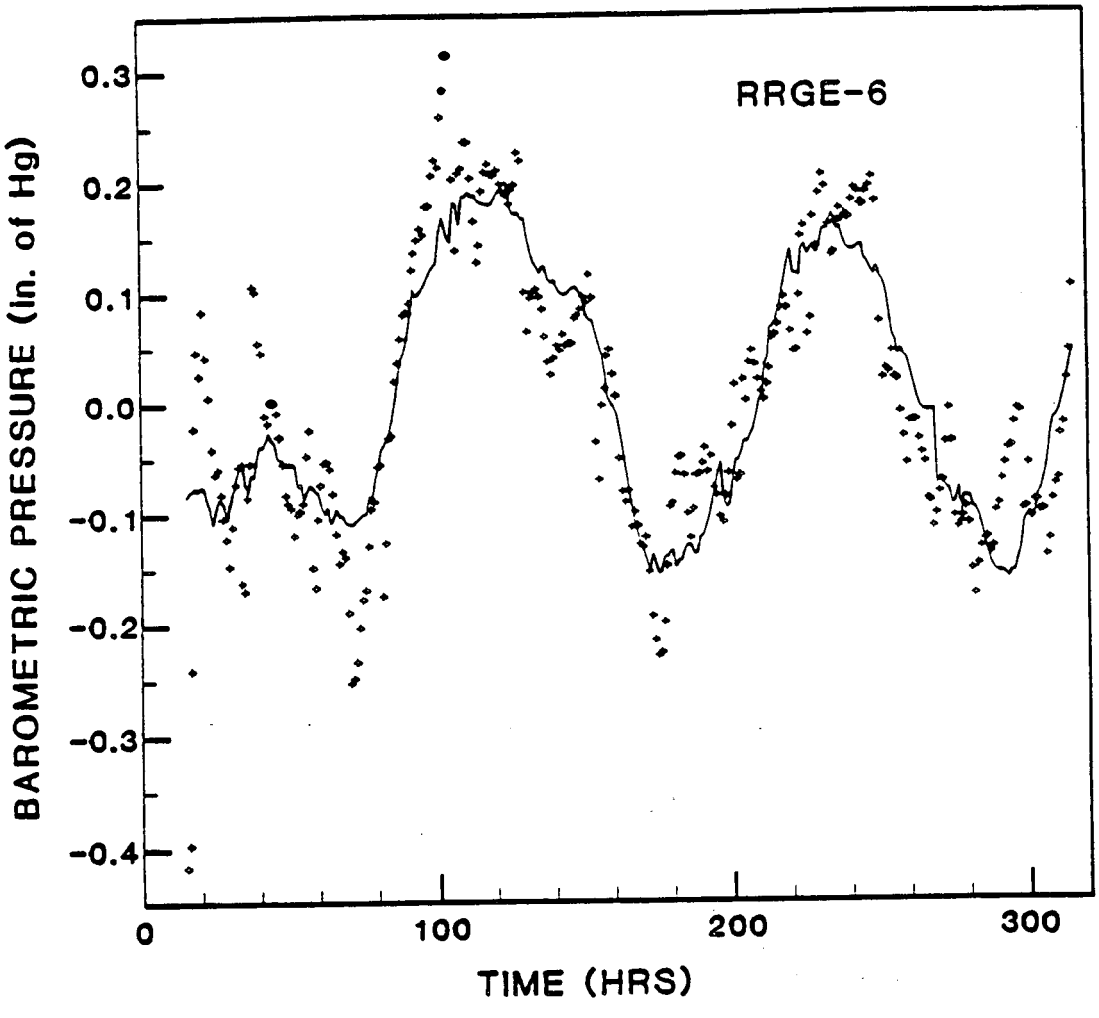

Figure 6.17. Barometric pressure recorded at Pocatello, Idaho (solid line) and measured pressure response to barometric loading divided by barometric efficiency (crosses). Both signals have tidal constituents removed.

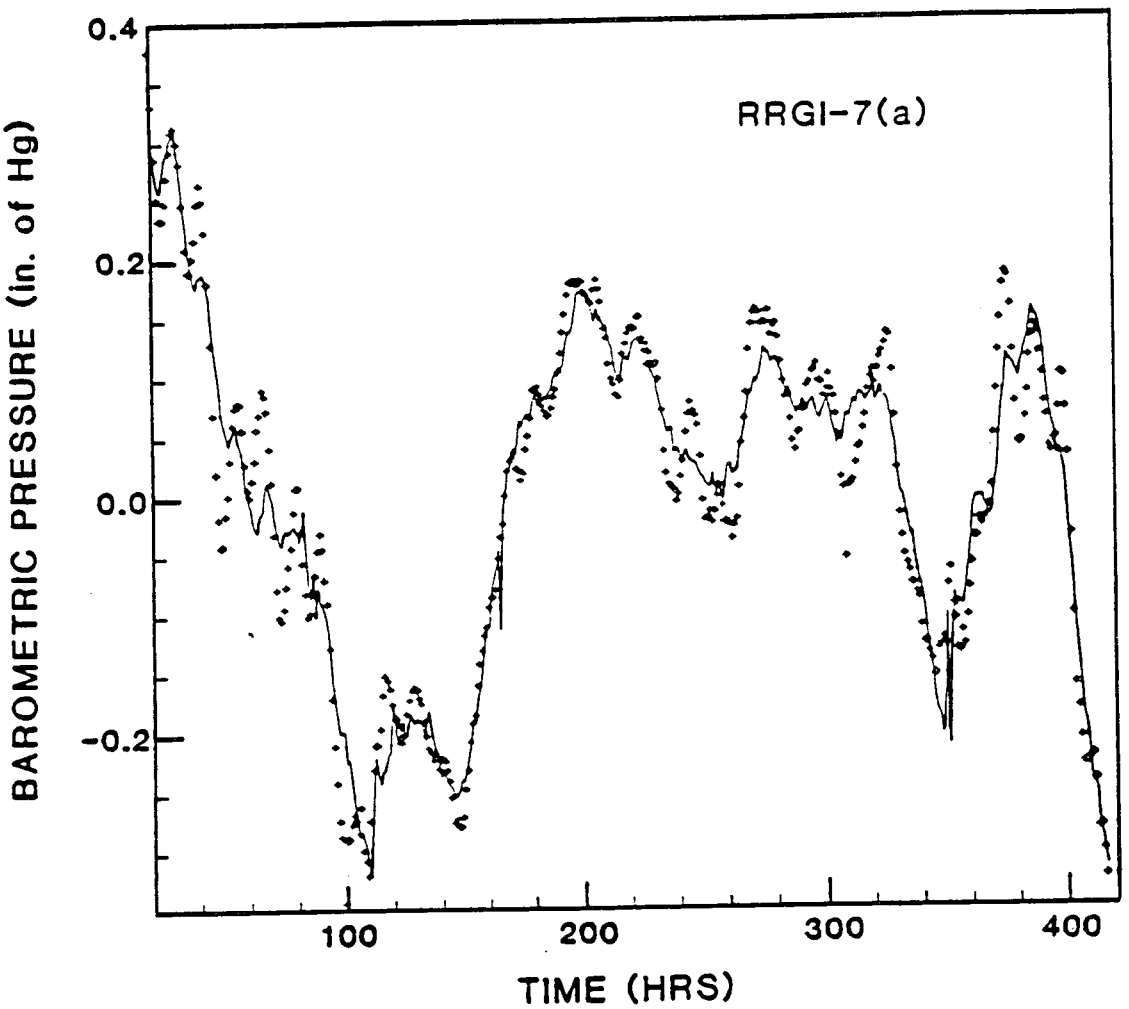

Figure 6.18. Barometric pressure recorded at Pocatello, Idaho (solid line) and measured pressure response to barometric loading divided by barometric efficiency (crosses). Both signals have tidal constituents removed.

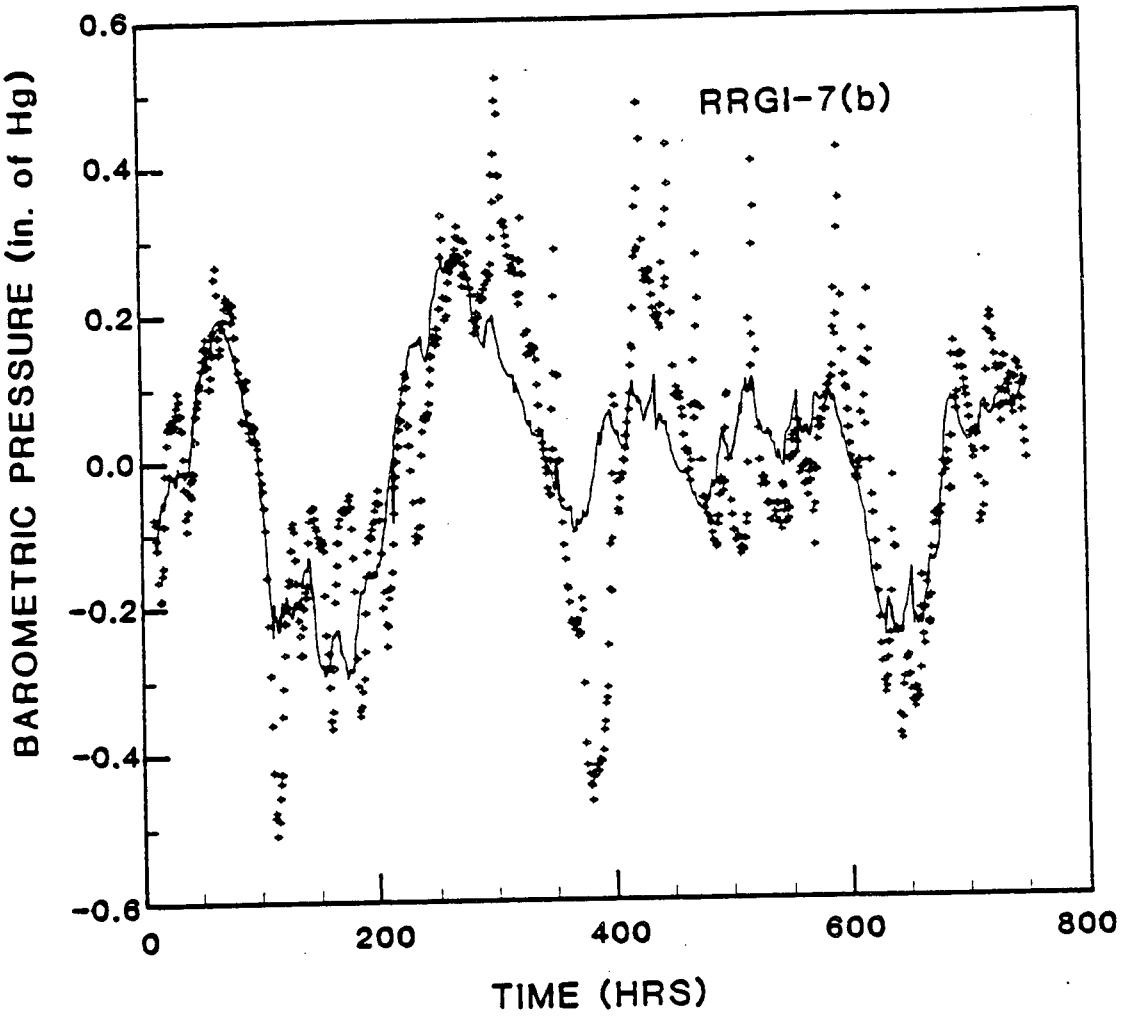

Figure 6.19. Barometric pressure recorded at Pocatello, Idaho (solid line) and measured pressure response to barometric loading divided by barometric efficiency (crosses). Both signals have tidal constituents removed.

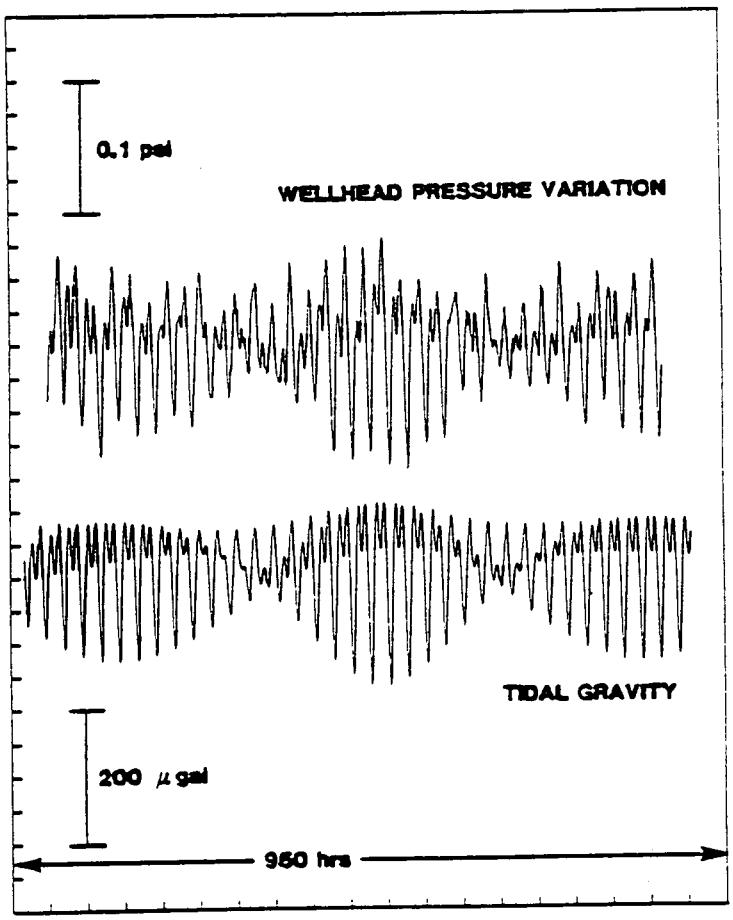

Figure 6.20. Isolated wellhead pressure response to tidal strain at RRGE-2, showing theoretical tidal gravity over same time period.

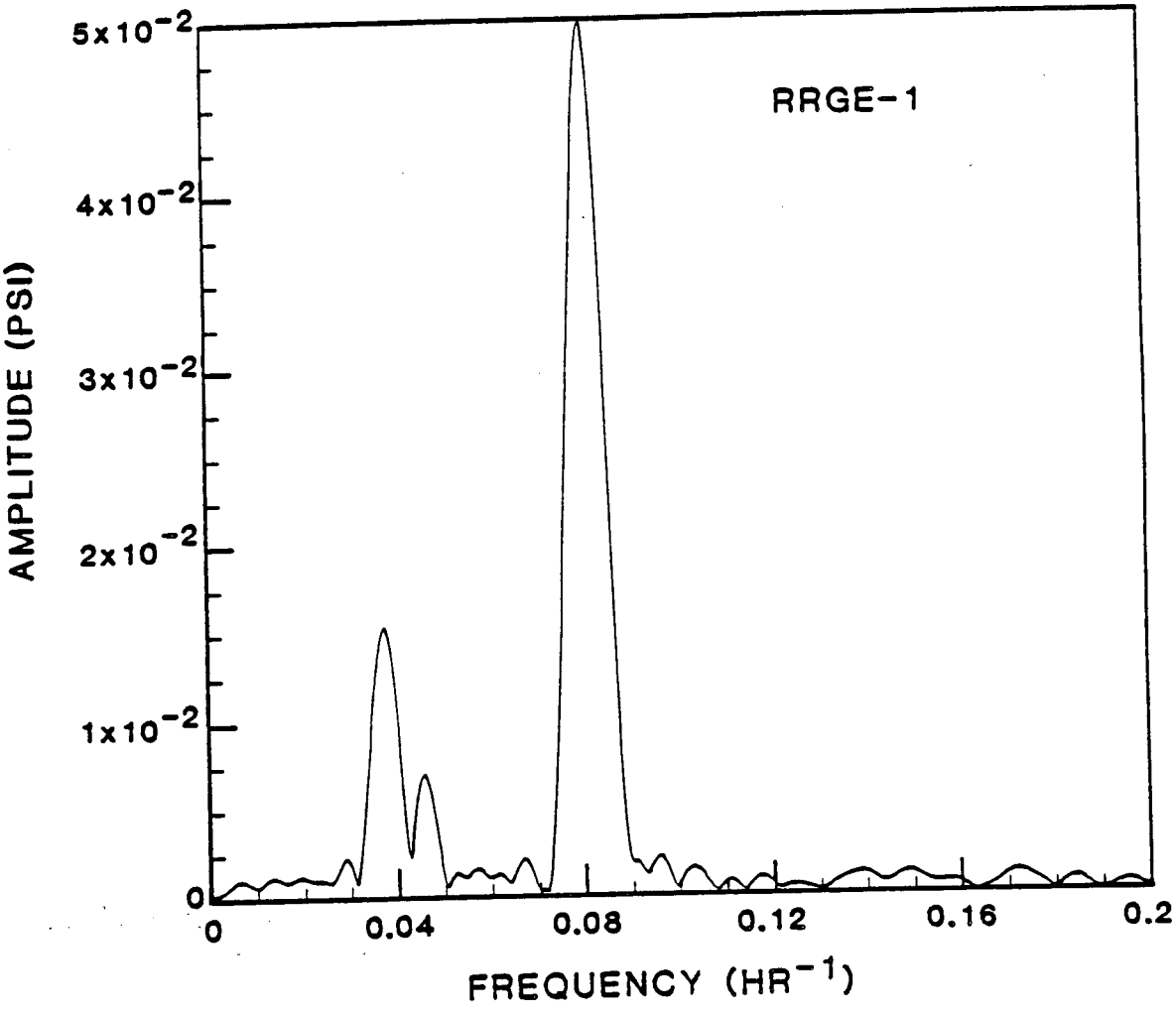

Figure 6.21. Fourier amplitude spectrum based on Finite Fourier transform.

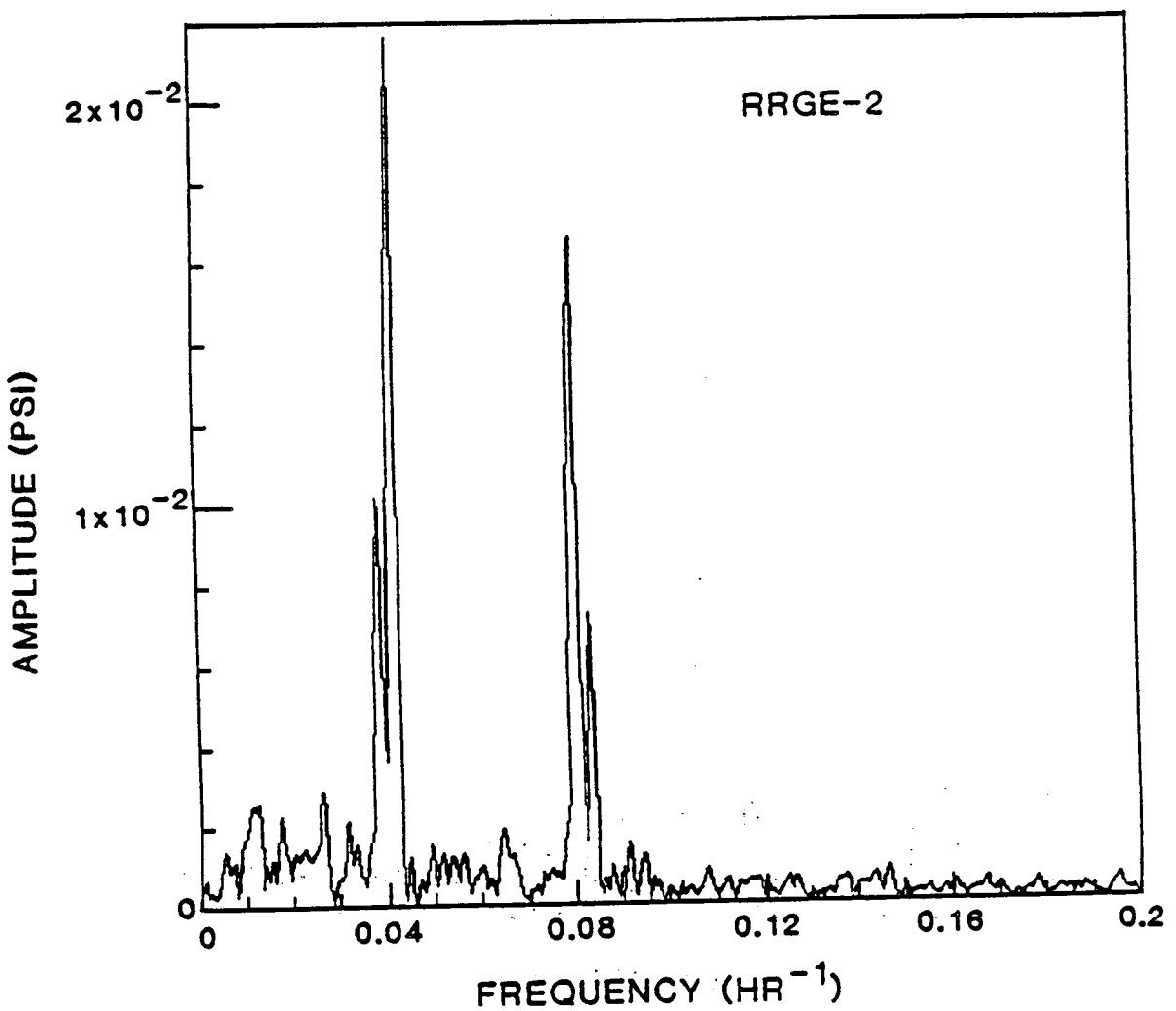

Figure 6.22. Fourier amplitude spectrum based on Finite Fourier transform.

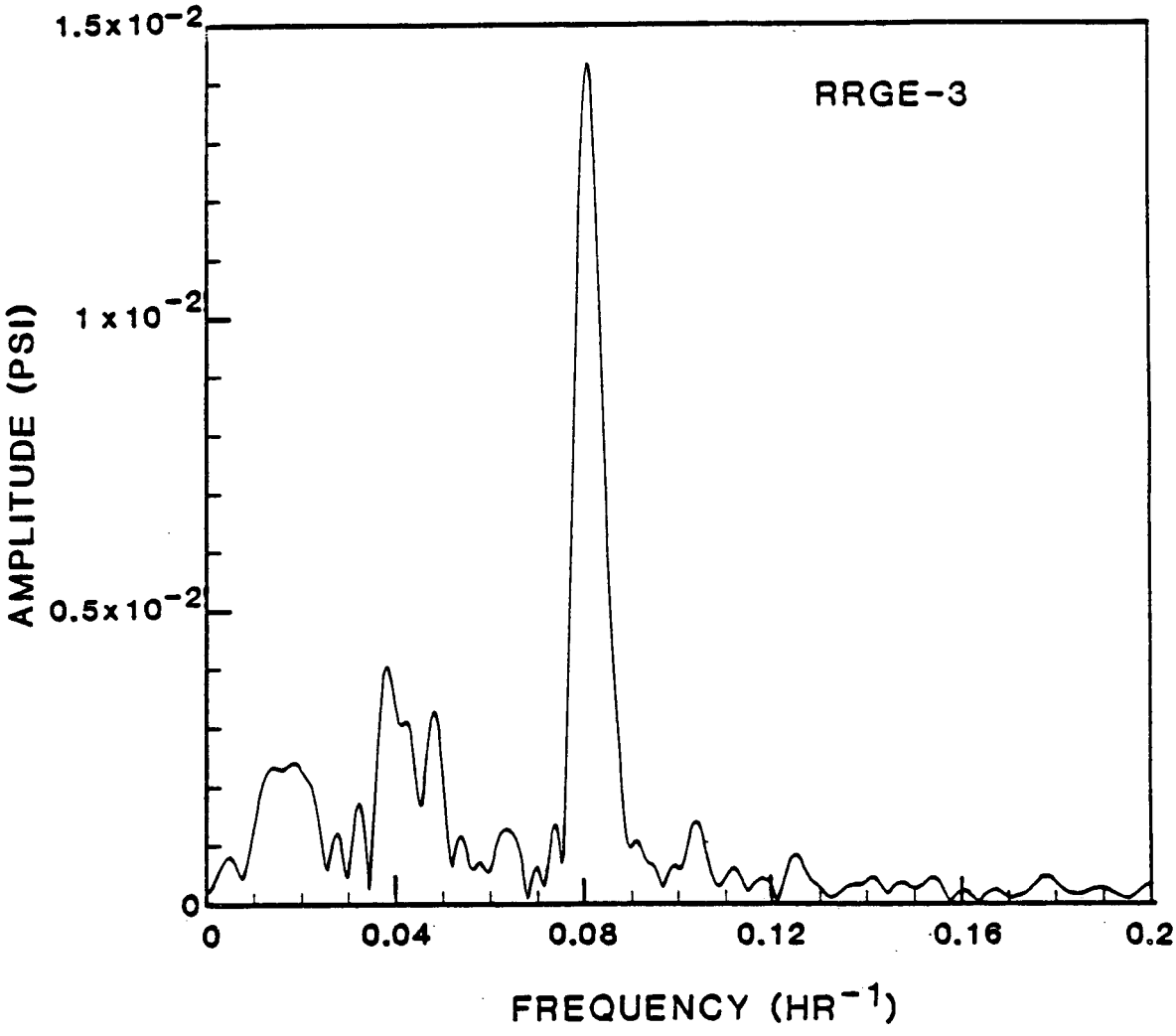

Figure 6.23. Fourier amplitude spectrum based on Finite Fourier transform.

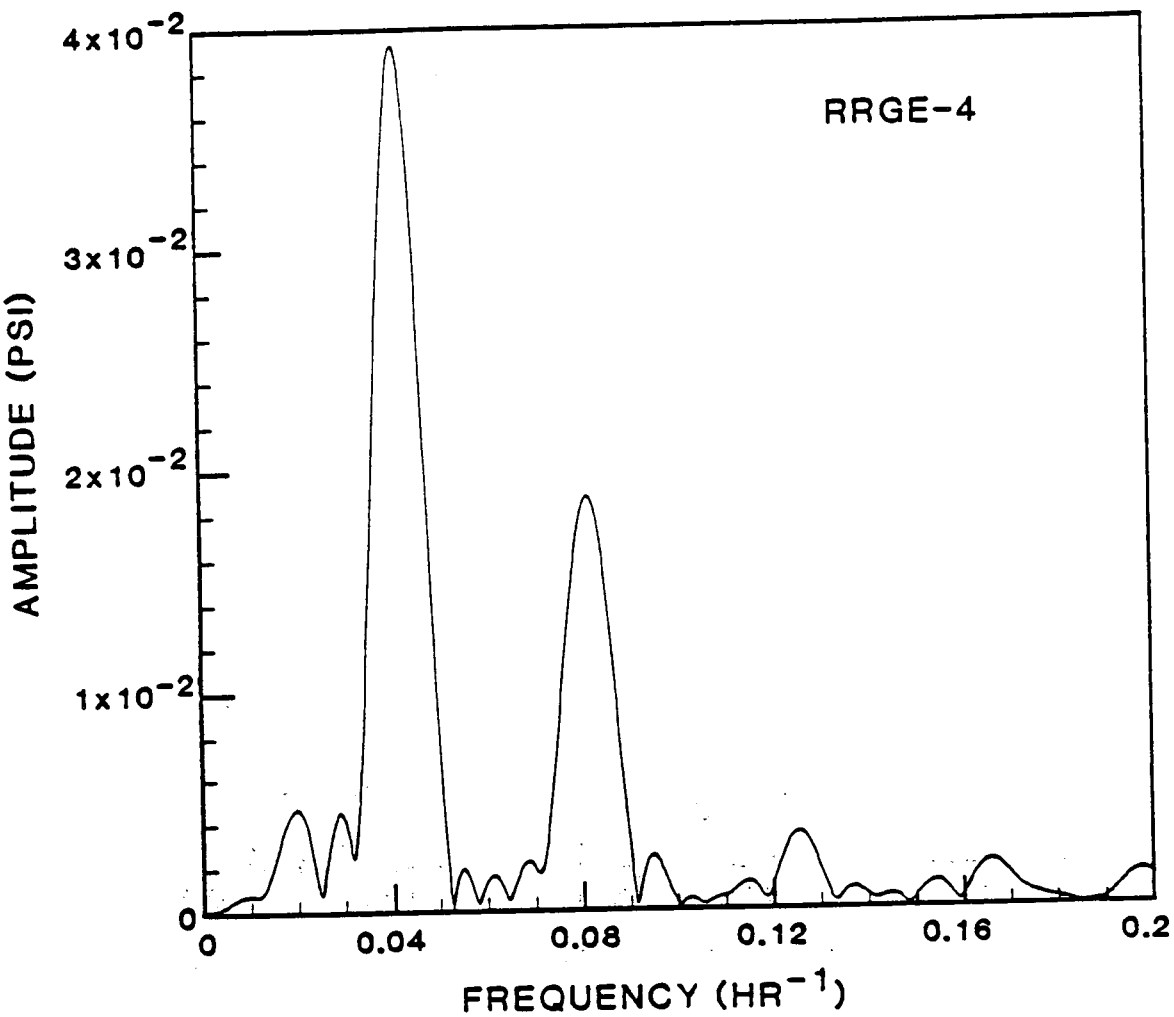

Figure 6.24. Fourier amplitude spectrum based on Finite Fourier transform.

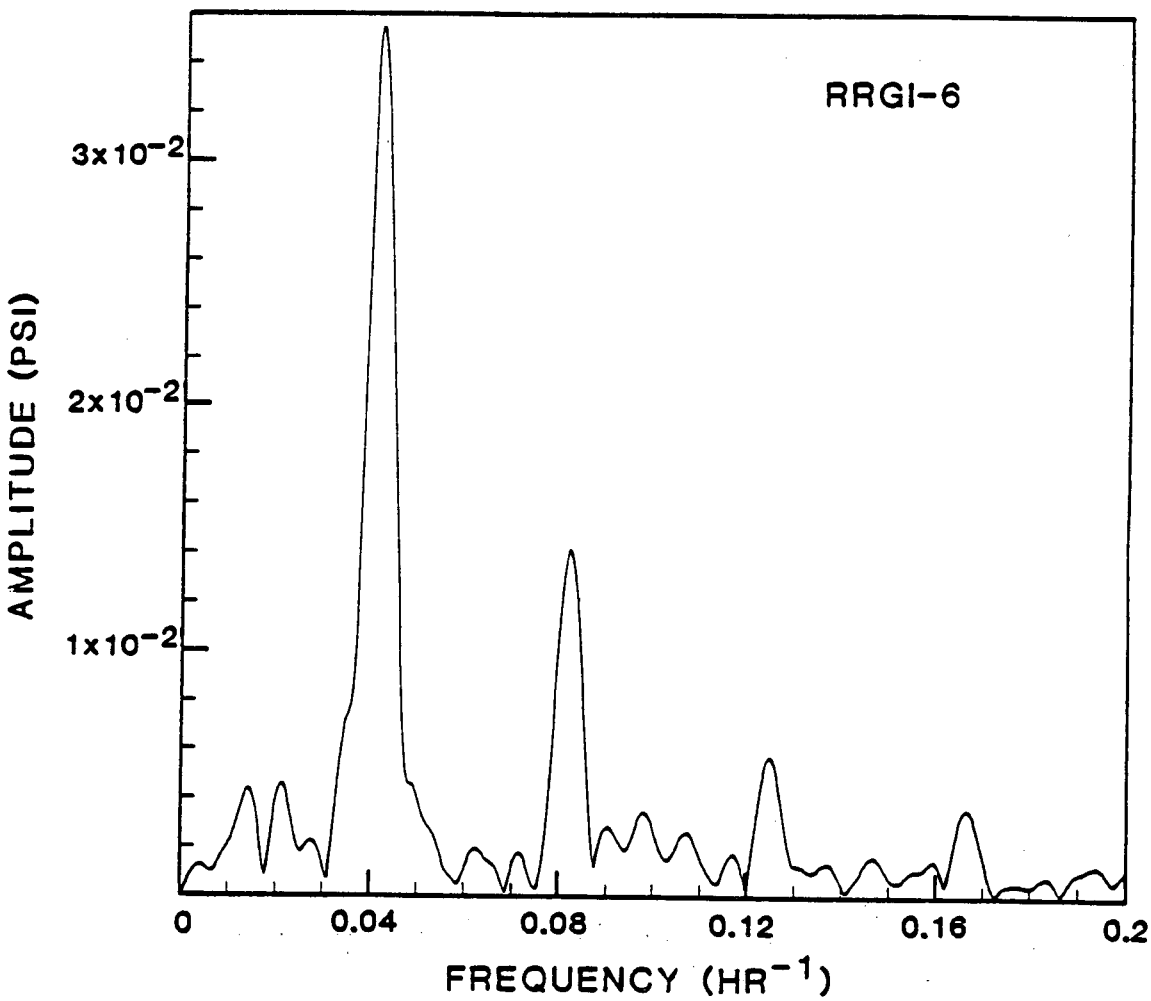

Figure 6.25. Fourier amplitude spectrum based on Finite Fourier transform.

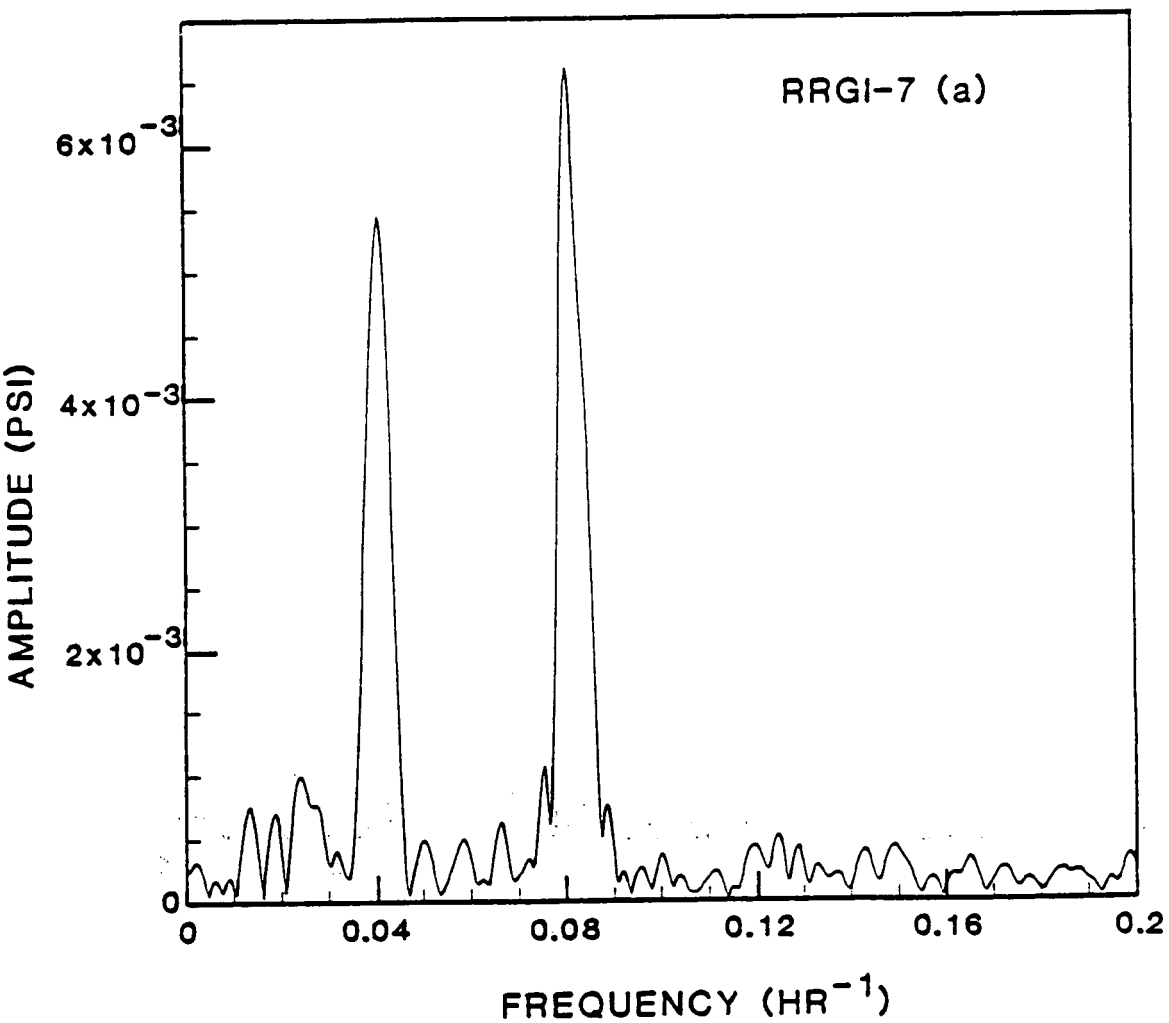

Figure 6.26. Fourier amplitude spectrum based on Finite Fourier transform.

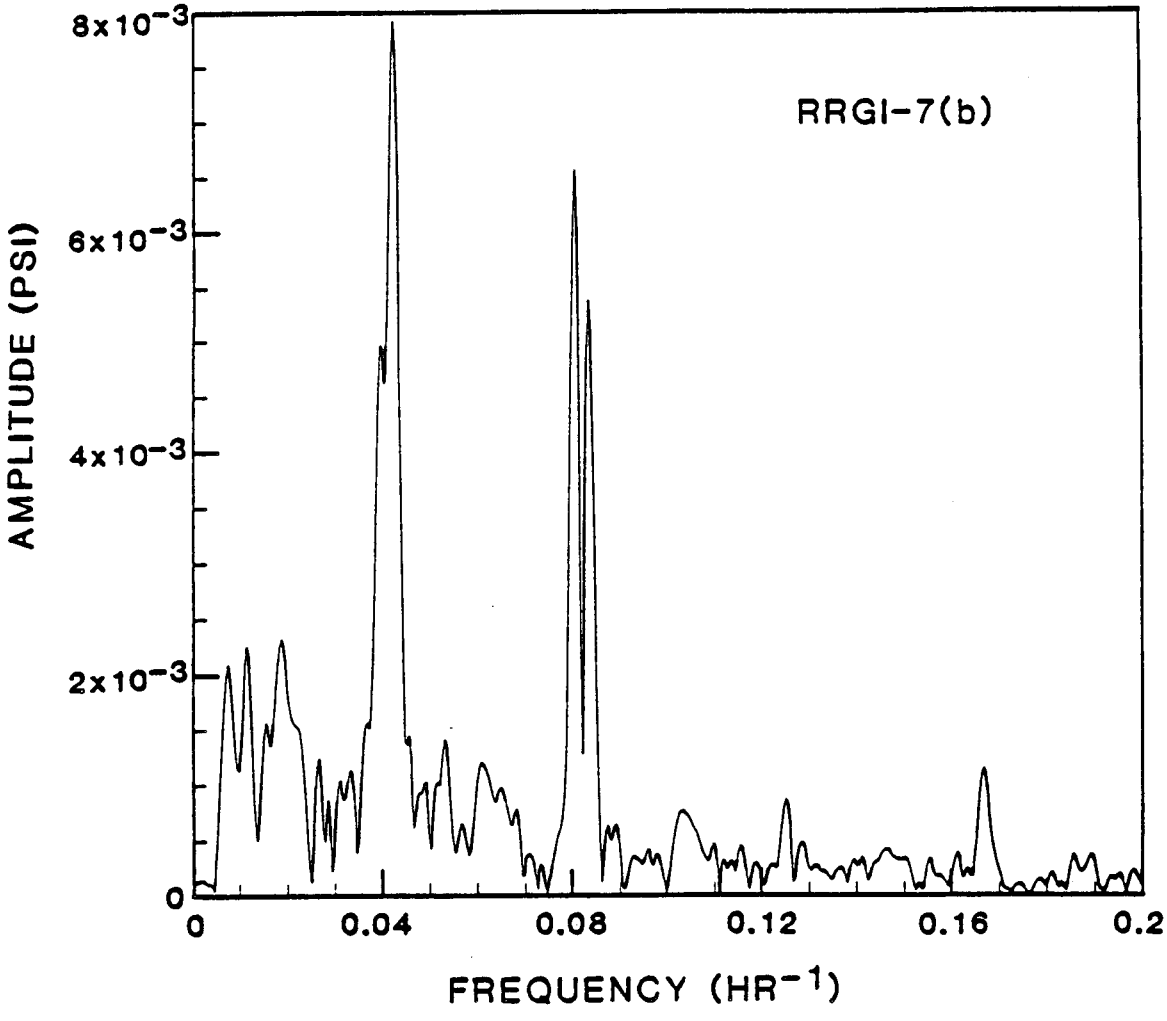

Figure 6.27. Fourier amplitude spectrum based on Finite Fourier transform.

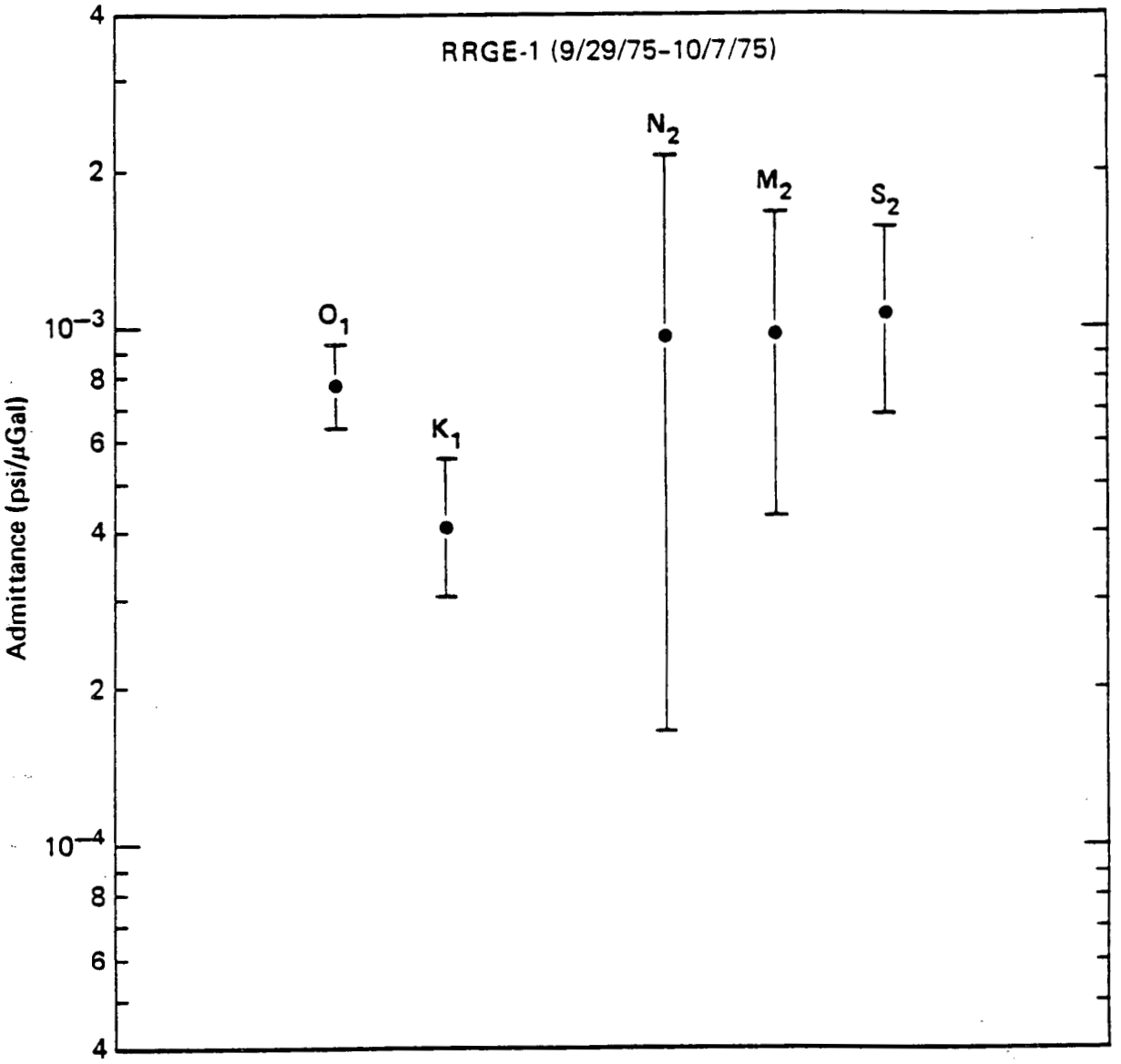

Figure 6.28. Computed tidal admittance showing 90% confidence intervals.

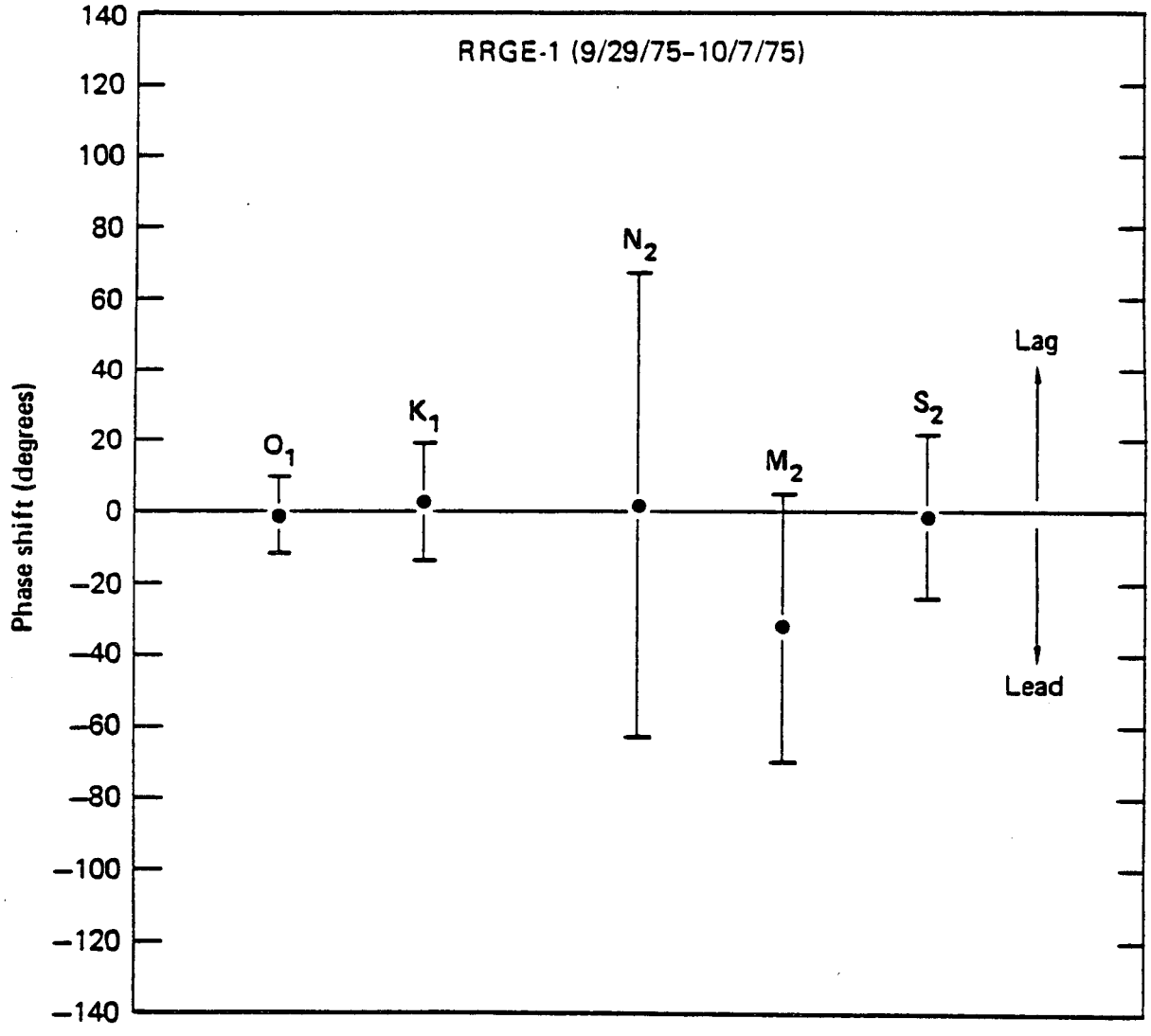

Figure 6.29. Computed phase shift showing 90% confidence intervals.

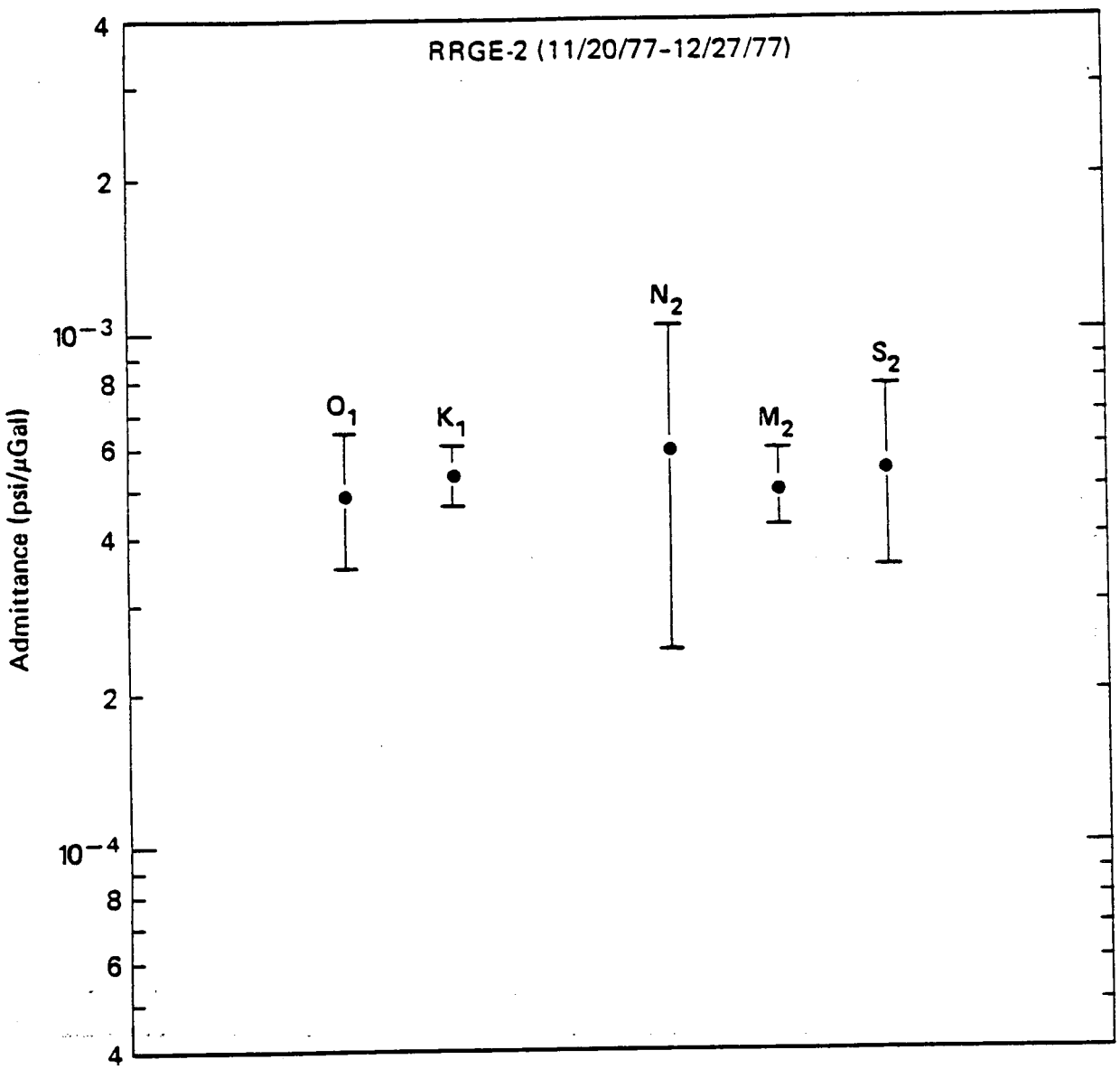

Figure 6.30. Computed tidal admittance showing 90% confidence intervals.

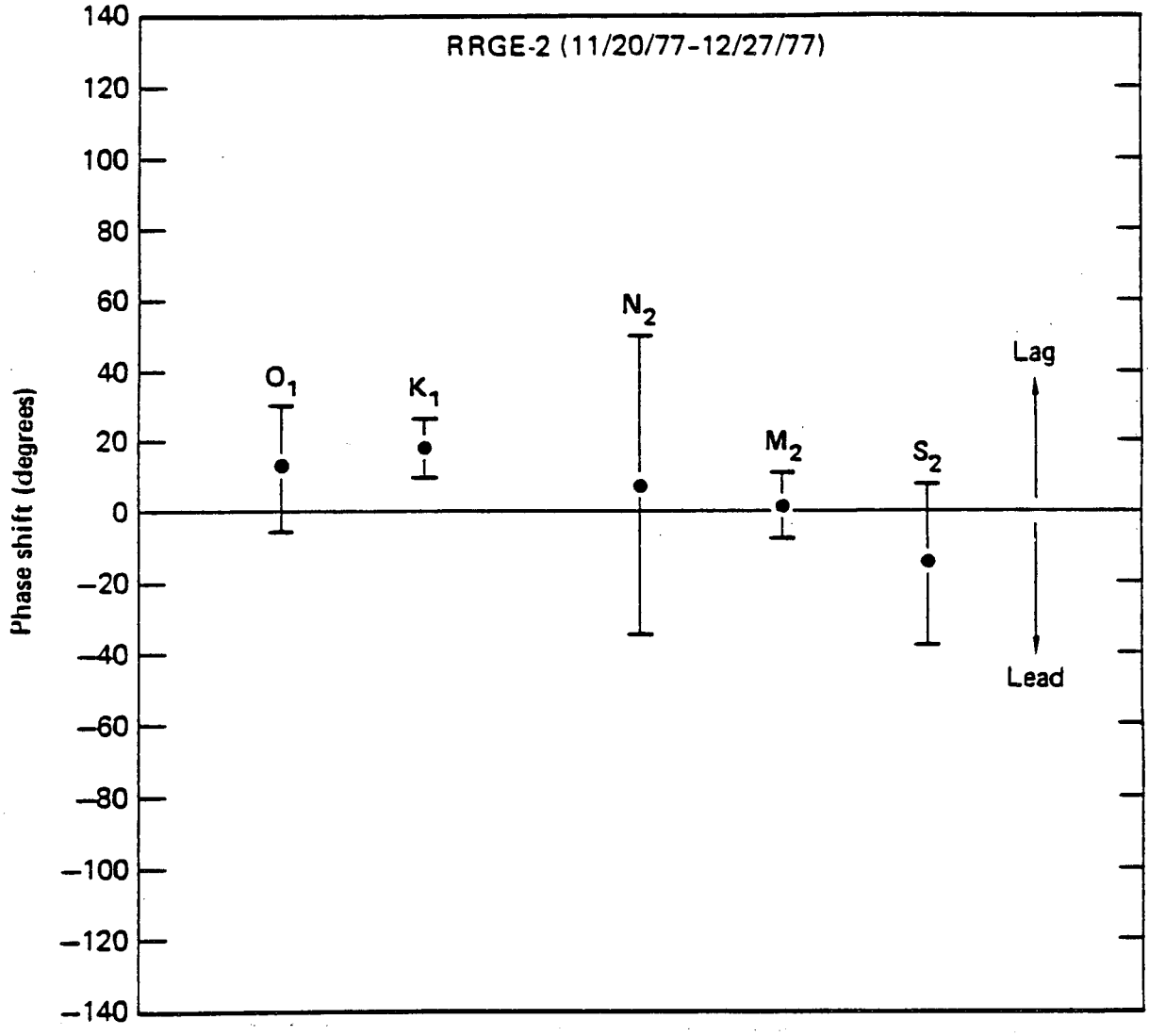

Figure 6.31. Computed phase shift showing 90% confidence intervals.

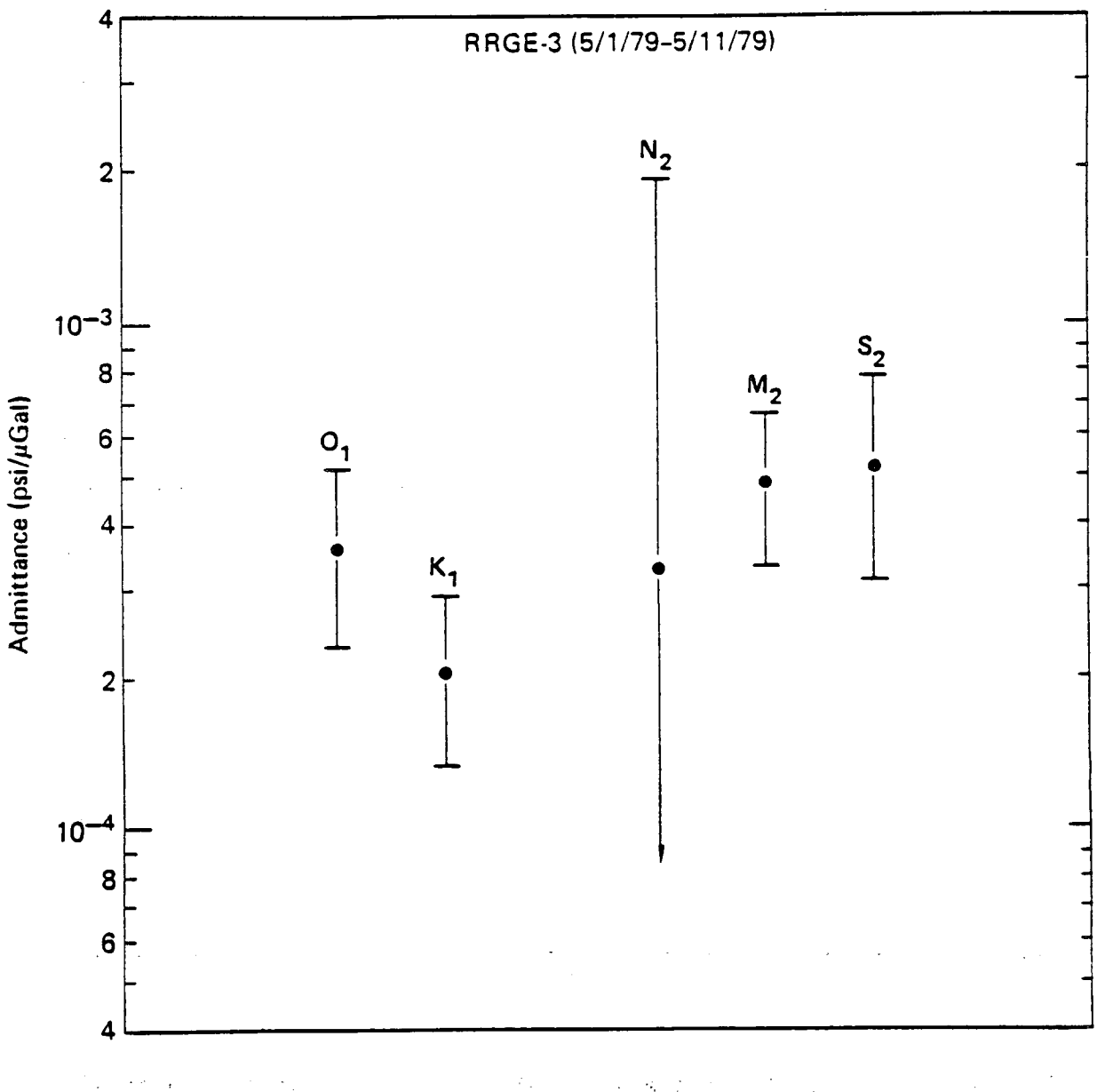

Figure 6.32. Computed tidal admittance showing 90% confidence intervals.

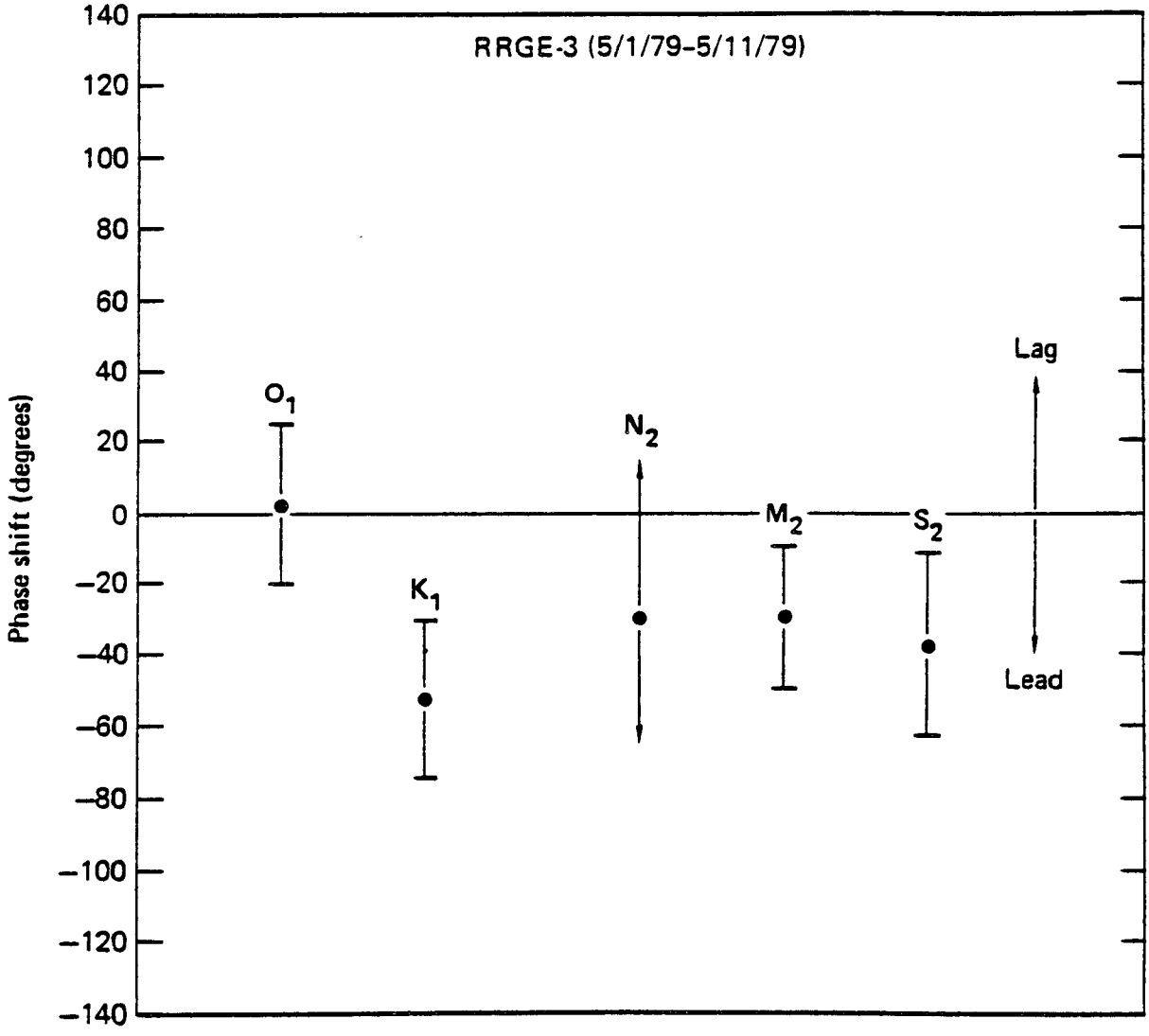

Figure 6.33. Computed phase shift showing 90% confidence intervals.

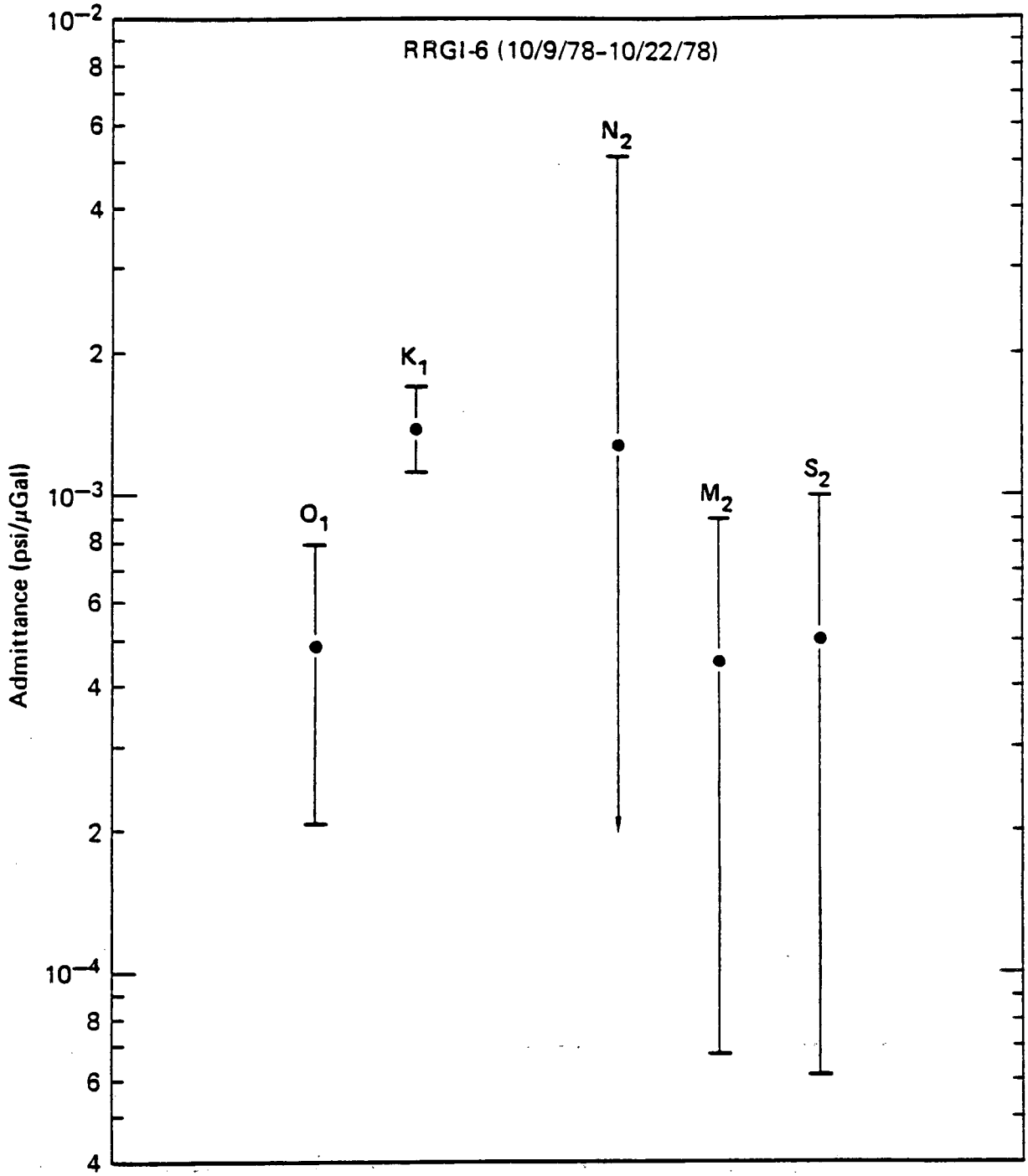

Figure 6.34. Computed tidal admittance showing 90% confidence intervals.

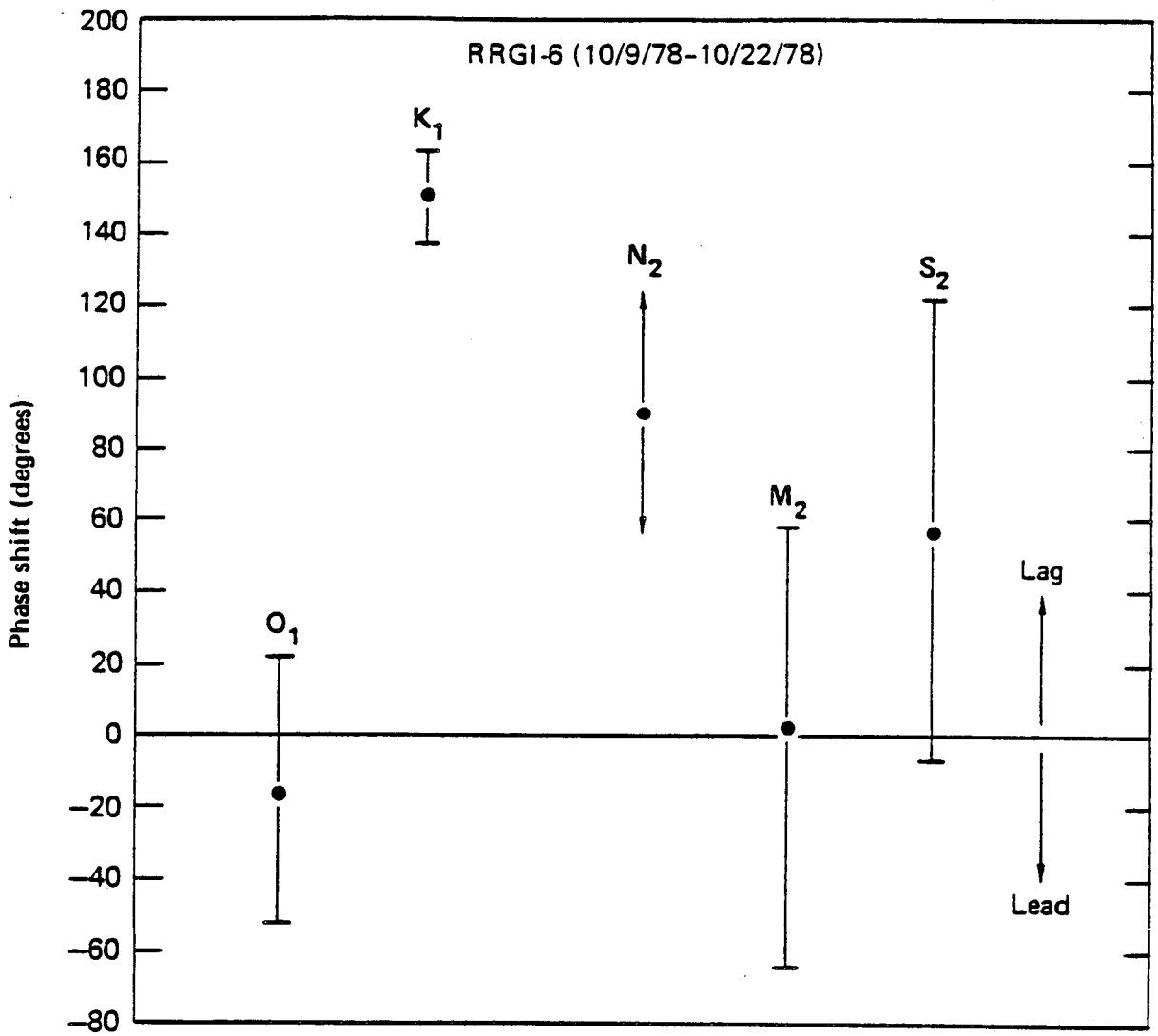

Figure 6.35. Computed phase shift showing 90% confidence intervals.

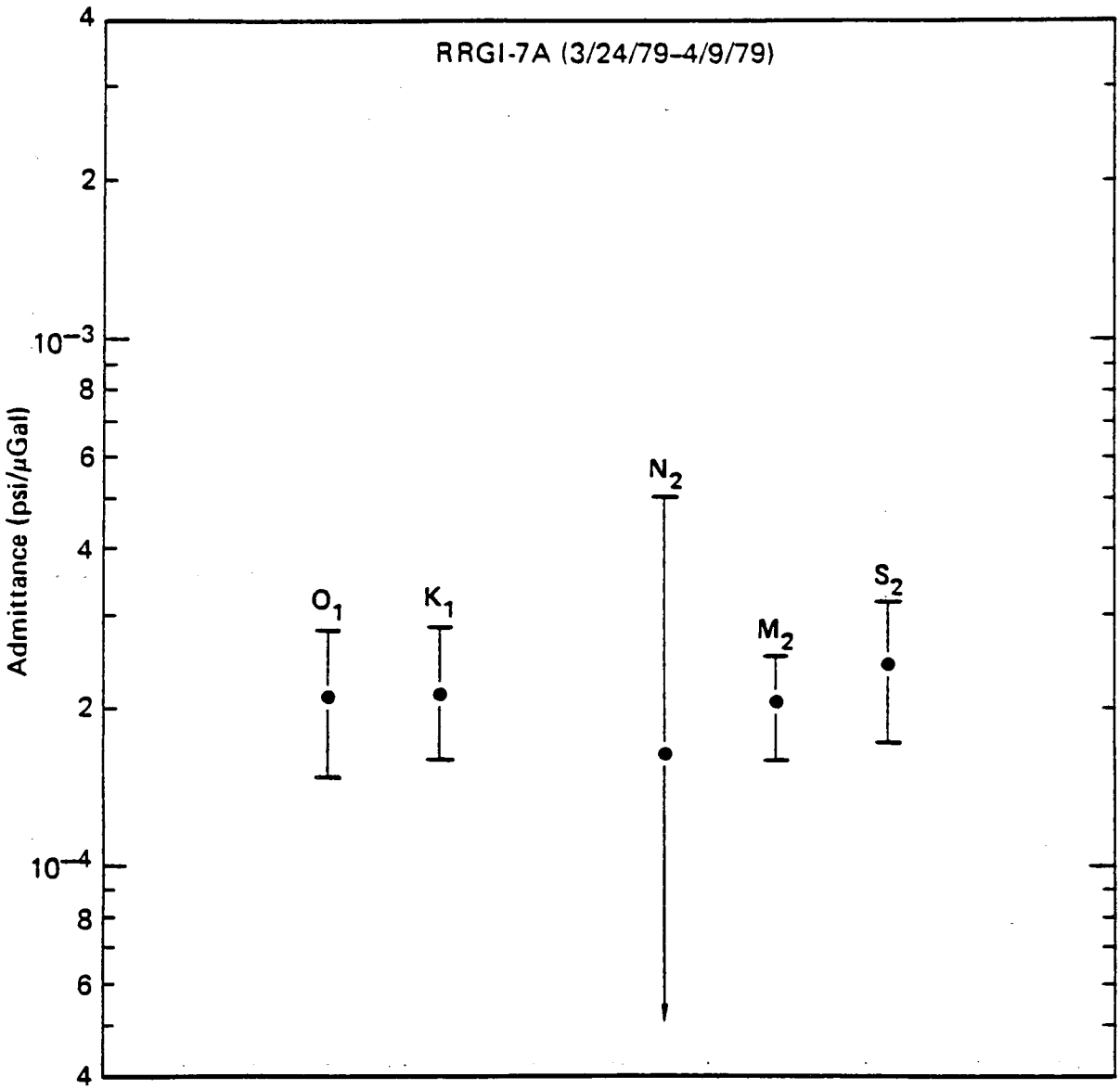

Figure 6.36. Computed tidal admittance showing 90% confidence intervals.

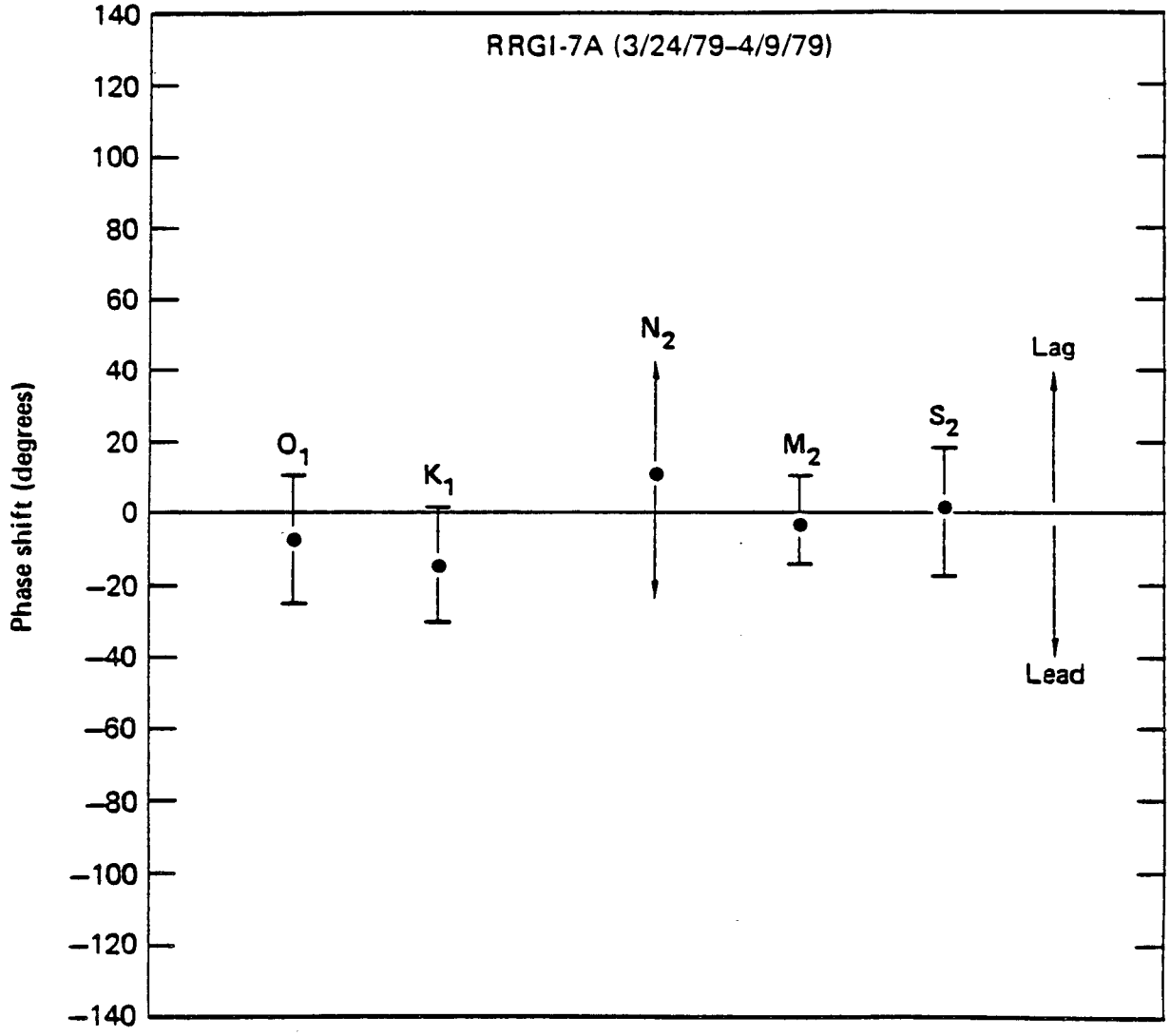

Figure 6.37. Computed phase shift showing 90% confidence intervals.

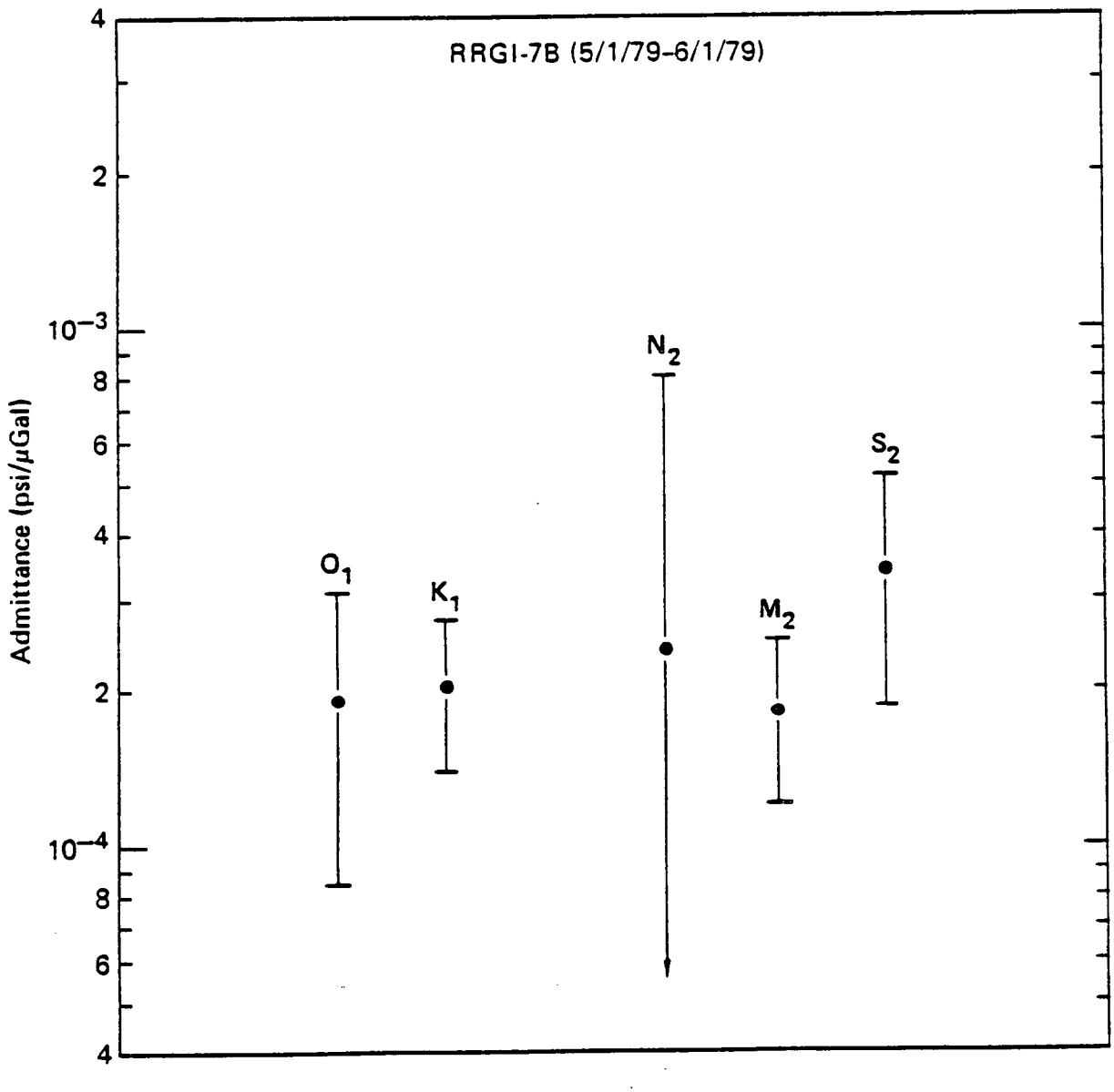

Figure 6.38. Computed tidal admittance showing 90% confidence intervals.

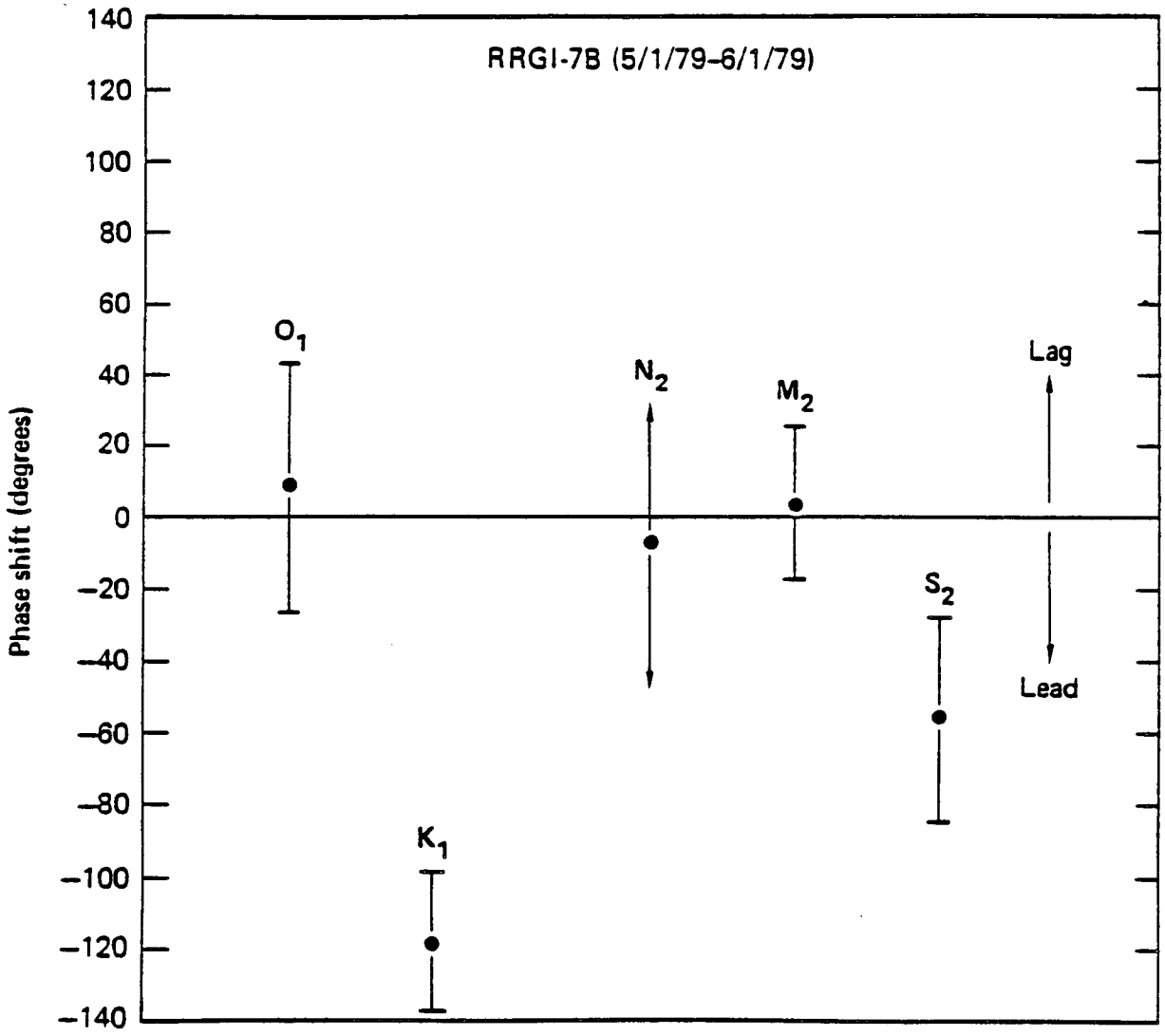

Figure 6.39. Computed phase shift showing 90% confidence intervals.

Wellhead temperature contaminated pressure at the K_1 and S_2 frequencies (solar tides) is clear in several of the wells analyzed, particularly RRGI-7B.

A confined aquifer model (see Chapter III) was applied to all of the wells for which data was available for the purpose of computing the specific storage coefficient and porosity. This was motivated primarily by an interest in determining the sensitivity of such a simple model for differentiating fracture porosity from pore porosity in a reservoir that exhibits both. Table 6.1 summarizes the results of this analysis. The effective stress constant α was taken to be 1 in the evaluation of ϕ and S_s. Only the lunar O_1 and M_2 tidal components were used in this and later analyses since the K_1 and S_2 components are of solar origin and may contain wellhead heating effects which will contaminate the measurement. The lunar N_2 tide is typically of such small amplitude as to yield a large statistical uncertainty, and therefore was not used in the analysis. The small calculated porosity and large total compressibility determined for RRGE-1,2 and 3 are consistent with the hypothesis that the primary production for these wells originates in fracture-dominated production zones. Flowmeter logs and temperature logs (Stoker, et al., 1977) as well as extensive core analyses (Dolenc, et al., 1981) for these wells confirm this hypothesis On the other hand, RRGI-6 and RRGI-7, which are completed in the sedimentary Salt Lake formation, have calculated porosities of 14% and 16%. These are well within the range of porosities measured by more conventional methods for the Salt Lake formation. Using values of permeability obtained from conventional well testing to estimate the hydraulic skin depth, it was found that the above porosity estimates are averages over distances between 2.5 and 5 km from the well. Calculated porosity for RRGE-4 was indicative of normal primary porosity even though RRGE-4 is of similar depth

Table 6.1

Summary of Computed Specific Storage and Porosity Values for the Raft River Geothermal Field

Well	ϕC_t (psi^{-1})	S_s (ft^{-1})	BE	ϕ	C_t (psi^{-1})
RRGE-1	3.3×10^{-7} (O_1)	1.4×10^{-7}	0.08	0.01	31.8×10^{-6}
RRGE-2	5.1×10^{-7} (M_2)	2.2×10^{-7}	0.18	0.04	14.2×10^{-6}
RRGE-3	5.3×10^{-7} (M_2)	2.3×10^{-7}	0.24	0.05	10.6×10^{-6}
RRGE-4	8.2×10^{-7} (M_2)	3.5×10^{-7}	0.75	0.24	3.4×10^{-6}
RRGI-6	5.3×10^{-7} (O_1)	2.3×10^{-7}	0.69	0.14	3.8×10^{-6}
RRGI-7	1.3×10^{-6} (M_2)	5.6×10^{-7}	0.30	0.16	8.1×10^{-6}

as RRGE-3 and also penetrates through the base of the Salt Lake formation into the metamorphic basement complex. In 1978, RRGE-4 was deepened by 137.2 m to a total depth of 1554.5 m. However, following recompletion neither fractures nor improved production were observed suggesting that primary production of RRGE-4 remained pore dominated. Core analysis (Communication from D. O. Enniss, Terra Tek to R. C. Stoker, EG&G Idaho, May 19, 1977) at the 640 m depth at RRGE-4 indicates an effective porosity of 24.5%, very close to the calculated results using the tidal response method.

A conventional injection test (Ahmed, et al., 1981) carried out in 1978 at RRGI-7 yielded a value for $S_s L$ of 1.2×10^{-3} using an assumed formation thickness L of 548.6 m. The tidal analysis method, using the same formation thickness, yields a value of 1.0×10^{-3} for the same well. Formation thickness for RRGE-1 and RRGE-2 is ill-defined due to the fractured and heterogeneous nature of the production zones in these wells. However, using the open-hole length as an effective formation thickness, the tidal response method yields a $S_s L$ of 1.8×10^{-4} and 4.8×10^{-4} for RRGE-1 and RRGE-2, respectively. A conventional long-term interference test (Narasimhan and Witherspoon, 1977) between these wells yielded a value of 9.4×10^{-4}. Differences between the tidal response method and the conventional pump test for these wells may be attributed to differences in the nature of the applied load and/or limitations of a confined aquifer models for interpreting fractured formations. No comparable conventional well test interpretations were available for RRGE-3, RRGE-4 or RRGI-6.

The differences in barometric efficiency and total compressibility between RRGI-6 and RRGI-7 are difficult to account for since both wells are completed in the same formation and both have similar depth. During an injection test at RRGI-7 in 1978, a pressure response was observed in RRGE-3 but no

pressure response was observed in RRGI-6 (Allman, 1978). The report concluded that the most likely explanation was reservoir heterogeneity in the vicinity of RRGI-6 and 7 allowing for a hydraulic connection between RRGI-7 and RRGE-3. This observation may explain the difference in barometric efficiency and total compressibility observed between RRGI-6 and RRGI-7 and the similarity of these parameters between RRGI-7 and RRGE-3.

The fracture orientation model was applied to tidal response data taken at RRGE-1, RRGE-2 and RRGE-3. Dip and strike were adjusted as discussed in Chapter III until the theoretical amplitude ratios and phase shifts of the lunar O_1 and M_2 tidal pressure responses matched the measured amplitude ratios and phase shifts. Uncertainties in the dip and strike estimates were computed by propagating the error in computed spectral estimates of the measured fluid pressure response as discussed in Chapter V. Figure 6.40 shows the range of computed strike for fractures intersecting RRGE-1, RRGE-2 and RRGE-3 at the 90% confidence level. RRGE-1 and RRGE-2 have similar computed strikes which are close to the strike of the Bridge fault. RRGE-3, however, has a computed strike consistent with the strike of the Narrows Structure. These results also suggest that, at a high confidence level, primary production at RRGE-1 and RRGE-2 comes from a set of fractures of distinctly different orientation than the production for RRGE-3. These conclusions based on the tidal response method are supported by water chemistry studies (Allen, et al., 1979) which indicate that the waters at RRGE-1 and RRGE-2 originate in the Bridge fault and are distinct from the waters at RRGE-3, which intersects the Narrows Structure. Conventional well testing at Raft River indicates that the reservoir is anisotropic in the vicinity of the production wells with the major axis of hydraulic conductivity lying roughly in the north-south direction (Dolenc, et al., 1981).

Figure 6.41 shows a histogram of fracture dip angles measured in core taken within 200 m of the sediment-crystalline basement decollement at RRGE-1 and RRGE-5 (Guth, et al., 1981). As indicated by the figure, the distribution is distinctly bimodal with the majority of the fractures having a dip between 40° and 80°. The tidal strain response analysis for dip, which is also shown on the figure, indicates that production is from the steeply dipping set of fractures.

Commercial borehole geophysical logging indicates that the Salt Lake formation sediments, in general, are not very permeable (Dolenc, et al., 1981). Also, near the base of the Salt Lake formation, considerable thermal alteration in the form of silica and calcite deposition has occurred (Covington, 1980). Therefore, the permeability contrast between the fractured production zones in RRGE-1,2 and 3 and the surrounding rock can be considered quite high. This suggests that the simple fracture model consisting of a high permeability fracture or set of fractures within an impermeable host rock is a reasonable first-order model for the fractured production zones at Raft River.

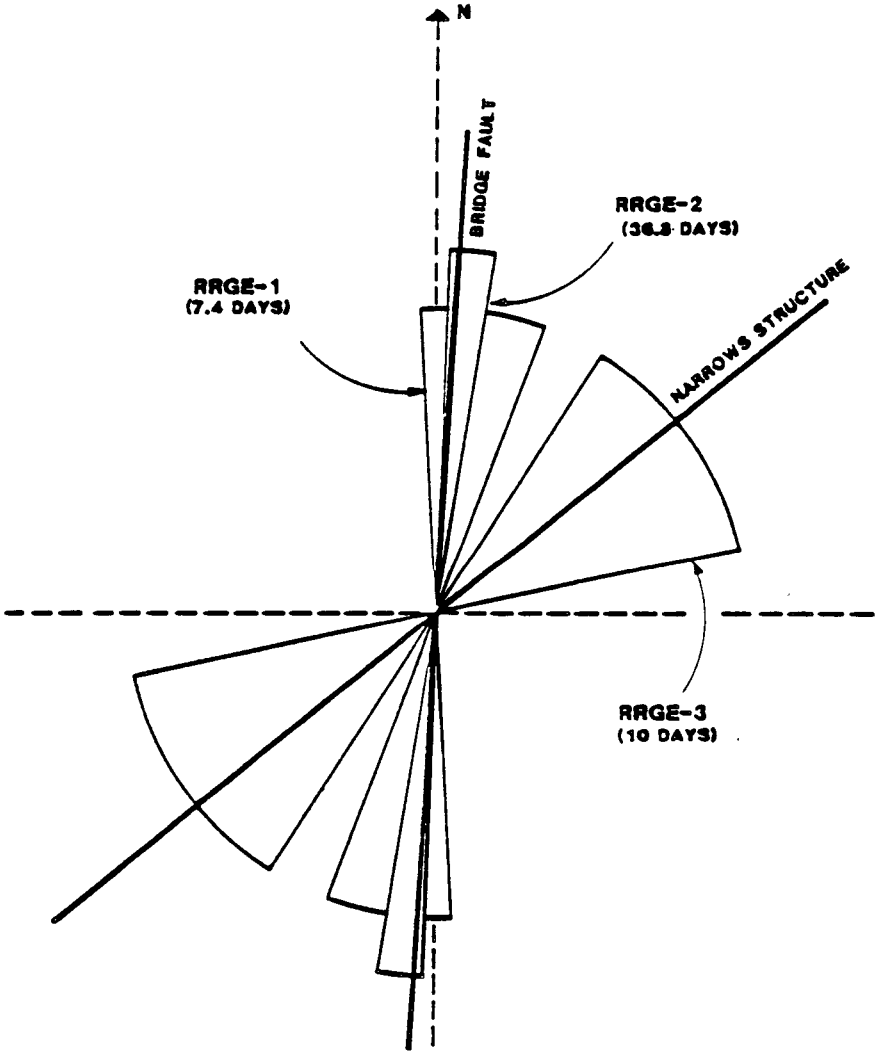

Figure 6.40. Computed fracture zone strike for RRGE-1, 2, and 3 showing 90% confidence strike sectors. Estimated strike based on surface geology and Landsat imagery is shown by labeled lines.

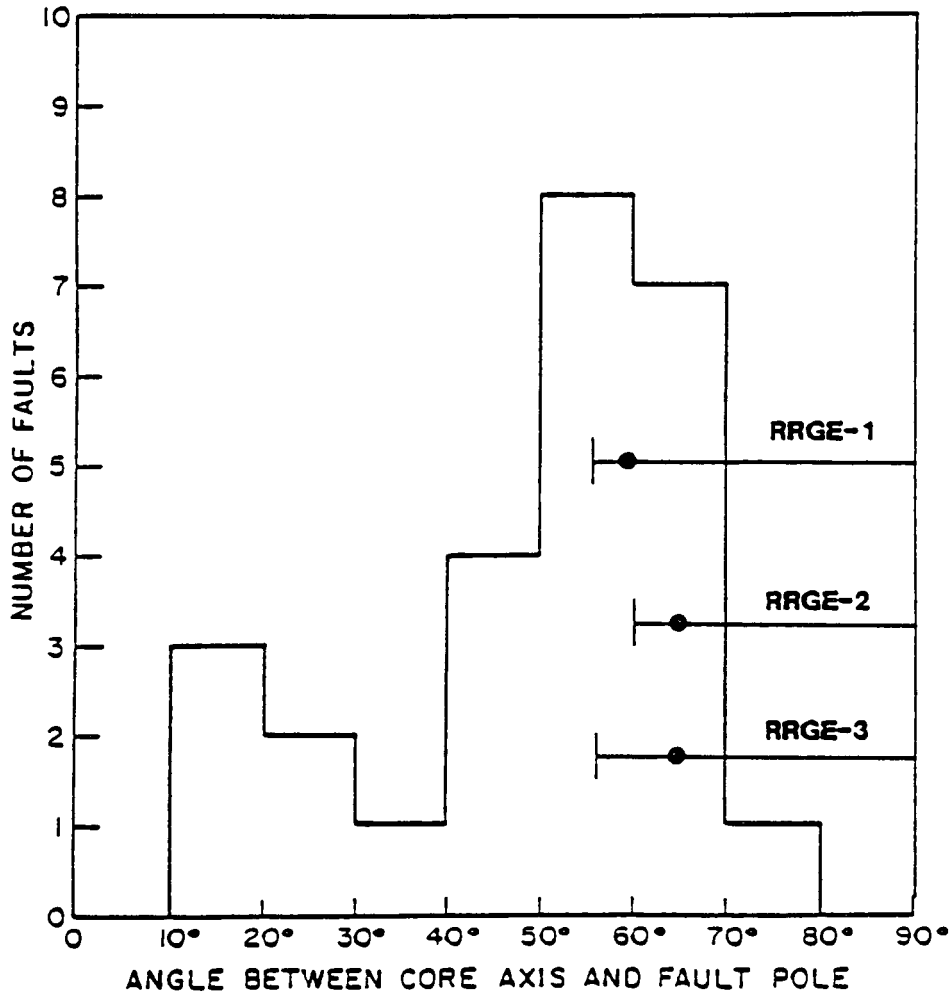

Figure 6.41. Histogram of dip angles of fractures in core taken at RRGE-1 and RRGE-5 (from Guth, et al., 1981). Dip estimates based on solid earth tidal strain method (solid circles) are superimposed with 90% confidence error bars.

CHAPTER VII

SUMMARY AND CONCLUSIONS

Considerable work has been carried out over the last two decades on characterizing pore pressure response to solid earth tidal strain and barometric pressure for the case of a homogeneous and isotropic porous rock. In some cases, these models have been used to interpret measured downhole or wellhead pressure in terms of porosity and storage. It has only been recently that the usefulness of solid earth tidal strain for characterizing discrete fractures in-situ has been recognized. This report presents an indirect confirmation of the method made through comparison with other information consisting of regional geology, geophysics, reservoir fluid chemistry and hydrology. In a more direct confirmation of the method, Bower (1982) carried out tidal strain fracture orientation analysis on shallow wells penetrating crystalline rock. This work was directed toward evaluating the method as a technique for characterizing discrete natural fractures in crystalline rock for the purpose of subsurface containment of radioactive waste. The tidal strain results were confirmed directly by lowering a borehole televiewer to the packed off section. Table 7.1 shows a comparison of the orientation using solid earth tidal strain and borehole TV. It should be emphasized that the borehole TV does not differentiate between producing and non-producing fractures and therefore some care must be taken in comparing these results. Furthermore, we emphasize that the borehole televiewer yields information about fractured orientation at the well face only. In the case of a borehole penetrating a pre-existing fracture, the televiewer results probably reflect the fracture orientation away from the wellbore. A stimulated fracture, however, will likely exhibit orientation at the wellface different from the orientation of the fracture away from the well

Table 7.1

Radioactive Waste Containment Tests -
Chalk River Nuclear Laboratories, Ontario
Canada, 1982 - Borehole CR8*

Packed Off Interval (m)	(Dip, Strike) Tidal Analysis	Borehole TV
180.8-196.7	(32°,278°)	(20°,280°), (53°,246°)
197.6-240.9	(37°,312°)	(36°,313°), (54°,316°)
275.3-281.1	(37°,228°)	(31°,248°)

*(1) Boreholes cased and perforated intervals packed off
(2) Completion in crystalline rock - no drainage effects.

From: Internal Report
Chalk River Nuclear Laboratories
June, 1982

face, causing a televiewer estimation to be incorrect. The tidal method, on the other hand, can see far from the well face. It is most encouraging that, at every packed-off interval, there is good correlation between fractures detected by the borehole TV and the orientation evaluated on the basis of solid earth tidal strain. These results, along with the work carried out at the Raft River system, indicate that the analysis of pore pressure response to solid earth tidal strain can be an exceedingly powerful tool for determining fracture orientation.

The advantages of the solid earth tidal strain approach for fracture orientation analysis are many. Unlike potential field methods (e.g. resistivity, IP, magnetic proppants, etc.) and most seismic methods, the tidal strain method has no depth limitations. As in all methods based on fluid pressure transient analysis, the signal propagation speed is almost instantaneous when compared with the actual fluid velocity. Therefore, the ability to predict the migration of injected fluid in a reservoir far exceeds conventional tracer methods which track the fluid directly. By the time tracer methods indicate a problem associated with waste water reinjection, it is likely to be too late to take corrective action to reduce the problem to an acceptable level. Another advantage of the tidal strain method is the modest equipment necessary to carry out the procedure. Wellhead or downhole fluid pressure measurement and simultaneous barometric pressure measurement over a period of a few weeks is required. Sufficient pressure measurement resolution is obtained with "off-the-shelf" quartz pressure gauges.

What is clearly indicated at present is the need for an expanded data base to test more thoroughly the tidal strain response models. The method has been applied to date only to fractures exhibiting minimal drainage to the formation. In the work by Bower (1982), the formation permeability was in the

microdarcy range characteristic of granites. For the case of the Raft River system, considerable thermal alteration in the form of silica and calcite deposition in the pores had occurred in the basement Palezoic metasedimentary complex. As a result, the formation permeability was greatly reduced. One cannot typically expect to find this optimum situation. Horizons for geothermal waste water reinjection are usually chosen for the opposite reason -- namely a moderately high permeability for the purpose of minimizing pumping costs associated with reinjection. Often times, however, a large part of the observed permeability in injection horzons can be attributed to fractures or other high permeability channels. A good example of this is given by Einarsson, et al. (1975), for the case of geothermal waste water injection at the Ahuachapán geothermal field in El Salvador. A rapid response at one of the wells due to the injection of a tritium tracer slug at a nearby well clearly indicated channelling, although the total quantity of tritium recovered indicated that most of the injected tritium was lost by migration into the formation. Another example of flow channelling in injection horizons has been given in this report. The difference in barometric efficiency found between the injection wells RRGI-6 and RRGI-7 at Raft River and the similarity between the barometric efficiency between RRGI-7 and the production well RRGE-3 suggests very strongly that the horizon chosen for reinjection at Raft River is not isotropic. This was confirmed by a conventional pump test that indicated a hydraulic connection between RRGE-3 and RRGI-7. The nature of this connection is not totally clear although the tidal analysis indicates that it is not a simple non-draining fracture. The calculated connected porosity is much more consistent with a porous injection horizon (the Salt Lake Formation) than with a fracture.

Further testing and use of the tidal strain method in the field is clearly warranted based on the results obtained at the Raft River Geothermal Field in Idaho and at the Chalk River Nuclear Laboratories in Canada. Several likely candidates for future field testing of the tidal strain method are: 1) continued work at Raft River, 2) the Fenton Hill "Hot Dry Rock" system in New Mexico, 3) geothermal systems in the Salton Trough in Southern California, and 4) other systems in the Basin and Range province. This list contains most of the expected geologic and hydrologic environments likely to be encountered in future geothermal development. Potential sites, however, should not be limited to these alone. The Raft River system is a most appropriate candidate in that a considerable amount of knowledge has accumulated over the past decade regarding the regional and local structure and extent of the hydrothermal system. The reservoir exhibits both fracture and pore porosity as well as a demonstrated large scale hydraulic connection between the shallower pore-dominated and deeper fracture-dominated regimes. The conclusions drawn in this report regarding the Raft River system are based on tidal response data obtained from conventional well tests. A field experiment tailored specifically for tidal strain response analysis at this reservoir would no doubt improve the resolution of the data and therefore refine the conclusions reached in this report.

The Fenton Hill "Hot Dry Rock" system in New Mexico, conceived and established by Los Alamos Scientific Laboratory (LASL), is a man-made fracture system in deep, hot crystalline rock. Cold water is injected into the fracture system via an intersecting borehole, is subsequently heated by the rock, and the hot water is then removed from the system through a second intersecting borehole. Although the long-term economic viability of this type of system for electrical power production has yet to be verified, there is considerable interest, both in the U.S. and abroad, in its space heating applica-

tions. Response of the Fenton Hill system to solid earth tidal strain has been observed and is roughly 0.02-0.04 psi (personal communication, J. Albright, LASL). The application of tidal strain analysis to this kind of system include: 1) fracture orientation analysis, necessary for successfully intersecting the hydraulic fracture with the second borehole, 2) evaluation of effective fracture size, and 3) long-term fracture dilatancy due to thermoelastic effects.

The Salton Trough is a northward extension of the Gulf of California spreading center. It is an extensive region of crustal thinning, faulting, and dike injection which has resulted in many near surface thermal anomalies of large magnitude. Considerable thermal alteration in the form of silica deposition within many of the thermal reservoirs has resulted in the establishment of fracture-dominated systems. Local on-going tectonic activity associated with the Pacific-North American plate interaction keeps these fracture systems open. Environmental requirements necessitate that the produced fluid, which is extremely saline (up to 300,000 ppm total dissolved solids), be reinjected. Reinjection is also a most important consideration in the Imperial Valley, where ground subsidence has the potential of modifying the gravity-driven irrigation in this heavily agricultural area. Pore pressure response to solid earth tides has been observed at the Salton Sea Geothermal Field (Hanson, 1979) and at the East Mesa Geothermal Field (Kanehiro, 1980).

Finally, a typical "Basin and Range" type reservoir should be considered for the reasons that: 1) these are structurally dominated system usually controlled by steeply dipping normal faults, and 2) these types of systems dominate all others in number of occurrences and total thermal energy in the U.S. and will probably represent the future "type" system for geothermal energy exploitation.

The immediate applications of earth tide analysis to geothermal reservoirs are three-fold: 1) as a complementary method to be used with conventional pressure transient testing for characterizing the nature of the fluid conduits (pore or fracture) within the production and injection zones, 2) as a method for determining the structural nature (i.e. spatial orientation) of the fluid conduits, and 3) as a method for monitoring long-term structural modification of the reservoir due to extensive production or injection which results in significant changes in effective stress. An example of the latter is given in Figure 7.1. This figure shows the measured wellhead pressure history of a shut-in oil well in a Western Canadian oil field (Hanson, 1982). This particular well, which had been hydraulically fractured, produces from a formation that is also slightly fractured. The well was shut-in shortly after nearby wells had undergone a period of injection. It is clear from this figure that above a certain reservoir pressure, roughly 1330 psi, the behavior of the reservoir is as one would expect based on the results of Chapters II and III. At a 90% confidence level, the pore pressure response to tidal strain was less than 0.1 psi while the static pressure stayed above a critical pressure of 1300 psi. However, an interesting phenomena occurred as the reservoir pressure dropped below this critical pressure. During this phase, the response to tidal strain emerged and indeed was amplified over the expected response. Figure 7.2 shows a maximum entropy amplitude spectrum of a 50 hour segment of the data between t = 410 hours and t = 460 hours. There are two possible explanations for the amplification. The first is that the fractures were deforming "globally" rather than "locally". Formulation presented in Chapter III uses a local fracture deformation expression (equation III.35) which does not take into account the effect of fracture size on fracture dilatance. If this were done, the observed amplication can be easily explained (Hanson,

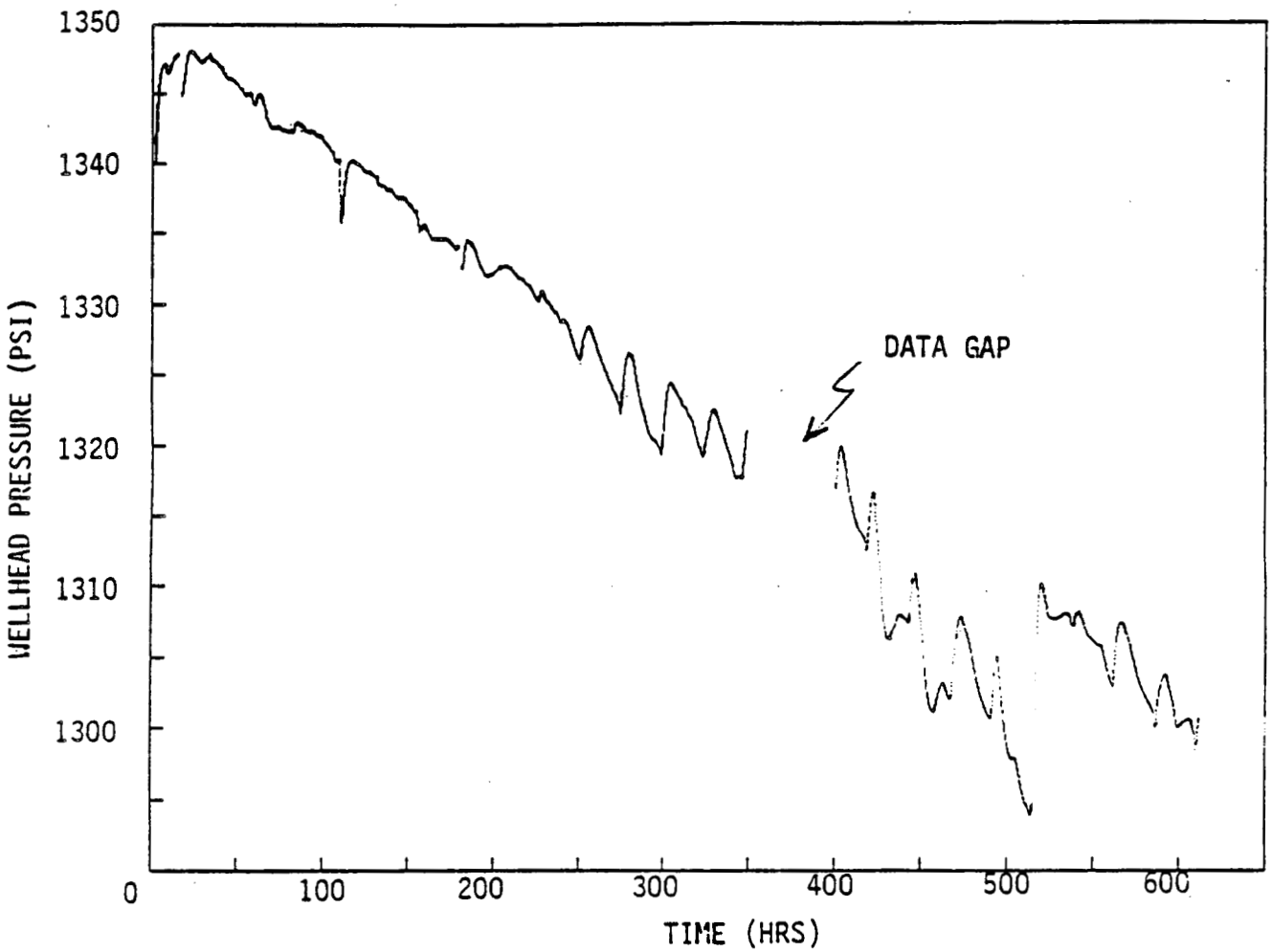

Figure 7.1. Measured wellhead pressure at a stimulated well in a Western Canadian oil field.

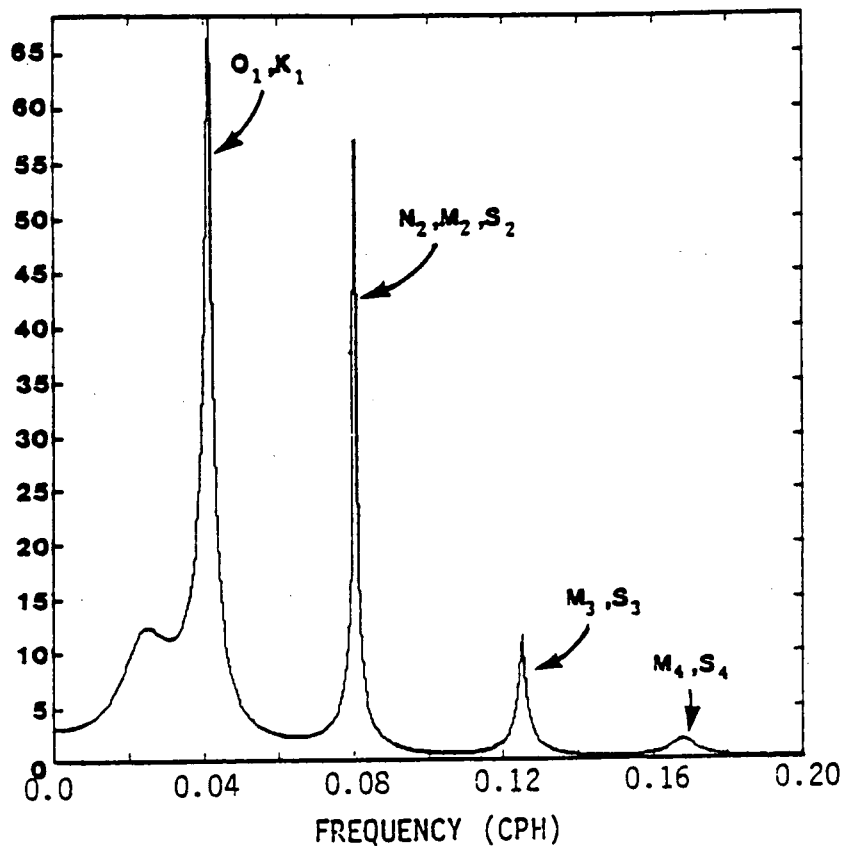

Figure 7.2. Maximum entropy amplitude spectrum of a portion of the data shown in Figure 7.1. Analysis is on 50 hours of data, from t = 410 hrs to t = 460 hrs. Amplitude is in arbitrary units.

1982). The other possibility is some sort of resonance effect between the fracture elasticity and borehole storage (see for example Bodvarsson and Bjornsson, 1976). In any event, it is clear that the response to tidal strain was very dependent on effective stress. An understanding of this dependency will be extremely useful for evaluating the dynamics of fracture systems including in-situ fracture aperture-effective stress interrelationships.

The tidal amplification question is but one of several questions that need to be answered. Others include: 1) effects of formation permeability anisotropy and formation compressibility anisotropy on the determination of fracture orientation, 2) connection of the primary subsurface fluid conduit with other conduits with different hydraulic characteristics or spatial orientation, 3) the effect of non-ideal fracture geometry on tidal response, 4) optimization of data acquisition methods for improved resolution, and 5) the practical feasibility of accounting for ocean loading effects in the models.

BIBLIOGRAPHY

Ahmed, U., K. Wolgemuth, A.S. Abou-Sayed, J.F. Schatz and A.H. Jones, "Raft River Geothermal Site: A Reinjection Study." Geothermal Res. Council, Trans., V. 4, September 1980.

Allen, C.A., R.E. Chaney, and R.E. McAtee, "Geochemical Modeling at Raft River," Geothermal Resources Council Trans., V. 3, 1979.

Allman, D.W., "Air Lift and Injection Testing on RRGI-7 from August 1, 1978 to August 3, 1978," EG&G Idaho, Internal Report, 1978.

Alsop, L.E. and J.T. Kuo, "The Characteristic Numbers of Semi-Diurnal Earth Tidal Components for Various Earth Models," Ann. Geophys., V. 20, 1964.

Arditty, P., "The Earth Tide Effects on Petroleum Reservoirs; Preliminary Study," Stanford Geothermal Program Report SGP-TR-34, 1978.

Arditty, P. and H.J. Ramey, "Response of a Closed Well-Reservoir System to Stress Induced by Earth Tides," SPE Paper 7484, Houston, Texas, 1978.

Armstrong, R.L., "Mantled Gneiss Domes in the Albion Range, Southern Idaho," Geol. Soc. Am. Bull., 79, p. 1295, 1968.

Beaumont, C. and J. Berger, "An Analysis of Tidal Strain Observations from the United States of America: I. The Laterally Homogeneous Tide," Bull. Seis. Soc. Am., 65, 6, 1975.

Berger, J. and F. Wyatt, "Some Observations of Earth Strain Tides in California," Phil. Trans. R. Soc. Lond. A., 274, 1973.

Berger, J. and C. Beaumont, "An Analysis of Tidal Strain Observations from the United States of America: II, The Inhomogeneous Tide," Bull. Seis. Soc. Am., 66, 6, 1976.

Biot, M.A., "General Theory of Three-Dimensional Consolidation," J. App. Phys., 12, 1941.

Blair, D., "Fourier Contamination of a Finite Length of Data in Tidal Analysis," Geophys. J.R. astr. Soc., 59, 1979.

Bodvarsson, G., "Confined Fluids as Strain Meters," J. Geophys. Res., 75, 14, 1970.

Bodvarsson, G. and A. Bjornsson, "Hydroelastic Cavity Resonators," Jökull, 26, 1976.

Bodvarsson, G. and J.M. Hanson, "Geothermal Reservoir Testing Based on Signals of Tidal Origin," Proc. 4th Workshop on Geothermal Reservoir Engineering, Stanford Univ., 1978.

Bower, D.R., Fracture Parameters From the Interpretation of Well Tides," J. Geophys. Res., 1983 (in press).

Bower, D.R. and K.C. Heaton, "Response of an Aquifer Near Ottawa to Tidal Forcing and the Alaskan Earthquake of 1964," Can. J. Earth Sci., 15, 3, 1978.

Bredehoeft, J.D., "Response of Well-Aquifer Systems to Earth Tides," J. Geophys. Res., 72, 12, 1967.

Bullen, K.E., The Earth's Density, John Wiley & Sons, 1975.

Chapman, S. and K.C. Westfold, "Comparison of the Annual Mean Solar and Lunar Atmospheric Tides in Barometric Pressure, as Regards Their Worldwide Distribution of Amplitude and Phase," Jour. Atmos. and Terres. Phys., 8, 1956.

Cinco-Ley, H. and F. Samaniego-V, "Transient Pressure Analysis for Fractured Wells," J. Pet. Tech., pp. 1749-1766, 1981.

Compton, R.R., "Geologic Map of the Yost Quadrangle, Box Elder County, Utah, and Cassia County, Idaho," U.S.G.S. Misc. Geol. Inv. Map I-672, 1972.

Covington, H.R., "Subsurface Geology of the Raft River Geothermal Area, Idaho," Geothermal Resources Council Trans., V. 4, 1980.

DeWeist, R.J.M., "On the Storage Coefficient and the Equations of Groundwater Flow," J. Geophys. Res., 71, 4, 1966.

Dolenc, M.R., L.C. Hull, S.A. Mizell, B.F. Russell, P.A. Skiba, J.A. Strawn, and J.A. Tullis, "Raft River Geosciences Case Study," EG&G Idaho, Report EGG-2125, V. I, II, 1981.

Duguid, J.O. and P.C.Y. Lee, "Flow in Fractured Porous Media," Water Res. Research, 13, 3, 1977.

Einarsson, S., A. Vides, R., and G. Cuellar, "Disposal of Geothermal Waste Water by Reinjection," Proc. 2nd U.N. Symp. on the Dev. and Use of Geothermal Res., San Francisco, May 1975.

Farrell, W.E., "Global Calculations of Tidal Loading," Nat. Phys. Sci., 238, 1972.

Farrell, W.E., "Earth Tides," Rev. Geophys. and Space Phys., 17, 6, 1979.

Felix, C.E., "Geology of the Eastern Part of the Raft River Range, Box Elder County, Utah," in Guidebook to the Geology of Parts of Northwestern Utah, Utah Geol. Soc., 11, pp. 76-97, 1956.

George, W.O. and F.E. Romberg, "Tide-Producing Forces and Artesian Pressures," Trans. Am. Geophys. Union, 32, 3, 1951.

Godin, G., The Analysis of Tides, Univ. of Toronto Press, 1972.

Goldman, S., Information Theory, Dover Publications, 1968.

Guth, L.R. R.L. Brahn, and S.L. Beck, "Fault and Joint Geometry at Raft River Geothermal Area, Idaho," Univ. of Utah, Report DOE-ID-12079-41, 1981.

Hanson, J.M., "Tidal Pressure Response Well Testing at the Salton Sea Geothermal Field, California and Raft River, Idaho, Proc. 5th Workshop on Geothermal Reservoir Engineering, Stanford Univ., 1979.

Hanson, J.M. and L.B. Owen, "Fracture Orientation Analysis by the Solid Earth Tidal Strain Method," SPE Paper 11070, New Orleans, LA, 1982.

Hanson, J.M., "In-Situ Fracture Characterization - A New Approach Using Multi-Frequency Flow Testing," Proc. 24th U.S. Symposium on Rock Mechanics, Texas A&M Univ., June 20-23, 1983 (in press).

Harrison, J.C., N.F. Ness, I.M. Longman, R.F.S. Forbes, E.A. Kraut, and L.B. Slichter, "Earth-Tide Observations Made During the International Geophysical Year," J. Geophys. Res., 68, 5, 1963.

Harrison, J.C., "New Computer Programs for the Calculation of Earth Tides," NOAA, Univ. of Colorado, CIRES, 1971.

Harrison, J.C., "Cavity and Topographic Effects in Tilt and Strain Measurement," J. Geophys. Res., 81, 2, 1976.

Jacob, C.E., "On the Flow of Water in an Elastic Artesian Aquifer," Trans. Am. Geophys. Union, Part 2, 1940.

Kanehiro, B.Y., "The Response of Aquifers to the Earth Tides," M.S. Thesis, Univ. of California, Berkeley, 1980.

King, G.C.P. and R.G. Bilham, "Strain Measurement Instrumentation and Technique," Phil. Trans. R. Soc. Lon. A., 274, 1973.

Khorosheva, V., "Effect of the Atmospheric Pressure on the Tilting of the Earth's Surface," Izv., Geophys. Ser., 1958.

Kuo, J.T., R.C. Jachens, M. Ewing, and G. White, "Transcontinental Tidal Gravity Profile Across the United States, Science, 168, 1970.

Lambert, A., "The Response of the Earth to Loading by the Ocean Tides around Nova Scotia," Geophys. J. R. astr. Soc., 19, 1970.

Longman, I.M., "Formulas for Computing the Tidal Accelerations Due to the Moon and the Sun," J. Geophys. Res., 64, 12, 1959.

Mabey, D.R., D.B. Cooper, J.E. O'Donnell, and C.W. Wilson, "Reconnaissance Geophysical Studies of the Geothermal System in Southern Raft River Valley, Idaho," Geophysics, 43, 7, 1978.

Major, M.W., G.H. Sutton, J. Oliver, and R. Metsger, "On Elastic Strain of the Earth in the Period Range 5 seconds to 100 hours," Bull. Seis. Soc. Am., 54, 1, 1964.

Marine, I.W., "Water Level Fluctuations Due to Earth Tides in a Well Pumping From Slightly Fractured Crystalline Rock," Water Res. Research, 11, 1, 1975.

Melchior, P., The Earth Tides, Pergamon, 1966.

Melchior, P., The Tides of the Planet Earth, Pergamon, 1978.

Morland, L.W., "Earth Tide Effects on Flows in Horizontal Permeable Elastic Layers Connected to Wells," Geophys. J. R. astr. Soc., 51, 1977.

Munk, W. and K. Hasselmann, "Super-Resolution of Tides," Studies on Oceanography, pp. 339-344, 1964.

Narasimhan, T.N. and P.A. Witherspoon, "Reservoir Evaluation Tests on RRGE-1 and RRGE-2, Raft River Geothermal Project, Idaho," Univ. of Calif. Report LBL-5958, 1977.

Nur, A. and J.D. Byerlee, "An Exact Effective Stress Law for Elastic Deformation of Rock with Fluids," J. Geophys. Res., 76, 26, 1971.

Prothero, W.A. and J.M. Goodkind, "Earth-Tide Measurements with the Superconducting Gravimeter," J. Geophys. Res., 77, 5, 1972.

Rhoads, G.H., Jr., "Determination of Aquifer Parameters from Well Tides," M.S. Thesis, Virginia Polytechnic Institute and State University, 1976.

Rice, J.R. and M.P. Cleary, "Some Basic Stress Diffusion Solutions for Fluid-Saturated Elastic Porous Media with Compressible Constituents," Rev. Geophys. Space Phys., 14, 1976.

Richardson, R.M., "Tidal Fluctuations of Water Level Observed in Wells in East Tennessee," Trans. Am. Geophys. Union, 37, 4, 1956.

Robinson, E.S. and R.T. Bell, "Tides in Confined Well-Aquifer Systems," J. Geophys. Res., 76, 8, 1971.

Robinson, T.W., "Earth-Tides Shown by Fluctuations of Water-Levels in Wells in New Mexico and Iowa," Trans. Am. Geophys. Union, Reports and Papers, Hydrology, 1939.

Rosato, N.D., C.O. Bennett, A.C. Reynolds, and R. Raghavan, "Analysis of Short-Time Buildup Data for Finite-Conductivity Fractures," J. Pet. Tech., pp. 2413-2422, 1982.

Snow, D.R., "Fracture Deformation and Changes of Permeability and Storage Upon Changes in Fluid Pressure," Quart. Colo. Sch. of Mines, 63, 1, 1968.

Stehfest, H., "Algorithm 368," Collected Algorithms from CACM, 1969.

Sterling, A. and E. Smets, "Study of Earth Tides, Earthquakes and Terrestrial Spectroscopy by Analysis of the Level Fluctuations in a Borehole at Heibaart (Belgium)," Geophys. J. R. astr. Soc., 23, 1971.

Stoker, R.C., D. Goldman, and J.F. Kunze, "Deducing Production Zones From Well Logs," Geothermal Resources Council Trans., V. 1, 1977.

Takeuchi, H., "On the Earth Tide of the Compressible Earth of Variable Density and Elasticity," Trans. Am. Geophys. Union, 31, 5, 1950.

Tanaka, T., "On the Effect of Atmospheric Pressure Upon Ground Tilt," Bull. Disas. Prev. Res. Inst., Kyoto Univ., 18, 2, 1968 (abstract).

Tanaka, T., "On the Effect of Atmospheric Pressure Upon Ground Tilt," Bull. Disas. Prev. Res. Inst., Kyoto Univ., 18, 2, 1968.

Trubytsyn, A.P. and A.V. Makalin, "Deformations of the Earth's Crust Due to Atmospheric Cyclones," Izv., Earth Physics, 5, 1976.

Urmantsev, F.M., "Barometric and Surface Inclinations and Their Effect on the Determination of Contemporary Vertical Movements of the Earth's Crust by the Geodetic Method," Izv., Earth Physics, 6, 1970.

Urmanstev, F.M., "An Estimate of the Effect of the Diurnal Variations of Atmospheric Pressure on Gravimeter and Tiltmeter Readings on Precise Leveling Work," Izv., Earth Physics, 3, 1975.

Van der Kamp, G. and J.E. Gale, "Theory of Earth Tide and Barometric Effects in Porous Formations with Compressible Grains," Water Res. Research, (in press), 1983.

Witherspoon, P.A., T.N. Narasimhan, and D.G. McEdwards, "Results of Interference Tests from Two Geothermal Reservoirs," J. Pet. Tech., Jan., 1978.

Zschau, J., "The Influence of Air Pressure Variations on Tilt Measurements With the Askania Borehole Pendulum at the Station Kiel-Rehmsberg," Proc. of the 7th Symposium on Earth Tides, Edited by G. Szadeczky-Kardoss, Akademiai Kiado, Budapest, 1976.

U. S. Government Printing Office: 1984/10-587-002/24012